MSc Thesis

Benefits of High-Temperature Storage for Base Load Geothermal Energy

T.M.G. van de Griendt

Benefits of High-Temperature Storage for Base Load Geothermal Energy

by

T.M.G. van de Griendt

to obtain the degree of Master of Science
at the Delft University of Technology,
to be defended publicly on Wednesday October 5, 2022 at 1.30 PM.

Student number:	4561848	
Project duration:	November 1, 2021 – October 5, 2022	
Thesis committee:	Dr. Ir. J.M. Bloemendal,	TU Delft, supervisor
	Dr. Ir. A.D. Daniilidis,	TU Delft, supervisor
	Dr. Ir. R. Godderij,	EBN B.V., supervisor

TU Delft

Abstract

Currently, a large part of the energy used to provide heat to heating network comes from gas boilers, a combustion process where 2.2kg of CO_2 is emitted for every m^3 of gas. Deep geothermal energy is implemented more in The Netherlands over the last couple of years as a substitute to the conventional boilers and this is a technique that is proven to be working. However, one problem with geothermal energy is the fact that only base load extraction is possible, whereas the heating demand varies throughout the year. During winter there is an energy shortage while during summer there is a surplus. Hence, seasonal heat storage is seen as a promising technique to increase the portion of green energy in heating networks.

High-Temperature Aquifer Thermal Energy Storage (HT-ATES) can bridge the gap between the supply and demand, storing excess produced heat during summer and supplying during the winter months. This research focuses on both the technical aspects as well as the business case of the implementation of such a system in a heating network. Technical simulations are performed where the fluid transport and heat loss processes are modelled. The output of these simulations is used to compare the business cases of a heating network with and without HT-ATES implementation, based on the Levelized Cost Of Heat (LCOH) and total annual CO_2 emissions in an economics tool developed in Python. All simulations are based on the situation at the TU Delft Campus, where plans are made for a HT-ATES in the Maassluis formation.

The base case shows a thermal recovery efficiency of 0.75 in cycle four. The LCOH for a project with a lifetime of 30 years is 52 €/MWh (14 €/GJ) when HT-ATES is implemented, compared to 61 €/MWh (17 €/GJ) in the case where only geothermal energy and gas boilers are used to supply the heat. Total CO_2 emission reductions are 31%. Based on these values, one can conclude that the situation where HT-ATES is included is the economic scenario.

On top of the case study, a parameter sensitivity study is performed. The results show that storage volume, storage reservoir permeability and temperature differences between the wells are the key geological and operational parameters when assessing the project feasibility. Economic parameters such as the discount rate and gas prices also have a considerable impact on the economic results. The results of the sensitivity analysis shows that the project in Delft is feasible as long as the future average gas price remains above 21 €/MWh and the discount rate does not exceed 18.3%, while keeping the other variables constant.

Preface

I would like to start off by thanking Delft University of Technology for giving me the opportunity to conduct my research on this topic. I am dedicated to try and help contributing to a sustainable world in the near future and the people at the University have teached me a lot to try and achieve this goal. This research, performed on a technique to enable more green energy in our heating systems, was the perfect way to start this journey.

Secondly, I want to thank EBN B.V. for giving me the opportunity to combine my thesis with an internship. The atmosphere in the office felt extremely good, everyone seems to love what they do and the enthusiastic and positive mindset of the people really had a good impact on my mood and productiveness. The A&I team deserves a special mention as well, they really made me feel part of the team and were always interested in my project and helpful when needed. Moreover, I want to thank my co-interns Bouke and Alonso for sharing a lot of coffee and lunch breaks together. We have one conclusion in common from our theses; wherever you go, lunch will never be as good as at the EBN office.

Over the last eleven months, I have gotten to know the CMG modelling environment better than my own house. This was not without its struggles, but the CMG Customer Support team was always available for help. They even provided me with a beta version of the software in order to solve a specific issue in my simulations. I would like to thank them for their contribution to the project.

I also want to thank my supervisors and graduation committee, Martin Bloemendal and Alexandros Daniliidis from TU Delft and Raymond Godderij from EBN B.V.. Your daily supervision kept me critical on my own work and often showed the broader perspective. You were always available when I got stuck and guided me very well from start to finish.

Finally, I could not have done this research without the support from friends and family. Jaro, thank you for your help, your coding skills are unmatched. To my roommates, study and tennis friends; thank you for all the fun we had outside office hours, this made sure I was sharp and ready again the next day. I would like to finish by thanking my family. Thank you mom and dad, Hugo and Susanna for your support, not only during this research but throughout my studies. People always say 'family is everything', but I know why, because family really is everything.

T.M.G. van de Griendt
Delft, October 2022

List of Figures

1.1 The mismatch in annual heat supply and -demand (Hartog, Bloemendal, Slingerland, & Van Wijk, 2016) . . . 2

2.1 3D Cartesian grid used in the simulations. Boundary conditions are dependent on well placement. . . . 8
2.2 Overview of reservoir geometry and well placement for the doublet . . . 8
2.3 Grid cell size overview for the doublet base case . . . 9
2.4 Overview of reservoir geometry and well placement for the 5-spot pattern. See Section 2.1.1 for further details regarding operating constraints. . . . 9
2.5 2D aerial overview of the quarter-five-spot pattern grid cell distribution . . . 10
2.6 HT-ATES recovery efficiency over time and difference in efficiency between years 10

4.1 Temperature of produced water for hot and warm well over time . . . 27
4.2 Vertical cross-section of the temperature profile after three cycles, just before hot-water injection of fourth cycle. The aquifer is at the 130 - 180 meter interval. 28
4.3 Vertical cross-section of the temperature profile after 3.5 cycles, just after hot-water injection of fourth cycle. The aquifer is at the 130 - 180 meter interval. . . 29
4.4 Horizontal cross-section at model top of the temperature profile after 3.5 cycles, just after hot-water injection of fourth cycle. Located at the top cell interval of the aquifer. . . . 29
4.5 Hot and warm well bottom hole pressures over time . . . 30
4.6 Heat demand per heat source . . . 31
4.7 Recovery efficiency of the base case over time . . . 31
4.8 Pumping costs and LCOH over time . . . 32

5.1 Recovery efficiencies for the fourth cycle for all scenarios as provided in Table 3.6 . . . 36
5.2 I-K temperature profile after exactly 3.5 cycles; right after the fourth hot-water injection period. Permeability: $k_h = 50D, k_v = 5D$. All other parameters are as provided in Table 3.4. . . . 36
5.3 I-K temperature profile after exactly 3.5 cycles; right after the fourth hot-water injection period. Permeability: $k_h = 1D, k_v = 0.1D$. All other parameters are as provided in Table 3.4. . . . 37
5.4 I-K temperature profile after exactly 3.5 cycles; right after the fourth hot-water injection period. Aquifer thickness: $h = 100m$. . . . 39
5.5 I-K temperature profile after exactly 3.5 cycles; right after the fourth hot-water injection period. Aquifer thickness: $h = 20m$. . . . 40
5.6 I-K temperature profile after exactly 3.5 cycles: right after the fourth hot-water injection period. One clay layer. . . . 41
5.7 I-K temperature profile after exactly 3.5 cycles: right after the fourth hot-water injection period. Two clay layers. . . . 41
5.8 HT-ATES energy output versus LCOH for the scenarios as provided in Table 3.6 42
5.9 Recovery efficiency in year 4 versus LCOH . . . 43

5.10 Horizontal permeability versus LCOH 44
5.11 Recovery efficiencies for different values of horizontal and vertical permeabilities 45
5.12 The difference in shape when k_v changes from 100 to 50 Darcy. Temperature profile after 6 months of hot-fluid injection. 45
5.13 LCOH plotted versus the projects' discount rate (r). All other parameters are kept constant as provided in Tables 3.4 and 3.5. 46
5.14 LCOH plotted versus the gas price. All other parameters are kept constant as provided in Tables 3.4 and 3.5. 47
5.15 LCOH plotted versus the HT-ATES CAPEX. All other parameters are kept constant as provided in Tables 3.4 and 3.5. 48
5.16 LCOH plotted versus the CO_2 tax. All other parameters are kept constant as provided in Tables 3.4 and 3.5. 48
5.17 LCOH plotted versus the electricity price. All other parameters are kept constant as provided in Tables 3.4 and 3.5. 49

1 Storage volume versus recovery efficiency 63
2 Storage volume versus LCOH 64
3 Vertical cross-section of the temperature profile after 0.5 cycle 65
4 Vertical cross-section of the temperature profile after 1 cycle 65
5 Vertical cross-section of the temperature profile after 1.5 cycles 66
6 Vertical cross-section of the temperature profile after 2 cycles 66
7 Vertical cross-section of the temperature profile after 2.5 cycles 67
8 Vertical cross-section of the temperature profile after 4 cycle 67
9 Vertical cross-section of the temperature profile after 4.5 cycles 68
10 Vertical cross-section of the temperature profile after 3.5 cycles for scenario 1; small storage volume 69
11 Vertical cross-section of the temperature profile after 3.5 cycles for scenario 2; small well spacing 69
12 Vertical cross-section of the temperature profile after 3.5 cycles for scenario 3; large well spacing 70
13 Vertical cross-section of the temperature profile after 3.5 cycles for scenario 4; screen length only in upper half 70
14 Vertical cross-section of the temperature profile after 3.5 cycles for scenario 5; higher temperatures in the wells 71
15 Vertical cross-section of the temperature profile after 3.5 cycles for scenario 6; larger temperature difference between the wells 71
16 Vertical cross-section of the temperature profile after 3.5 cycles for scenario 7; lower temperatures in the wells 72
17 Vertical cross-section of the temperature profile after 3.5 cycles for scenario 10; lower porosity 72
18 Vertical cross-section of the temperature profile after 3.5 cycles for scenario 11; higher rock compressibility 73
19 Vertical cross-section of the temperature profile after 3.5 cycles for scenario 12; lower rock specific heat 73
20 Vertical cross-section of the temperature profile after 3.5 cycles for scenario 13; higher rock thermal conductivity 74
21 Vertical cross-section of the temperature profile after 3.5 cycles for scenario 16; higher ambient temperature 74
22 Vertical cross-section of the temperature profile after 3.5 cycles for scenario 17; groundwater flow 75

23 Vertical cross-section of the temperature profile after 3.5 cycles for scenario 20; 5-spot pattern geometry 75
24 Vertical cross-section of the temperature profile after 3.5 cycles for scenario 21; injection and production profiles following the demand curve 76
25 Vertical cross-section of the temperature profile after 3.5 cycles for scenario 22; loading in 5 months and produce during 7 months 76

List of Tables

2.1 Geothermal, HT-ATES and gas boiler costs and revenues overview 16

3.1 Geological parameter overview 19
3.2 Operational parameter overview 20
3.3 Economic parameter overview 20
3.4 Operational and Geological/Subsurface parameters for base case scenario (Bloemendal et al., 2020) (Baker & Jensen, 2015) 22
3.5 Economic parameters for base case scenario (Bloemendal et al., 2020) 23
3.6 22 different scenarios with different geological or operational aspects 24
3.7 Using the values for these three important parameters, a total of 27 simulations were performed 25
3.8 Values used to further investigate the impact of storage volume 25
3.9 Values used to further investigate the impact of permeability 25
3.10 Values used to further investigate the relationship between vertical and horizontal permeabilities. A total of 12 simulations are performed using all combinations of the permeabilities shown in this Table. 26

5.1 Flow rates per interval in the hot well for scenarios 8 and 9 at the end of the simulations 38
5.2 The amount of energy stored in the aquifer and confining layers before and after hot-water injection, after 3.5 and after 4 cycles. 38

List of Abbreviations

Symbol / Abbreviation	Description	Unit
ATES	Aquifer Thermal Energy Storage	-
BHP	Bottom-Hole Pressure	kPa
CAPEX	Capital Expenditures	€
CMG	Computer Modelling Group	-
$c_{p.b}$	Bulk specific heat capacity	$\frac{J}{kg \cdot K}$
$c_{p.r}$	Rock specific heat capacity	$\frac{J}{kg \cdot K}$
$c_{p.w}$	Water specific heat capacity	$\frac{J}{kg \cdot K}$
c_r	Rock compressibility	kPa^{-1}
d	Depth	m
EOS	Equation Of State	-
GTD	Geothermie Delft	-
g	Gravitational acceleration	$\frac{m}{s^2}$
HT-ATES	High-Temperature Aquifer Thermal Energy Storage	-
HTO	Hoge Temperatuur Opslag	-
HTS	High-Temperature Storage	-
h	Thickness	m
K	Hydraulic conductivity	$\frac{m}{day}$
k_h	Horizontal permeability	Darcy
k_t	Bulk thermal conductivity	$\frac{W}{m \cdot K}$
k_v	Vertical permeability	Darcy
L	Screen length	m
LCOH	Levelized Cost of Heat	-
LT-ATES	Low-Temperature Aquifer Thermal Energy Storage	-
MT-ATES	Mid-Temperature Aquifer Thermal Energy Storage	-
N/G	Net-to-gross	-
NPV	Net Present Value	€
OPEX	Operational Expenditures	€
p	Pressure	kPa
p_i	Initial pressure	kPa
Q	Flow rate	$\frac{m^3}{day}$
RC	Reservoir Conditions	-
r	Discount rate	-
SC	Surface Conditions	-
SDE++	Stimulering Duurzame Energie	-
SOTA	State-Of-The-Art	-
T	Temperature	°C
T_i	Initial ambient temperature	°C
t	Time	Days

Symbol / Abbreviation	Description	Unit
V	Total water storage volume	m^3
v	Superficial (Darcy) velocity	$\frac{m}{day}$
w_f	Well fraction	-
ΔT	Temperature difference	°C
Δp	Pressure difference	kPa
η_{pump}	Pump efficiency	-

Contents

List of Figures ix

List of Tables xi

List of Abbreviations xiii

1 Introduction 1
- 1.1 Problem Statement . . . 1
  - 1.1.1 How does ATES work? . . . 1
  - 1.1.2 Previous studies on HT-ATES . . . 3
- 1.2 Research Questions . . . 4
- 1.3 Approach and thesis outline . . . 4

2 HT-ATES performance and feasibility simulators 7
- 2.1 CMG GEM Technical performance simulator . . . 7
  - 2.1.1 Reservoir model . . . 7
  - 2.1.2 Well model . . . 10
  - 2.1.3 Thermal model . . . 11
  - 2.1.4 Simulation outputs . . . 13
- 2.2 Python feasibility assessment tool . . . 13
  - 2.2.1 HT-ATES feasibility assessment criteria . . . 13
  - 2.2.2 Data transformation and HT-ATES power output . . . 14
  - 2.2.3 Costs . . . 15
  - 2.2.4 Levelized cost of heat . . . 16
  - 2.2.5 Load factors, CO_2 emissions and costs . . . 17
  - 2.2.6 Recovery efficiency . . . 17

3 Methodology 19
- 3.1 Overview of the parameters affecting HT-ATES feasibility . . . 19
  - 3.1.1 Geological parameters . . . 19
  - 3.1.2 Operational parameters . . . 20
  - 3.1.3 Economic parameters . . . 20
- 3.2 Case study Delft and parameter study . . . 21
  - 3.2.1 HT-ATES in Delft . . . 21
  - 3.2.2 Parameter study . . . 24

4 Results: Base Case 27
- 4.1 Results HT-ATES performance simulator . . . 27
- 4.2 Results Python feasibility assessment tool . . . 31

5 Results: Sensitivity analysis 35
- 5.1 Parameter variation analysis . . . 35
- 5.2 Study on storage volume, permeability and temperature difference . . . 42
- 5.3 Permeability study . . . 43
- 5.4 Impact of economic parameters on the LCOH . . . 46

6 Discussion **51**
6.1 Importance of the results 51
6.2 Added value in relation to previous studies 52
6.3 Consequences 52

7 Conclusions and Recommendations **55**
7.1 Conclusions 55
7.2 Recommendations. 57

Appendices **63**
Appendix I: Study on storage volume 63
Appendix II: Base case temperature profiles. 65
Appendix III: Temperature profiles of the scenarios from parameter study 69

1

Introduction

1.1. Problem Statement

In recent years, global warming has triggered a large-scale energy transition from fossil to renewable energy resources. In the process of making this shift, new solutions, but also new problems arise.

The heating industry is one of the sectors that needs to make this shift. In 2020, a total of 41% of the total energy demand was covered by the demand for heat (EBN, 2022). Still 88% of the total heating demand in The Netherlands is provided from oil and gas (Van Gessel, Huijskes, Juez-Larré, & Dalman, 2021). Renewable alternatives are introduced in heating networks, such as geothermal and solar heat and heat from biomass.

However, substituting the oil and gas with renewables is not as straightforward as one might think, since all energy sources have different optimal ways of implementation. Geothermal power, in particular, operates the most efficiently when it runs continuously without interruption (Matek & Gawell, 2015) and solar heat is highly dependent on the amount of daily hours of sun.

Depending on the combination of different heat resources, there is a mismatch in heat demand and supply. In Figure 1.1, a geothermal base load is shown in combination with a variable heat demand (Hartog et al., 2016). During summer, the base load exceeds the heat demand while in winter the demand is higher than the heat provided by the geothermal doublet. The red coloured area shows the storage potential of the excess geothermal heat. When this can be stored, it can (partly) account for the deficit in winter months. In this specific figure it even fully accounts for the winter deficits. Large-scale seasonal heat storage is possible, in the form of Aquifer Thermal Energy Storage (ATES).

1.1.1. How does ATES work?

ATES makes use of the difference in temperature of the stored medium (e.g. water) in the subsurface and the seasonal temperatures at the surface. ATES can, depending on this difference in temperatures, provide either heating or cooling during specific periods. The storage system is based on the seasonal changes in temperature, where during summer there is an excess of heat while in winter months the temperatures are low. Storing cold water in aquifers during winter could provide cooling to buildings in warmer periods and vice versa.

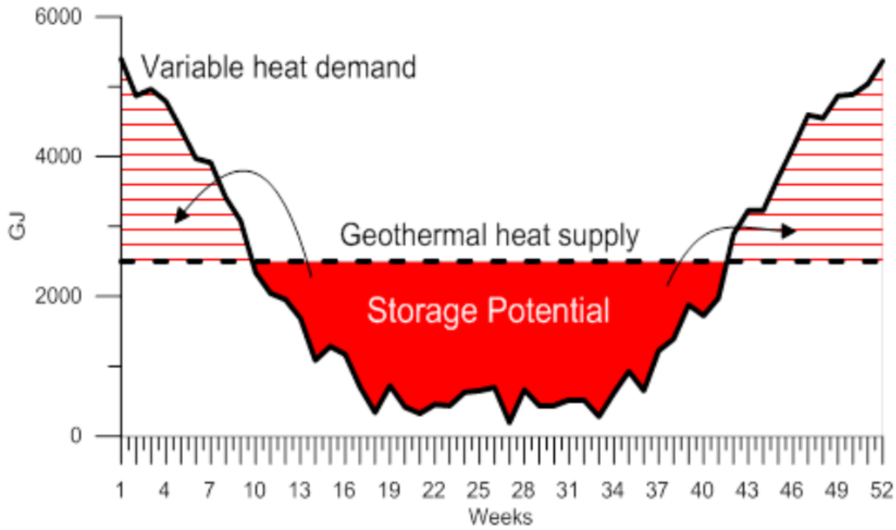

Figure 1.1: The mismatch in annual heat supply and -demand (Hartog et al., 2016)

Types of systems

There are multiple types of ATES systems. First of all, a distinction can be made between systems that work with different temperatures. When initial storage temperatures are below 30 °C, such a system is called a Low-Temperature (LT-) ATES, a Mid-Temperature (MT-) ATES has storage temperatures between 30-60 °C and all systems exceeding 60 °C are HT-ATES systems (Driesner, 2021).

LT-ATES is already widely used in The Netherlands. In 2018, there were over 2500 LT-ATES systems present in The Netherlands and this number is increasing (Marif, 2019). However, HT-ATES systems are not as common. In recent years, only three of such systems have been realized in The Netherlands, one at Utrecht University, one in Zwammerdam, near Gouda (Drijver, Van Aarssen, & De Zwart, 2012), and the third in Middenmeer. The locations in Utrecht and Zwammerdam have been closed due to technical complications and as of today there are only two known working systems, the one in Middenmeer (since 2021) and one at the Reichstag Building in Berlin, Germany.

Advantages and disadvantages of HT-ATES

The main reasons why the HT-ATES system is barely used as of yet are low recovery efficiencies and technical problems that occurred in previous projects (Drijver et al., 2012). The recovery efficiency is generally lower than for lower temperature projects, since the difference between storage and ambient temperature is larger, resulting in more heat losses to the surroundings. In Chapter 4, a closer look will be taken on the technical aspects of the recovery efficiency. Especially in the ’80s, a lot of technical problems occurred in experimental and pilot plants (Drijver et al., 2012). These problems included mineral precipitation and corrosion of components in the groundwater system (Drijver et al., 2012). Since this period, a lot of new research has been performed, resulting in solutions that could be applied to the systems to fix the issues.

One of the advantages of HT-ATES is that the primary energy source can be used more efficiently. When, for example, a geothermal doublet is combined with heat storage, the load factor of the doublet can be increased due to the direct use of the excess heat to fill the ATES when heat demand is low. Another advantage is that, generally speaking, a reduction of greenhouse gas emissions can be obtained because of the more efficient usage of the geothermal doublet. This can also be obtained from the research performed by Bloemendal et al. (2020) where a 31% CO_2 reduction is predicted when implementing HT-ATES at the TU Delft Campus.

Another advantage of high-temperature storage is the fact that the heat can directly be used to heat buildings. For Low- and Mid-Temperature systems, a heat pump is desired in most cases to heat the water to the desired temperature. Also, there is only little space needed at the surface to provide a significant portion of the heat when demand is high. Especially considering that at locations where the heat demand is high, there is generally not a lot of space at the surface and if there is any, it will be expensive. Last but not least, HT-ATES can improve the business cases for specific heating networks (Bloemendal et al., 2020). This research will focus on the business case of HT-ATES implementation in heating networks.

1.1.2. Previous studies on HT-ATES

Even though there clearly is an opportunity for HT-ATES to be used more widely for heating purposes, at the moment only one project is in operation in The Netherlands, which is the HT-ATES in Middenmeer at ECW Energy. The performed case study on this specific project shows that the High-Temperature Storage implementation significantly saves costs in combination with deep geothermal energy, but in order to make geothermal profitable still subsidies are necessary (Dinkelman, 2019). There are a couple of reasons why HT-ATES is not yet widely used in The Netherlands.

The paper of Fleuchaus, Godschalk, Stober, and Blum (2018) provides an overview of the current situation of ATES implementation worldwide. It concludes that ATES technology has proven its ability to efficiently tackle the seasonal mismatch between periods of highest energy supply and highest energy demand. However, despite the high potential in most developed economies, a significant position in energy markets is still missing. Appropriate legislative basis is needed, as well as well-placed subsidies. This paper also indicates that most research performed already, is focused on technical aspects for the Thermal Energy Storage.

One of these researches is the MSc thesis of Marif (2019), where the effect of buoyancy flow is studied. Buoyancy flow is the heat transport via convection that takes place due to different fluid temperatures and therefore different fluid densities. This research focuses on how to counteract this effect using multiple partially penetrating wells to improve recovery efficiencies. Another method to counteract the buoyancy flow is also studied, namely the use of salinity contrast for density difference compensation. This research is performed by Van Lopik, Hartog, and Zaadnoordijk (2016) and there it is concluded that this method improves system recovery efficiencies.

Schout, Drijver, Gutierrez-Neri, and Schotting (2014) presented a numerical evaluation of the prime factors influencing the recovery efficiency. An interesting result obtained from their research was that a correlation is found between the Rayleigh number, which is a measure of relative strength of free convection, and the thermal recovery efficiency. Also the storage system efficiency is studied over time and there it is found that after a total of four cycles the efficiency stabilizes. One cycle is one full period of hot-water injection and extraction.

More technical research is performed by Oerlemans (2018), where the heat transport in HT-ATES systems is modelled in a numerical 2D axisymmetric SEAWATv4 model. Heat conduction and convection processes were studied and a relationship was found between storage temperatures and the main heat loss processes. At low temperatures, most heat was lost due to conduction, whereas for higher storage temperatures the buoyancy flow causes more heat losses via convection. Different storage volumes were tested and there it is found that larger volumes result in higher recovery efficiencies.

One of the few publications that included HT-ATES economics is the work from Daniilidis, Mindel, De Oliveira Filho, and Guglielmetti (2022), where a techno-economic and CO_2 emissions assessment of HT-ATES systems is performed. In the paper from Daniilidis et al. (2022), the economic index used for assessment was LCOH and this method is adopted for this specific research.

1.2. Research Questions

Fleuchaus et al. (2018) concluded their research with the following: 'The identification of parameters, which affect the economic performance of an ATES, would not only be a first step towards a financial optimization of ATES plants, but also a tremendous support for stakeholders and decision makers to estimate capital costs and financial payback times'. This still clearly is the major bottleneck that prevents HT-ATES implementation to be accomplished in more heating networks. Therefore, this research will focus on studying these decisive parameters, not only from a technical point of view, but from an economic perspective.

A unique aspect of this research is that for the economic assessment, not only the HT-ATES economics but also a geothermal doublet and gas boilers are taken into account. This gives an overview of the total costs of the heat network for the operator. Another aspect is that the HT-ATES technical simulations will be performed in CMG GEM software (LTD., 2022). This software is developed primarily for the oil and gas industry and is widely used by companies in this sector. Creating high-temperature storage simulations in this software could lower the threshold for companies in this industry to also consider starting such projects, because they are already familiar with the software.

Based on the questions that still arise after performing the literature review, as mentioned above, the research question for this specific research is constructed as follows:

How can geological, operational and economic parameters be modelled to obtain a business case for HT-ATES implementation? And what are the decisive characteristics for HT-ATES economic feasibility?

1.3. Approach and thesis outline

In order to be able to answer the first question, a case study is performed on HT-ATES implementation at the TU Delft Campus. From literature, all necessary parameters are retrieved. A HT-ATES technical performance simulator is created in CMG GEM software where the geological and part of the operational characteristics are modelled. The output of these technical simulations are used in a Python economic assessment tool to obtain valuable information about the business case of the implementation in the current heat network at the TU Delft Campus.

The second question is answered by performing a sensitivity analysis, where the high-temperature storage in Delft is used as a base case. All parameters are changed to study the effect on both technical performance as well as economic feasibility.

In Chapter 2.1, the HT-ATES performance simulator and the Python feasibility assessment tool are discussed. A technical model is used, where the parameters shown in Tables 3.1 and 3.2 are used as inputs, together with the aquifer geometry and well locations. Hot-water injection and production takes place over time and the model calculates the pressure and temperature profiles. The main outputs, used as inputs for the economics model, are BHP's, well-head temperatures and volumetric flow rates at standard conditions over time for all wells. Further details about the model are provided in Section 2.1.

The technical simulations show the technical and operational possibilities and difficulties when storing the heat in the subsurface. However, the technical feasibility is not the only important factor, in the end it also matters whether or not the project is financially feasible. Therefore, an economic assessment is performed.

At the moment, there are still a lot of uncertainties regarding the economics behind HT-ATES. As is explained in Section 1.1, only very few HT-ATES systems are currently active and even then the business cases might be very different due to different subsurface and operating conditions. But with the information that is available at this point, one can still obtain valuable information about the business cases. This is done in the Python feasibility assessment tool, where the outputs described above are used as input parameters, together with the economic parameters provided in Table 3.3. Further details about this model are provided in Section 2.2

In the Methodology, Chapter 3, some background information is provided regarding the different types of ATES systems. Based on literature research, a list is created with all parameters that could affect HT-ATES economic feasibility. This list includes different types of parameters, both geological, operational and economic. Afterwards, values are coupled to all of these parameters, based on the situation of HT-ATES implementation at the TU Delft Campus. These values are used to simulate the base case. A sensitivity analysis is performed afterwards, where parameters are changed to study the effect on the final technical and economic feasibility.

There are two chapters that provide the results of this research. In Chapter 4 the result for the case study can be found and in Chapter 5 the results of the parameter study are highlighted and already briefly discussed. Further general discussion about the results is provided in Chapter 6. The report will end with the conclusions and recommendations and appendices in Chapters 7 and 8, respectively.

2

HT-ATES performance and feasibility simulators

2.1. CMG GEM Technical performance simulator

CMG GEM is a multidimensional, equation-of-state (EOS) compositional numerical simulator developed by Computer Modelling Group LTD (LTD., 2022). Its main purpose is to model oil and gas reservoirs, however, due to the wide input range and its thermal function, it can be used for other purposes as well, including CO_2 and hydrogen storage, geothermal and heat storage simulations. This software is used to simulate the technical part of the HT-ATES, further referred to as the HT-ATES performance simulator. In this Chapter, the important functions and principles used for the simulations are provided. This includes the reservoir, well and thermal model and density calculations.

2.1.1. Reservoir model

Grid and boundary conditions

All simulations are performed in a 3D Cartesian grid, where a permeable aquifer is confined by (almost) impermeable clay formations, as is shown in Figure 2.1. All three formations are homogeneous and characteristics are the same for I- and J-directions, however, some can vary in the K-direction. Two different well geometries are tested, these include a doublet and a quarter-five-spot pattern.

Doublet

The doublet includes one hot and one warm well, both placed at one of the grid boundaries. This is a no-flow boundary and no heat conduction can take place, so that the simulated processes are mirrored along this boundary. The other three boundaries are open-flow, where grid cell volumes along these boundaries are multiplied by $1e^{15}$. The bottom and top of the grid are defined as Neumann boundary conditions; heat losses can take place. However, for all simulated scenarios the grid is constructed in a way that heat propagation is far away from these boundaries so that it does not affect the simulations. An overview is shown in Figure 2.2.

Cell sizes are not homogeneous throughout the grid, since in the region of the well screen intervals the most important processes occur. This means that in the vertical direction, cells are smaller in and just below and above the aquifer. Also in I- and J-directions, the cell sizes differ according to distance to the wells. This is shown in Figure 2.3. Impact of cell sizes on the

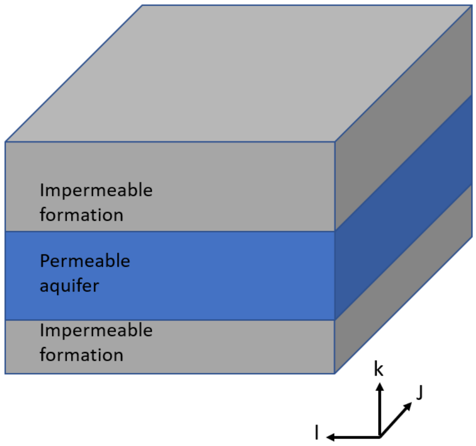

Figure 2.1: 3D Cartesian grid used in the simulations. Boundary conditions are dependent on well placement.

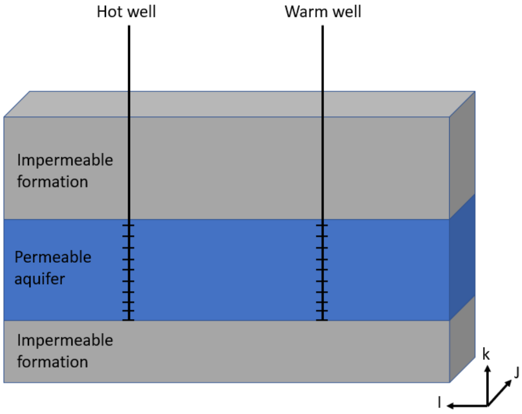

(a) 3D overview

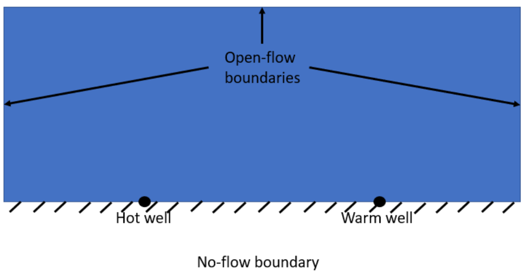

(b) 2D aerial overview

Figure 2.2: Overview of reservoir geometry and well placement for the doublet

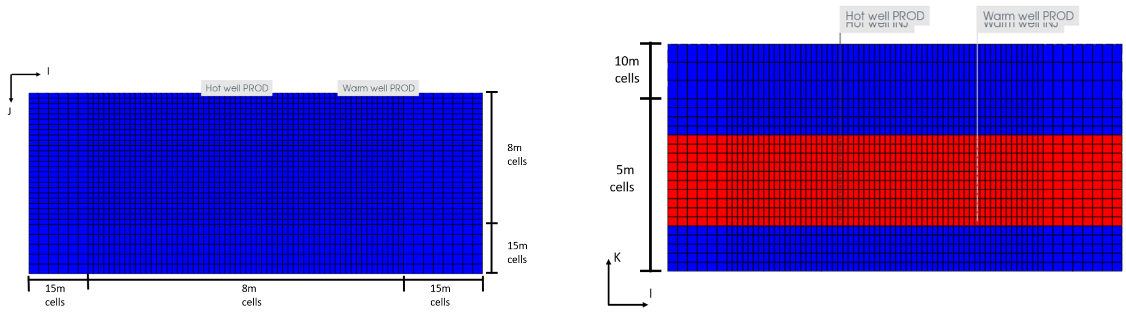

(a) 2D aerial overview (b) I-K view

Figure 2.3: Grid cell size overview for the doublet base case

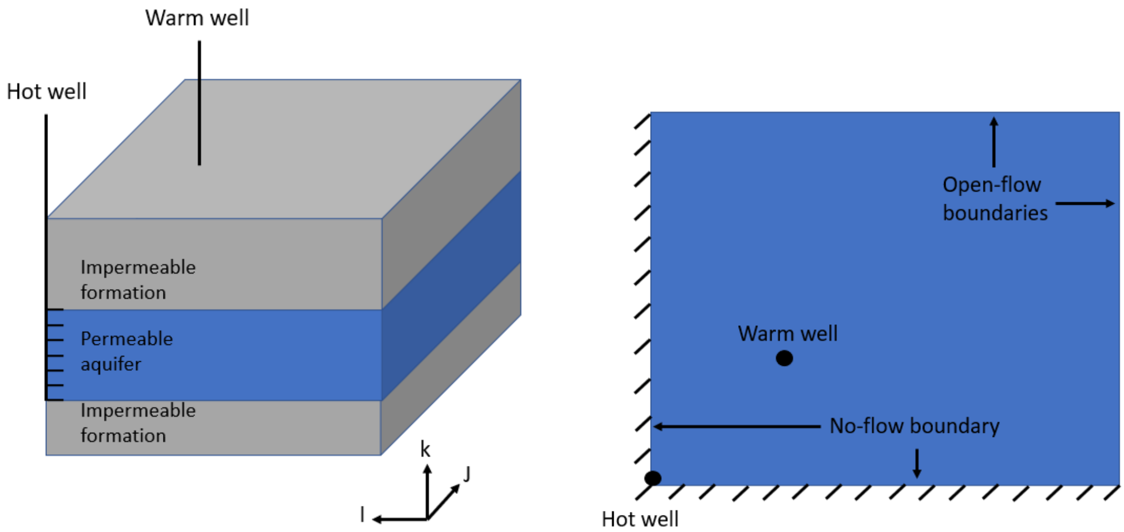

(a) 3D overview (b) 2D aerial overview

Figure 2.4: Overview of reservoir geometry and well placement for the 5-spot pattern. See Section 2.1.1 for further details regarding operating constraints.

results were studied in advance to eliminate numerical dispersion effects while also limiting simulation runtime.

Quarter-five-spot pattern

The quarter-five-spot pattern includes two closed and two open vertical boundary planes. The grid boundaries intersecting the hot well do not allow flow or heat conduction, to simulate a scenario where on the other side of this boundary the exact same processes are taking place. The grid cell distribution in the vertical direction equals the one shown in Figure 2.3(b). However, due to different well placement, the aerial distribution differs, as shown in Figure 2.5.

Operating constraints

All wells are operated based on a surface volumetric water rate constraint. This is because of the assumption that loading the storage system is based on a base load from the geothermal doublet. When reproducing the stored heat, the total power now is only dependent on the fluid temperature. The total volumetric flow rate in the well is dependent on the well placement and scenario. For the doublet geometry, flow rates in the simulations are divided by two, because of the mirroring concept and for the quarter-five-spot pattern, the hot well flow rate is divided by four. By doing so, the total injection and production rates in the simulations are always

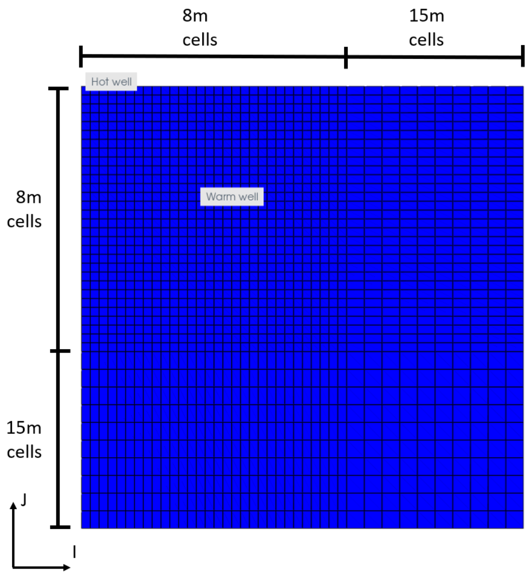

Figure 2.5: 2D aerial overview of the quarter-five-spot pattern grid cell distribution

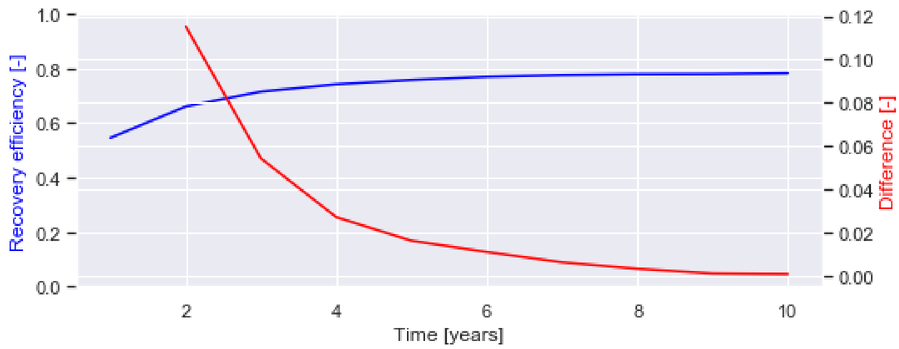

Figure 2.6: HT-ATES recovery efficiency over time and difference in efficiency between years

constant.

Using the doublet grid and boundary conditions as formulated in Section 2.1.1, one is able to run the heat storage simulations over time. From Van Lopik et al. (2016) and own simulations running for a total of 10 years, one can conclude that a 'thermal equilibrium' is reached after four cycles: the first three cycles generate lower performances because the system needs to heat up. From the fourth cycle onwards, performance does not improve significantly and to limit simulation runtime, further simulations are done over a total of four years. It can be obtained from Figure 2.6 that the recovery efficiency improves only 3 percentage point from year 4 to year 10. This does not weight up against the increased simulation runtime, which is roughly 2.5 times longer. Also, the efficiency in the first three years is lower so taking year four as a reference on average is a representative efficiency.

2.1.2. Well model

The injection and production rates along the well screen are based on well injectivity and productivity indices, fluid mobilities and pressure differences. There are different relationships for the injection and production rates in a grid cell, as shown in Equations 2.1 and 2.3.

$$Q_j = \sum_l WI_l \lambda_{T,l}(p_{bh} - p_{o,i}) \tag{2.1}$$

Where,

$$WI = 2\pi ffkh \frac{w_f}{ln(r_e/r_w) + S} \tag{2.2}$$

The well injectivity index from Equation 2.2, is a function of the fraction of completion of the well in the grid block (ff [-]), effective permeability (k [mD]), grid block thickness in well direction (h [m]), well fraction governed by the aerial geometry (w_f [-]) (LTD., 2022), effective and wellbore radius (r_e and r_w [m]) and skin factor (S [-]). The fluid mobility ($\lambda_{T,l}$ [$\frac{mD}{m^2/s}$]) is defined as $\sum_j \frac{k_{rj}}{\mu_j} j = o, g, w$, but since the heat storage model only includes a single component this can be simplified to $\lambda_T = \frac{k_r}{\mu}$. The main driver for fluid flow near the wells is the pressure difference between the bottom-hole pressure (p_{bh} [kPa]) and pressure of the grid cell in which the screen is placed ($p_{o,i}$ [kPa]).

The flow rates for cells in the production well are calculated using the relationship in Equation 2.3.

$$Q_j = \sum_l PI_{j,l} \left(\frac{k_r}{\mu}\right)_{j,l} (p_{o,i} - p_{bh}) \tag{2.3}$$

Where,

$$PI = 2\pi ffkh \frac{w_f}{ln(r_e/r_w) + S} \tag{2.4}$$

In the case of well completion in multiple grid cells, as is the case in the base scenario, the bottom-hole pressure is defined as shown in Equation 2.5.

$$p_{bh,i} = p_{bh,l} - \int_{hi}^{hl} \tilde{\rho}^T g dh \tag{2.5}$$

Where $\tilde{\rho}^T$ [$\frac{kg}{m^3}$] is the density of all phases present in the wellbore, g [$\frac{m}{s^2}$] the gravitational constant and h [m] the depth, measured positive downwards. Since this specific model only includes one phase, $\tilde{\rho}^T$ can be simplified to ρ_w [$\frac{kg}{m^3}$], the water density at that specific moment and location.

2.1.3. Thermal model

The thermal option in GEM is used to derive temperature profiles over time in the grid. Heat exchange does take place when injecting fluids at different temperatures compared to ambient temperatures, this propagation is crucial for modelling heat storage applications.

Energy balance equation

In order to model the heat propagation, GEM makes use of an energy balance equation that includes convection, conduction and heat losses to the surroundings. Enthalpy calculations for the oil and gas phase are performed from an EoS, however these phases are zero in the energy balance for this specific model. Water enthalpy is determined from the steam table, where values for temperature as a function of pressure are given. The energy balance equation is given in Equation 2.6 (LTD., 2022).

$$\nabla \cdot \left[\sum_{\alpha=1}^{N_p} \rho_\alpha H_\alpha \frac{k_{r,\alpha}\mathbf{K}}{\mu_\alpha}(\nabla P_\alpha - \rho_\alpha g \nabla h)\right] + \sum_{\alpha=1}^{N_p}(H_\alpha Q_\alpha) = \frac{\delta}{\delta t}\left[\phi \sum_{\alpha=1}^{N_p}(\rho_\alpha U_\alpha S_\alpha) + (1-\phi)C_r(T - T_i)\right] \tag{2.6}$$

Equation 2.6 is based on the mass balance and Darcy multiphase flow equations, where N_p [-] is the phase number in the system, ϕ [-] the aquifer porosity, ρ_α [$\frac{kg}{m^3}$] the density of phase α, S_α [-] the saturation of phase α, **K** the rock permeability tensor [-], $K_{r,\alpha}$ [-] and μ_α [$\frac{m^2}{s}$] the relative permeability and viscosity of phase α. p [kPa] is the pressure with h [m] as corresponding height in the reservoir. H_α [J], Q_α [$\frac{m^3}{s}$] and U_α [J] are the enthalpy, injection rate and internal energy of phase α, respectively. Heat losses to the reservoir rock are described by the rock specific heat C_r [$\frac{kJ}{kg \cdot C}$] and temperature difference $(T - T_i)$ [$°C$], where T [$°C$] is the reservoir rock temperature. Heat loss might not be the right description here, since the heat is not lost, but rather stored in the formation. During hot-water production periods, the heat contained in the grains is extracted again. During this process, the fluid propagation through the formation transports heat in the form of convection. Due to the interaction between the hot water and colder formation grains, heat is transported into the grains via heat conduction. This results in a thermal propagation slower than the fluid velocity itself, called thermal retardation.

Since in this specific model only one phase is present, the energy balance equation can be simplified to the following, shown in Equation 2.7.

$$\nabla \cdot \left[\rho H \frac{\mathbf{K}}{\mu}(\nabla P - \rho g \nabla h)\right] + HQ = \frac{\delta}{\delta t}\left[\phi \rho U + (1-\rho)C_r(T - T_i)\right] \tag{2.7}$$

Here, all phase annotations are deleted and the characteristics should be taken for water as the single component. Relative permeability and phase saturation are absent now as well.

Heat losses

Heat losses to the over- and underburden are calculated using the method of Vinsome and Westerveld (1980), where a specific temperature in the confining formations is assumed. This temperature is defined as in Equation 2.8 and is applied to the top and bottom boundaries of the grid.

$$T(t,z) = (\Theta - \Theta^0 + b_1 z + b_2 z^2)e^{-(z/d)+\Theta^0} \tag{2.8}$$

In the Equation above, $T(t,z)$ is the over- and underburden temperature at time t and distance z from the reservoir boundary, b_1 and b_2 are time-dependent parameters, d the thermal diffusion length, Θ the temperature in the boundary grid cell and Θ^0 the initial temperature in this cell. Equations for the diffusion length, time-dependent parameters and the total heat loss rate can be found in Vinsome and Westerveld (1980).

Rowe-Chou density calculations

Since from preliminary literature study is known that buoyancy flow plays an important role in heat convection in the aquifer (Marif, 2019), fluid density calculations should take temperature into account. This is the case when using the Rowe-Chou empirical equation for density calculations (Rowe & Chou, 1970), which has a maximum error of 0.2% over the tested interval, which is from 0 to 176 °C and from 0 to 345 bar (Numbere, Brigham, & Standing, 1977). This is within the projected temperature and pressure range for the simulations for this research.

2.1.4. Simulation outputs

One of the goals of the simulations in the CMG GEM software is to study the subsurface heat propagation processes, in order to understand how each parameter affects the total storage efficiency. CMG has software to show 2D and 3D profiles of the important aspects over time, the most important ones for these simulations being pressure and temperature profiles. Well injection and production data is obtained as well. This data is important for the economic feasibility assessment.

2.2. Python feasibility assessment tool

The results from the technical model can be used in combination with economic inputs, to obtain a business case for a project. This Chapter focuses on the economics analysis and explains the calculations performed in the economics model.

2.2.1. HT-ATES feasibility assessment criteria

The parameters controlling HT-ATES feasibility are the main focus of this research. But before the feasibility study can be performed, first it should be defined how HT-ATES feasibility is assessed. Feasibility analysis is a management decision tool that assesses the viability of a project concept to enable an organisation to decide whether to go ahead with a project concept or to reject it and hence avoid wasting resources (Ssegawaa & Muzindab, 2021).

Whether or not HT-ATES should be implemented in certain heat networks, depends on several aspects. These aspects are listed below;

- **Economic value**: Implementation will initially add costs to the network, but depending on the benefits can also save money on the long term.
- **Emissions**: HT-ATES could result in a larger part of a renewable heat source (e.g. geothermal) to account for the total demand, emitting less CO_2.
- **Robustness**: One of the most important aspects of an energy system is its consistency in the ability to supply the energy needed. The energy system needs to cope with risks, threats and adverse events that can jeopardize its capacity to satisfy the needs of the end users (Blanco & Faaij, 2018).
- **Neighbourhood disturbances**: Livability is extremely important, any disturbances in the neighbourhood should be taken serious. Implementation of HT-ATES should not result in too much noise disturbance or any other disturbances.

The robustness and neighbourhood disturbances are hard to measure, since it cannot be expressed in specific numbers to assess. In order to assess the robustness of the heat network after implementation of HT-ATES, the chances of failure of specific parts in the storage system, such as well clogging, a power cut that could restrict the pumps, or any damage to the pumps, piping network, etc., should be looked into.

Disturbances in the neighbourhood could mainly include noise, smells or lighting during evenings and/or nights. In order to obtain the best efficiency, heat transport should be minimized and therefore the storage location should be close to the heat consumers. The installation of HT-ATES could generate noise, for example, during drilling and the pumps could generate some noise as well. With the heat consumers close by, these disturbances should be considered well before the start of the project. However, system robustness and neighbourhood disturbances are beyond the scope of this research and therefore will not be assessed.

The economic value and emissions of greenhouse gasses can easier be assessed. The economic value focuses on installation costs, fixed and variable costs, and revenues from heat delivery to consumers. This will be evaluated by looking into the Levelized Cost Of Heat (LCOH) of the project. The payback time will be taken into account as well. In Section 2.2.4, it is elaborated further into the means of these values.

From literature, one is able to obtain the amount of CO_2 emitted by providing 1 MWh of energy from a specific heat source. When taking into account the energy mix that will account for the heat demand, one is able to calculate the total amount of emitted CO_2. This evaluation can be performed for different heat supply scenarios and then be compared to each other.

The feasibility assessment tool created in Python provides key information about the economic value in the form of the LCOH, combined with an overview of the costs involved and the system load factors. The emission aspect is also covered, annual CO_2 emissions are determined as well. This will be highlighted in further detail in the next section.

2.2.2. Data transformation and HT-ATES power output

The feasibility assessment simulations have been performed in Python, the code and all input files can be found here: `https://github.com/ToonvdGriendt/HT-ATES_MSc_thesis`. Throughout the code, the Numpy library (Harris et al., 2020) is used for numerous calculations and for plotting purposes the matplotlib.pyplot library (Hunter, 2007) is used. The Seaborn library (Waskom, 2021) is also used, to clarify the plots by providing a background grid for x- and y-values. First, the extracted Excel data files from CMG GEM are called. The data should be slightly transformed since the economics assessment can best be performed when the time step between the data rows is constant. This is not the case in the extracted data.

A Pandas DataFrame (pandas development team, 2020) is used to adjust the time steps between the data, where first a new index is created based on a specific time interval; in this case one day. Then, a linear interpolation method is used to obtain the new data and the new index is assigned. After this is done, fluid flow rates are multiplied by a specific factor (2 or 4), based on the well geometry as explained in Section 2.1.

Apart from the extracted files from the HT-ATES performance simulator in CMG GEM, also an annual heating demand curve is required as an input. This demand can also be found in the Github repository. An assumption is made that all years have the same demand curve.

The bottom-hole temperature, pressure and volumetric flow rates at surface conditions over time are extracted from GEM for both wells and used to obtain the business case in the economics model. First, a simple relation shown in Equation 2.9 is used to obtain the HT-ATES power output, where $P_{HT-ATES}$ is the power $[MW]$, Q the volumetric flow rate $[\frac{m^3}{day}]$, ρ the fluid density $[\frac{kg}{m^3}]$, c the fluid specific heat capacity $[\frac{J}{kg \cdot K}]$ and dT the temperature difference between the injected and produced fluid $[°C]$.

$$P_{HT-ATES} = \frac{Q\rho c dT}{1e^{6} \cdot 24 \cdot 3600} \tag{2.9}$$

The power output from the heat storage is combined with the geothermal power output and the annual demand curve in order to obtain the supply and demand curve as shown in Figure

4.6(a) in Chapter 4. To get a clear overview on how much heat is provided by what source, a pie chart is created containing all heat suppliers. The amount of heat generated by gas boilers is obtained by the difference between the sum of geothermal and HT-ATES heat and the total demand; all that is not covered by the green energy suppliers will be delivered from gas boilers.

According to Driesner (2021), base load injection and extraction is preferred during the loading and production periods to limit heat losses during the transport to the surface. For the base case scenario, as provided later in Section 3.2.1, this is the case. Over the full injection and production periods, a constant flow rate is used. However, situations might occur where the total heat demand is lower than the geothermal and HT-ATES power combined. In that case, heat is still extracted from the heat storage system, to be in line with the recommendation of Driesner (2021). However, in Section 3.2.2, there is looked into a case where the HT-ATES injection and production follows the demand curve.

The conventional target reservoirs for hydrocarbons are often identical to those considered for geothermal resources, i.e. sandstone formations of Lower Cretaceous, Upper-Jurassic, Triassic and Permian age. Co-production of dissolved gas and, in rare cases, oil is observed at most of the geothermal systems in the Netherlands (MEA, 2018). Primarily this is dissolved in the water at reservoir conditions and separates when the pressure decreases at surface conditions. However, this is not always the case and the gas does not have to be methane, it can for example also be CO_2 or another gas. Therefore this possibility will be disregarded in the calculations; all gas is bought at the marked price.

2.2.3. Costs

In order to be able to obtain valuable information about the viability of a project, the costs of all heat suppliers of the network are considered. In this case, the costs for the geothermal doublet, heat storage and the gas boiler. For all investment costs (CapEx), fixed and variable OpEx, the total CO_2 emissions and costs and the revenues are determined. The values with their references are given in Table 2.1, except for the variable OPEX for the heat storage. This is based on the pumping power and can therefore directly be derived from the HT-ATES performance simulator output.

The variable OPEX for the HT-ATES is given in Equation 2.10.

$$OPEX_{pump} = price_{elec} \frac{Q \cdot |p_{hot} - p_{warm}|}{1e^3 \cdot 24 \cdot 3600 \cdot \eta_{pump}} \cdot dt \tag{2.10}$$

Where $price_{elec}$ is the electricity price used, Q the fluid volumetric flow rate [$\frac{m^3}{day}$], p_{hot} and p_{warm} the well bottom-hole pressures [kPa], η_{pump} the pump efficiency [-] and dt is the specific time step over which the OpEx is calculated [$days$]. Other parameters that are required for the economics assessment are the total lifetime of the project, CO_2 tax, the projects discount rate and the cutoff temperature of the heat storage system, which is generally equal to the heat network temperature.

The HT-ATES investment and installation (CAPEX) is taken as a function of the total maximum power output of the system. This is in line with WarmingUp (2021) and is in order to make the costs applicable to multiple scenarios. If for a project the CAPEX specific costs (e.g. drilling costs) are known, one can always substitute this in the total overview.

Table 2.1: Geothermal, HT-ATES and gas boiler costs and revenues overview

Costs and revenues	Value	Unit	Reference
Geothermal			
Investment and installation (P < 12MW)	2.333	M€/MW	PBL (2022)
Investment and installation (12MW $\leq P$ < 20MW)	1.395	M€/MW	PBL (2022)
Investment and installation ($P \geq$ 20MW)	1.014	M€/MW	PBL (2022)
Fixed operational and maintenance	91	k€/MW/year	WarmingUp (2021)
Variable operational	2	€/MWh	WarmingUp (2021)
CO_2 emissions	23	kg/MWh	WarmingUp (2021)
HT-ATES			
Investment and installation	0.9	M€/MW	WarmingUp (2021)
Fixed operational and maintenance	180	k€/year	WarmingUp (2021)
Variable operational (pumping costs)	-	-	-
Electricity price	145	€/MWh	EMI (2022)
CO_2 emissions	27.63	kg/MWh	TNO (2020)
Gas boiler			
Investment and installation	0.1	M€/MW	WarmingUp (2021)
Fixed operational and maintenance	2	% of CAPEX/year	WarmingUp (2021)
Variable operational	100	€/MWh	EEX (2022)
CO_2 emissions	200	kg/MWh	DUEC (2022)

2.2.4. Levelized cost of heat

The LCOH is defined as the total net present costs over the total energy and shows the value of the supplied energy. The LCOH is a single project value that can be determined when the lifetime of the project is known, however, it can also be plotted as a function of the project lifetime. The LCOH after n timesteps can be calculated using Equation 2.11 (Daniilidis et al., 2022).

$$\mathrm{LCOH} = \frac{\sum_{t=0}^{n} \frac{CAPEX+OPEX}{(1+r)^t}}{\sum_{t=0}^{n} \frac{E_t}{(1+r)^t}} \tag{2.11}$$

Where E_t is the total produced energy [MWh] (the sum of the energy produced by the geothermal doublet, gas boilers and the heat retrieved from the HT-ATES), r the discount rate [-] and t the time periods. The OPEX is the summation of all operational expenses of all energy suppliers, as shown in Equation 2.12. The subscript 'total' indicates that these components are for all heat suppliers.

$$\mathrm{OPEX} = \text{fixed OPEX}_{total} + \text{variable OPEX}_{total} + \mathrm{CO_2}\ \text{tax}_{total} \tag{2.12}$$

The main advantage of using LCOH over NPV is the fact that when using the LCOH, no predictions have to be done regarding the future energy prices. Since the energy prices have been extremely volatile over the last months and years, this will bring high uncertainties into the business case assessment. The LCOH can be used to compare to the LCOH of other suppliers or networks and the lowest will be the most attractive, generating the same heat at lower costs.

The LCOH is calculated in the Python tool and added as a column to the Pandas DataFrame, so that the data over time is stored. This is done for two scenarios, one including and the other excluding HT-ATES. The two LCOH's over time can be plotted to show the differences between the two scenarios. The results are found in Chapter 4.

2.2.5. Load factors, CO_2 emissions and costs

The load factor is an important output to study the actual usage of a specific energy supplier. It is defined as the factor between the total theoretical maximum energy output versus the actual energy output ($L_f = E_{actual}/E_{max,theoretical}$). To give an example, when the geothermal doublet is able to provide 20 MW of power throughout the year, but only fully supplies for eight months and provides nothing for the other four months, the load factor is 0.67. When implementing HT-ATES, the heat from the deep geothermal used to fill the HT-ATES also is used heat and therefore is included in the load factor. In theory, when all excess heat is stored, the geothermal load factor would be 1. However, due to heat losses in the storage system, not all the stored energy can be used, therefore the energy output of the HT-ATES is used in the load factor calculations. Therefore, for the HT-ATES the E_{actual} is the total annual energy output used to provide heat in the heat network and the $E_{max,theoretical}$ is the total amount of heat stored directly from the geothermal doublet.

When the amount of supplied heat is known, it can easily be calculated what the total CO_2 emissions are, based on the values shown in Table 2.1. The total annual CO_2 emissions are obtained by taking the annual heat supplied per source and multiply this by the CO_2 emission factor. One is also able to calculate the total costs of the emissions by using the CO_2 tax, of 125 €/ton CO_2 (PWC, 2022). All relevant values are found in Table 2.1 and the results for the base case are provided in Chapter 4.

2.2.6. Recovery efficiency

Recovery efficiency can not directly be retrieved from the HT-ATES performance simulations and therefore it is calculated in this model. The recovery efficiency is an indication of what part of the heat that was initially stored in the subsurface can be extracted again.

This is also a function of time, since in the first couple of years the efficiency is expected to be lower due to the fact that the aquifer needs to heat up. Some of the heat stored in the grains cannot be extracted afterwards. The recovery efficiency can be obtained using Equation 2.13.

$$RE = \frac{\sum_{t=0}^{n} E_{t,out}}{\sum_{t=0}^{n} E_{t,in}} = \frac{\sum_{t=0}^{n} E_{t,out}}{\left(\frac{Q_t \rho_t c_w (T_{t,hot} - T_{t,warm})}{V \cdot \delta t}\right)} \tag{2.13}$$

The recovery efficiencies can be calculated in the model for all years for which data is provided from the CMG GEM simulations and it can be plotted over time to study the increase in recovery efficiency.

3
Methodology

This Chapter provides an overview of the parameters affecting HT-ATES economic feasibility, where after the input parameters for the base case are listed. Also the approach of the sensitivity study is explained.

3.1. Overview of the parameters affecting HT-ATES feasibility

In order to be able to design a tool to predict high-temperature storage feasibility, one must first have information on what could be affecting parameters. These parameters are subdivided into three sections: geological, operational and economic parameters. The geological parameters are included in the HT-ATES performance simulator, the economic ones in the Python feasibility assessment tool and the operational parameters are covered in both models.

3.1.1. Geological parameters

The first set of parameters has to do with the subsurface characteristics. The list, together with their units, is shown in Table 3.1.

Some of these subsurface characteristics can have a big impact on the storage process, whereas others only have a very small influence. This already was discussed in the Introduction in Chapter 1 and results from the HT-ATES performance simulator and feasibility assessment tool will provide more information on what the key parameters are for influencing

Table 3.1: Geological parameter overview

Parameter	Unit
Porosity	-
Permeability (x-y-z directions)	mD
Heterogeneity	-
Groundwater flow	$\frac{m}{day}$
Aquifer depth	m
Aquifer temperature	°C
Aquifer dimensions	m
Rock specific heat capacity	$\frac{J}{kg \cdot K}$
Water specific heat capacity	$\frac{J}{kg \cdot K}$
Bulk thermal conductivity	$\frac{J}{m \cdot s \cdot K}$

Table 3.2: Operational parameter overview

Parameter	Unit
Injection/production temperature	°C
Injection/production rate	$\frac{m^3}{day}$
Injection/production period	days
Well screen depth	m
Well screen length	m
Well spacing	m
Storage volume dimensions	m
Lifetime	years

Table 3.3: Economic parameter overview

Parameter	Unit
Heating network temperature	°C
Heating network demand	MW
Electricity price	€/MWh
Capital Expenses (CapEx)	€
Operating Expenses (OpEx)	€
Discount rate	-
Subsidies	€

economic feasibility. Birdsell, Adams, and Saar (2021) states that a minimum transmissivity is required in the aquifer in order for the project to be economically viable. Since transmissibility and permeability represent the same physical meaning (of Gaza, 2011), this would indicate a high dependence on permeability and therefore, in Chapter 5, results are shown with multiple permeability realizations.

3.1.2. Operational parameters

The second set of parameters are operational-related. They care presented in Table 3.2. According to Dinkelman (2019), the injection and production temperature and the storage volume highly affect the recovery efficiency of the stored heat. Other operating parameters tend to have a smaller effect, but can still combine to have some significant effect so they should still be taken into account. Some of the parameters described in Table 3.2 are considered to be operational, however, they might also be a function of the geological parameters. To give an example, well screen depth and length and storage volume dimensions are defined by local geological conditions such as depths of suitable aquifers and their thicknesses.

3.1.3. Economic parameters

The last set of parameters is found in Table 3.3, which represent the economic parameters affecting HT-ATES feasibility. This set of parameters is the one that is most controlled by external factors, either directly dependent on the storage conditions or on things like the heating network or electricity prices. However, this does not mean these parameters are unimportant, as they can highly affect the final business case.

3.2. Case study Delft and parameter study

In order to answer the main research question and to validate the final tool that is created for HT-ATES feasibility prediction, a case study is performed on a specific location. For this research, there it is looked into HT-ATES implementation in the TU Delft Campus heating network. Afterward, an overview is given on what scenarios are performed to study the effect of these parameters on the final results.

3.2.1. HT-ATES in Delft

Current situation

The main reason why the HT-ATES implementation on the TU Delft Campus is chosen, is because there already is some valuable information present from the Window Phase 1 report (Bloemendal et al., 2020). This report contains technical feasibility assessments on multiple topics, information on policy and permits and financial feasibility studies. One other aspect in the decision-making was the fact that compared to other locations, the location in Delft has a high-volume storage potential and low nominal costs, as obtained from the Window report 'Comparison and selection locations' (Zwamborn, Kleinlugtenbelt, De Man, Schaaf, & Mars, 2020).

Input parameters

Technical model

In CMG GEM, both operational and geological/subsurface parameters are defined to simulate the storage system in Delft. These parameters, including the used values, are found in Table 3.4.

Hydraulic conductivities for both the aquifer and the confining layers are obtained from TNO (2022). Since GEM requires permeability as an input, the hydraulic conductivities are converted according to Equation 3.1.

$$k = \frac{\kappa \mu_T}{\rho_T g} \tag{3.1}$$

Where k is permeability $[m^2]$, κ is the hydraulic conductivity $[m/d]$, μ_T the fluid viscosity $[Pa \cdot s]$ and ρ_T the fluid density $[kg/m^3]$ at temperature T and g the gravitational acceleration constant $[m/s^2]$. For the rock compressibility, it is assumed that the Maassluis formation is an unconsolidated sand and therefore Baker and Jensen (2015) is used.

The well spacing is dependent on the thermal radius of the stored hot water, which is in its place dependent on water and bulk specific heat capacities, total screen length and the stored volume. The formula used to obtain the thermal radius can be found in Equation 3.2 (Bloemendal, 2021).

$$R_{th} = \sqrt{\frac{c_{p,w} V}{c_{p,b} \pi L}} \tag{3.2}$$

A rule is applied that states that the well spacing should be 2.2 times the thermal radius of the wells. In the base case this is also applied, whicht results in a spacing of the wells of 200 meters.

The well diameter would normally be dependent on the flow rate, aquifer hydraulic conductivity and the screen length. A minimum well diameter is applied to make sure that no sand is produced during the production stages of the wells. When the conditions require very large

Table 3.4: Operational and Geological/Subsurface parameters for base case scenario (Bloemendal et al., 2020) (Baker & Jensen, 2015)

Operating parameter	**Value**	**Unit**
Screen length	Aquifer thickness (50m)	m
Injection/production rate	4800	$\frac{m^3}{day}$
Injection/production duration	182.5	Days
Total storage volume	876,000	m^3
Injection T	80	°C
Return T	50	°C
Number of hot wells	1	-
Number of warm wells	1	-
Well spacing	200	m
Well radius	0.5	m
Geological/Subsurface parameter	**Value**	**Unit**
Permeability I-J directions aquifer	10	Darcy
Permeability K direction aquifer	1	Darcy
Permeability I-J directions conf. layers	0.005	Darcy
Permeability K direction conf. layers	0.0005	Darcy
Porosity	0.30	-
N/G	1	-
Rock compressibility	$5.15e^{-4}$	kPa^{-1}
Rock specific heat capacity	1000	$\frac{J}{kg \cdot K}$
Bulk thermal conductivity	1.60	$\frac{J}{m \cdot s \cdot K}$
Aquifer thickness	50	m
Groundwater flow	0	$\frac{m}{day}$
Top depth	130	m
Ambient T	15	°C
Heterogeneity	None	-

well diameters, it can be chosen to drill multiple wells where the hot wells are concentrated as close to each other as possible . However, since the grid cells in the aquifer near the well are 8 by 8 meters, the resolution is too low to include these multiple wells and a single well is used in the simulations.

Economics model

When constructing the business case for the case study in Delft, the costs calculations are based on the data provided in Table 2.1. This is done to make sure that the model is not only able to construct a business case for the scenario in Delft but also for other locations. However, there are some parameters that are specific for this case study, which are provided in Table 3.5.

Table 3.5: Economic parameters for base case scenario (Bloemendal et al., 2020)

Operating parameter	**Value**	**Unit**
Lifetime	30	Years
r	0.055	-
η_{pump}	0.5	-
Gas price	100	EUR/MWh

3.2.2. Parameter study

In Table 3.6, an overview is given with all different scenarios. One must note that only the changed parameters are highlighted and that all other values are equal to the ones provided in Table 3.4.

Table 3.6: 22 different scenarios with different geological or operational aspects

Scenario	Parameter	Value	Unit
1	Inj/Prod rate	1100	$\frac{m^3}{day}$
	Well spacing	96	m
2	Well spacing	160	m
3	Well spacing	232	m
4	Screen length	Upper half	-
	Well spacing	280	m
5	Injection T	90	°C
	Production T	60	°C
6	Injection T	90	°C
	Production T	30	°C
7	Injection T	70	°C
	Production T	40	°C
8	k_i, k_j aquifer	50	Darcy
	k_v aquifer	5	Darcy
9	k_i, k_j aquifer	1	Darcy
	k_v aquifer	0.1	Darcy
10	ϕ	0.10	-
11	c_r	$5.15e^{-3}$	kPa^{-1}
12	$c_{p,r}$	710	$\frac{J}{kg \cdot K}$
13	K	2.10	$\frac{J}{m \cdot s \cdot K}$
14	Aquifer thickness	20	m
	Well spacing	336	m
15	Aquifer thickness	100	m
	Well spacing	152	m
16	Ambient T	40	°C
17	Groundwater flow	0.03	$\frac{m}{day}$
18	One 1m thick clay layer	-	-
19	Two 1m thick clay layers	-	-
20	5-spot pattern geometry	-	-
21	INJ/PROD following demand curve	-	-
22	5 months loading, 7 months production	-	-

After these scenarios are simulated, it is further looked into a couple of important parameters affecting recovery efficiencies, including storage volume, permeability and the temperature difference between the two wells. The ΔT is changed by adjusting the return temperature, so the temperature in the warm well. A total of 27 simulations are performed, where for all three parameters, three values are taken and all combinations are simulated. The values are found in Table 3.7.

Table 3.7: Using the values for these three important parameters, a total of 27 simulations were performed

Storage volume [m^3]	**Permeability [Darcy]**	**ΔT [°C]**
200,000	10	20
600,000	50	30
1,000,000	100	40

The effect of storage volume is investigated separately as well. There is only one other parameter that changed as well for these runs, namely the well spacing. The same relationship, as shown in Equation 3.2, is used to determine the well spacing based on the thermal radius of the storage in the hot well.

Table 3.8: Values used to further investigate the impact of storage volume

Storage volume [m^3]	**Well spacing [m]**
200,000	96
400,000	136
600,000	167
800,000	192
1,000,000	215

Since the prediction is that permeabilities in the aquifer will play an important role in the total heat recovery, this specific parameter is studied in further depth. At first, some simulations are performed using different permeability realizations, while keeping the factor between horizontal and vertical permeability constant at 10/1. The smallest values in the range, like 0.1 and 1 Darcy for the k_h, just as the 200 Darcy might not be the most realistic values for HT-ATES aquifers. However, it is good to include these to give a good overview of the effect of permeability on the recovery efficiency.

Table 3.9: Values used to further investigate the impact of permeability

Horizontal permeability [Darcy]	**Vertical permeability [Darcy]**
0.1	0.01
1	0.10
10	1.0
25	2.5
50	5.0
100	10
200	20

In the next round of simulations, the ratio between k_h and k_v is changed. This likely shows results that can indicate what the decisive direction of permeability is to obtain good recovery efficiencies. All combinations of the values provided in Table 3.10 are simulated.

Table 3.10: Values used to further investigate the relationship between vertical and horizontal permeabilities. A total of 12 simulations are performed using all combinations of the permeabilities shown in this Table.

Horizontal permeability [Darcy]	**Vertical permeability [Darcy]**
1	1
10	5
50	10
100	

Not only the geological and operational parameters affect the final business case of the project. Economic parameters can also highly influence the final decision whether or not to implement HT-ATES in the network. The economic parameters discount rate, average gas price, HT-ATES CAPEX, CO_2 tax and the average electricity price are all plotted versus the project LCOH for two scenarios; a heat network in- and excluding high-temperature storage. This is done to study the impact and therefore the importance of these parameters in the final decision making.

4

Results: Base Case

In this Chapter, all results obtained from this case study are shown and explained.

4.1. Results HT-ATES performance simulator

Well bottom-hole temperatures for both wells are plotted over time in Figure 4.1. The first period, from May 1st until October 31st 2011 is used for injecting the hot water in the hot well; water is extracted at the same volumetric rate from the warm well, which is still at the initial temperature of 15 °C. In the Figure, this is the first part, until the hot-well temperature drops and the warm-well temperature remains at 50 °C. From November 1st, 2011, the processes turn around where heat is being produced from the hot well and re-injected at 50 °C in the warm well. In the Figure, this is the time interval between the hot-well temperature drop and where it goes up to 80 °C again. 4.5 more cycles are simulated as well in this case.

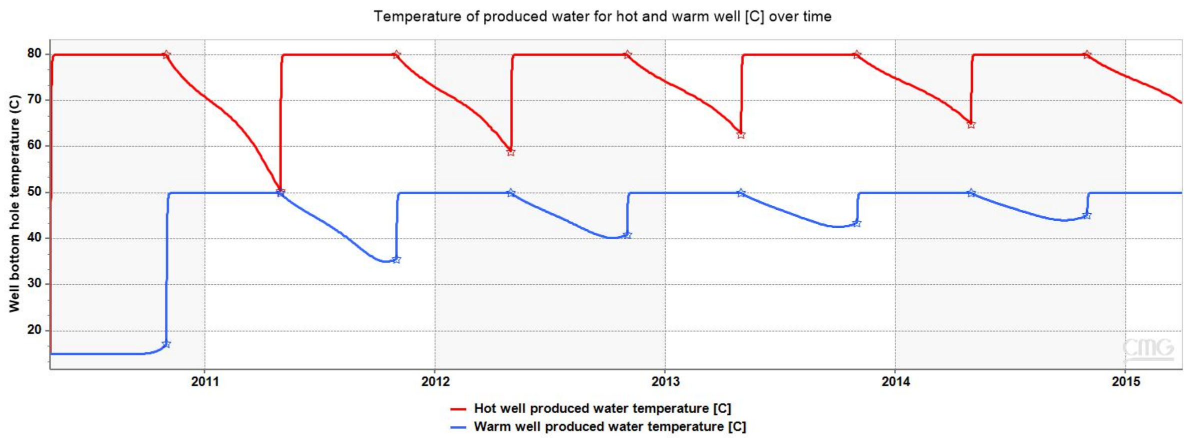

Figure 4.1: Temperature of produced water for hot and warm well over time

The well bottom-hole temperatures show that in the first couple of cycles, the temperature profile differs every year. After a total of four cycles the profiles become constant, which is in line with Figure 2.6 from Section 2.1.1. This is due to the fact that in the first couple of years, heat is transferred from the fluid into the rock where some of the heat cannot be extracted anymore. This process holds for both the hot as the warm well, although the effect is more visible near the hot well, since temperature differences are larger.

In Figure 4.2, the simulated temperature distribution in the underground after exactly three cycles is plotted, so at the end of hot-water extraction.

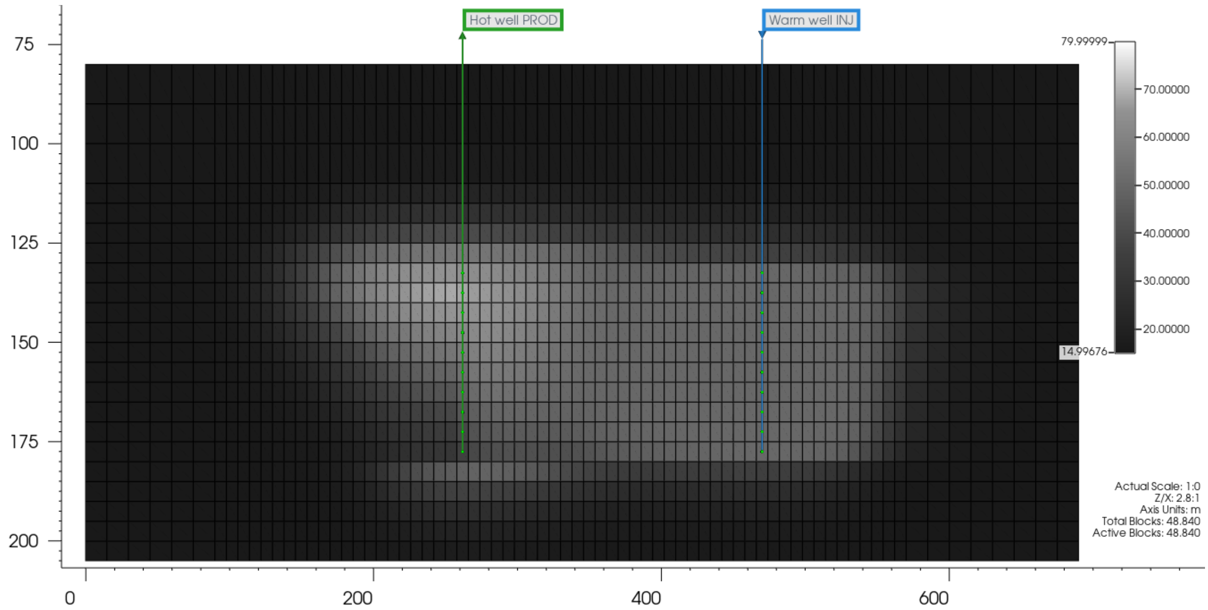

Figure 4.2: Vertical cross-section of the temperature profile after three cycles, just before hot-water injection of fourth cycle. The aquifer is at the 130 - 180 meter interval.

The vertical cross sectional temperature profile shows that there is an area around the wells that still is warmer than the surroundings; heat that is contained in the grains after extracting the hot water. The thermal radius around the wells is not homogeneous over the full aquifer thickness. The vertical permeability was high enough to allow buoyancy flow; hot (less dense) water transported to the aquifer top. This is the case at both sides; for the hot and warm well. However, the angle of the plume is higher at the left side; the hot well compared to the warm well. This can be explained by the fact that the temperature difference, and therefore density difference, was higher near the hot well. Therefore density-driven forces are higher.

One other element that is obvious from Figure 4.2 is the warm region in the confining clay formation right below the hot well. At the bottom of the aquifer the cold water has almost reached the well, however, in the clay layer still some heat is stored. This is because of the fact that conduction is the main heat transfer process in the clay layer and thus this part takes longer to cool down compared to the aquifer on top where heat convection also plays a role. From the simulation outputs is retrieved that a total of $1.3e^{14}$ J of energy is stored in the top confining clay formation at this point. The bottom formation, however, only contains $8.0e^{13}$ J of heat and in the aquifer itself $7.2e^{14}$ J is still present. This means that after a total of three cycles, 14% of the remaining heat is present in the top clay formation, 77% is present in the aquifer itself and the remaining 9% is in the bottom confining clay layer.

In Figure 4.3, the simulated temperature distribution in the underground is plotted. This illustrates the extend of the hot-water plume right after all heat is stored. This is after exactly 3.5 cycles.

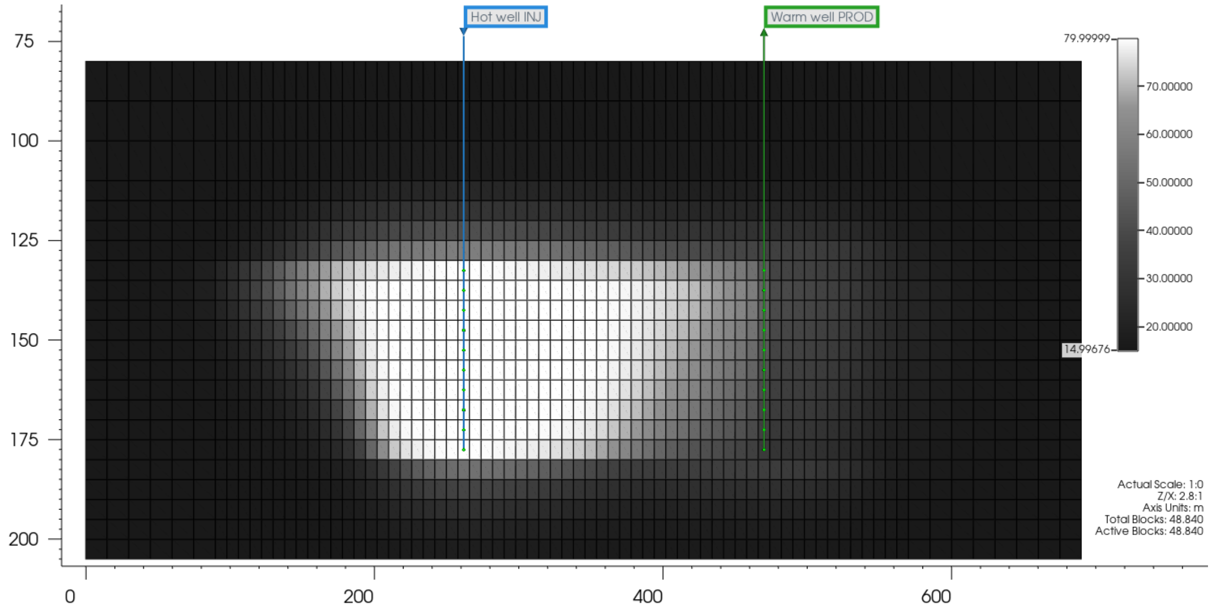

Figure 4.3: Vertical cross-section of the temperature profile after 3.5 cycles, just after hot-water injection of fourth cycle. The aquifer is at the 130 - 180 meter interval.

Figure 4.3 shows that the temperature in the system now is much higher compared to after extraction via the hot well. The hot-water front does stretch more to the right, to the warm well, compared to other directions. This is due to the pressure difference between the wells which is higher compared to the pressure difference with the hot well and the aquifer. A larger pressure difference results in more fluid flow when other influencing parameters such as fluid mobility and reservoir permeability are kept constant.

The aerial view of the temperature profile at the exact same point in time as Figure 4.3, can be seen in Figure 4.4.

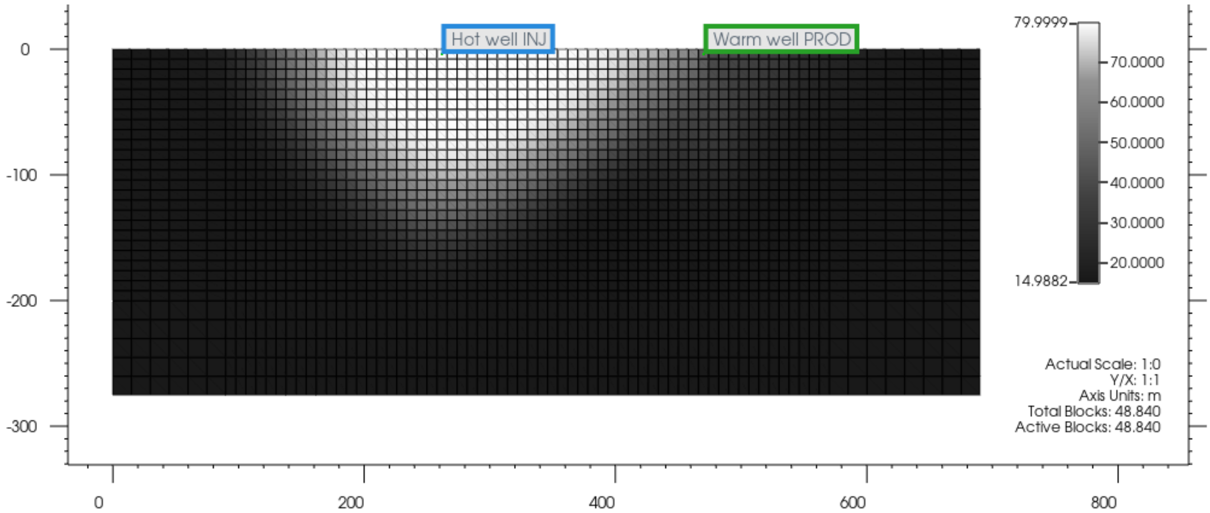

Figure 4.4: Horizontal cross-section at model top of the temperature profile after 3.5 cycles, just after hot-water injection of fourth cycle. Located at the top cell interval of the aquifer.

Figure 4.4 shows that the heat is spread out radially, due to homogeneous reservoir conditions and radial flow from the well. However, due to short-circuit flow with the warm well, the heat front propagates further towards the warm well. This is the same effect as seen in Figure 4.3.

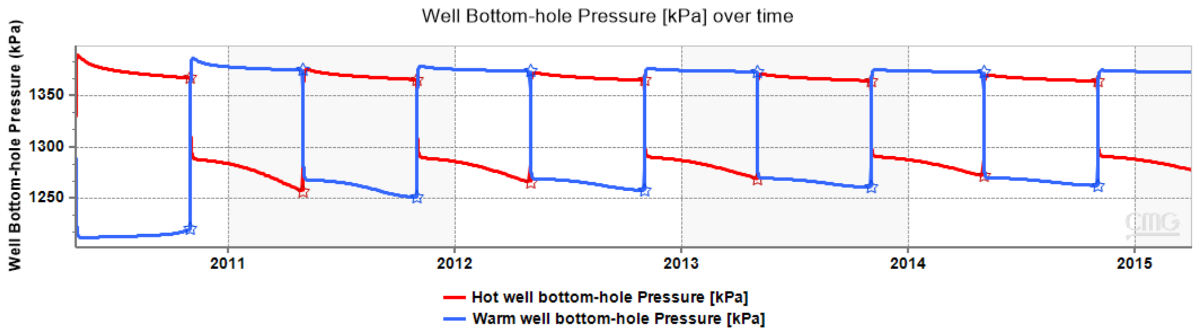

Figure 4.5: Hot and warm well bottom hole pressures over time

For both wells, bottom hole pressures over time are given in Figure 4.5. The injection and production periods are clearly visible; after every 6 months there is a pressure change in both wells as a result of the change in flow direction. During each injection or production periods, pressures in both wells are not constant, as is the pressure difference between the two. This is to make sure the same volumetric flow rate at the surface is maintained, while changes in temperature in the aquifer change the fluid viscosity. Higher fluid temperatures result in lower fluid viscosities and therefore higher fluid mobilities. This means that when the system heats up over time, the pressure difference between the wells can be decreased while maintaining a constant volumetric flow rate. During the first hot-water injection period, from May to November 2011, the system heats up and the pressure difference decreases over time. In the first hot-water extraction period, from November 2011 until May 2012 in Figure 4.5, the heat is extracted so fluid viscosities in the aquifer increase. This results in a larger Δp between the wells to maintain the flow rate. One can see in Figure 4.5, that over time the changes in pressure decline, because in general the system will heat up in the first couple of cycles.

One can also see in Figure 4.5 that during production periods of the hot well, the pressure decline is faster compared to the pressure decline in the warm well during extraction. This also has to do with the fluid mobility, the temperature differences are larger near the hot well so the pressure adjustments are larger to maintain the constant flow rate.

4.2. Results Python feasibility assessment tool

Figure 4.6(a) shows the annual demand curve of the TU Delft campus, subdivided for each of the three heat suppliers. In Figure 4.6(b), an overview is given of how much heat is provided by each of these three sources.

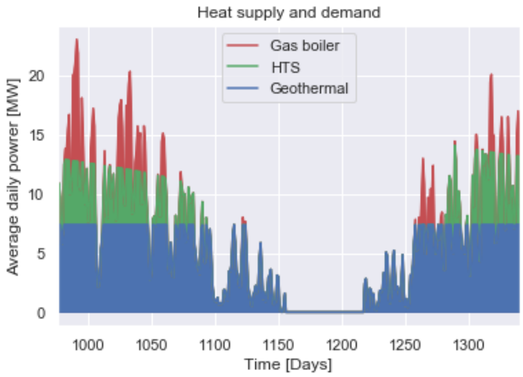

(a) Annual heat demand and supply per heat source

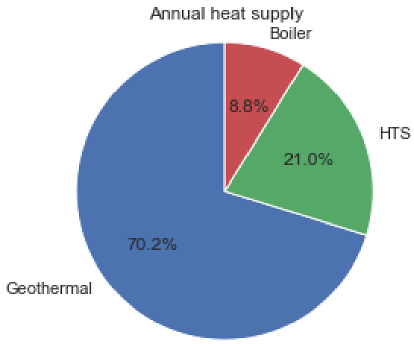

(b) Pie chart of the heat supply per source

Figure 4.6: Heat demand per heat source

In Figure 4.6(a), one can see a decline in power for the HT-ATES over time. The power output is dependent on the flow rate, fluid density, specific heat and temperature differences between the wells, as was shown in Equation 2.9. When flow rates, fluid density and specific heat are assumed to be constant, the only factor of influence on HT-ATES power output is the temperature difference. The decline in the green curve in Figure therefore is a result of the temperature decline of the water extracted from the hot well.

In Figure 4.6(b), one can see how much of the total demand is covered by which supplier. The geothermal doublet is the main heat supplier and it is logical that the heat storage system cannot supply as much, since it depends on the excess heat from the geothermal system. However, the part that normally would be covered by a gas boiler, a significant amount of energy can now be supplied by a green alternative.

In Figure 4.7, the development of the HT-ATES recovery efficiency over the simulation period is presented. This illustrates the increase in performance like was also identified by (Van Lopik et al., 2016) over 4 cycles. In year 1 the recovery efficiency is **0.55**, whereas in year 4 this already is **0.75**.

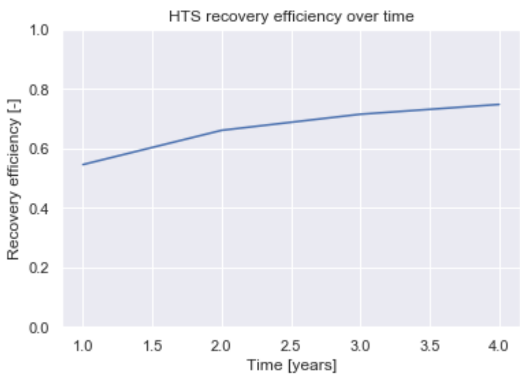

Figure 4.7: Recovery efficiency of the base case over time

The total pumping costs over the four cycles are shown in Figure 4.8(a). In Figure 4.8(b), the LCOH is plotted for two scenarios; one including and the other excluding the heat storage. Note that the LCOH is not a function of time, but a single value obtained at the end of the lifetime of a project. In this case, for the scenario including HT-ATES this will be **52 €/MWh**. However, when only making use of geothermal energy and the gas boiler, the final LCOH would be **61 €/MWh** after 30 years. To plot the LCOH as is done in Figure 4.8(b) still gives some valuable information about the minimum lifetime of the project.

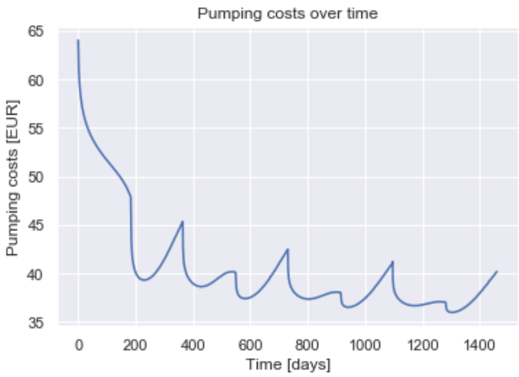

(a) HT-ATES Pumping costs over first four cycles

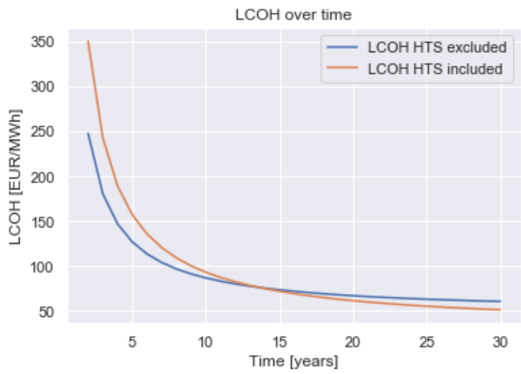

(b) LCOH for the two scenarios

Figure 4.8: Pumping costs and LCOH over time

In Figure 4.8(a), one can see that there are peaks at every change in flow direction. Also the general trend goes down, this is due to the heating of the system and therefore the fluid becomes less viscous. This increases fluid mobility and therefore a smaller pressure difference is required to accommodate for the constant flow rate.

In Figure 4.8(b), the levelized costs are higher for the heat storage scenario when project lifetimes are short, however, the lines cross after **13.6 years**. This difference is due to the relatively high investment costs accompanied with the red scenario (HT-ATES included) and the lower operational expenses. The lower levelized cost indicates that for lifetimes exceeding 13.6 years this scenario is the preferred one.

The geothermal load factor including the heat used for the HT-ATES is **0.75**. This is the load factor when considering the total energy output of the geothermal doublet combined with the HT-ATES. When there would be no heat storage system in place, this geothermal load factor would drop to **0.60**. The HT-ATES load factor is **0.57**.

These load factors show that HT-ATES implementation significantly improves the total usage of the deep geothermal source. However, the HTS 'only' provides 57% of its maximum output throughout the year. It would be better to improve this number, but there is also another side to it. When the portion of heat provided by geothermal energy and the heat storage system combined in the total heat demand becomes smaller, the portion of green heat declines while the load factor increases. A balance should be found where their load factors do not become too small while still supplying a significant amount of green heat to keep CO_2 emissions low. Where this balance is found, is a matter of priorities. Higher load factors result in more cost-efficient usage of the specific heat providers, but increasing the total portion of heat provided by the green suppliers (geothermal and HT-ATES) will result in lower total CO_2 emission.

The economics assessment tool also provides information regarding the CO_2 emissions of both scenarios, in- and excluding the HT-ATES. Emissions from the geothermal will remain constant in both cases when the emitted CO_2 from filling the HT-ATES is counted as HT-ATES CO_2 emissions. The annual geothermal emissions will be **37 tons**. The total emissions for the heat storage are **43 tons** per year and the gas boiler emits **41 tons** when HT-ATES is implemented. However, without HT-ATES, the boiler would annually emit a total of **138 tons** of CO_2. This means the total CO_2 savings by the heat storage in this case will be **31%**. This is quite significant, especially considering Figure 4.6(b) where one can see that the largest heat supplier is geothermal, where nothing changes regarding CO_2 emissions between both scenarios. The heat supply by the gas boiler is reduced from 29.8 to 8.8% which is the driver for the reduction in emissions.

5

Results: Sensitivity analysis

The results of the sensitivity analysis described in Tables 3.6, 3.7, 3.9 and 3.10 in Section 3.2.2, are described here, as well as plots showing LCOH as functions of discount rates and gas prices. Only the interesting results are highlighted in this Chapter, the results of the remaining scenarios can be found in the Appendix.

5.1. Parameter variation analysis

After running the first 22 scenarios, based on the input parameters from Table 3.6, an overview of the results is shown in the following Figures.

Figure 5.1 provides a first indication on how the recovery efficiency is affected by specific parameters. In this Figure, the blue horizontal line represents the recovery efficiency for the base case (the fourth cycle). Most scenarios are within the same range. The two main outliers to the negative side are scenarios 1, 9 and 14, which are the small storage volume, low permeability and small aquifer thickness scenarios, respectively. Some of the outliers to the positive side, scenarios with higher recovery efficiencies compared to the base case, are scenarios 6, 8, 15 and 16.

The smaller storage volume (scenario 1) in general results in more surface area compared to the total volume; the A/V ratio is higher. This enables more heat losses to the surroundings; either the rest of the aquifer or confining layers, depending mainly on the shape of the stored hot water.

Scenario 6 is the one where the temperature difference between the wells is higher, the water can cool down to 30 °C and initial hot-water injection temperature is at 90 °C. Due to the lower warm-well injection temperature, the difference between that well and the ambient temperature is lower, resulting in a higher recovery efficiency. The larger temperature difference dominates over the fact that the hot-water injection temperature is higher compared to the base case, which has a negative effect on the recovery efficiency, as obtained from scenario 5.

Scenarios 8 and 9 are the high and low permeability scenarios, respectively. Temperature distributions in the aquifer of these scenarios can be found in Figures 5.2 and 5.3. In Figure 5.2 can be seen that after the fourth time of hot-water injection, the thermal energy stored is mainly in the region near the top confining layer. The high vertical permeability allows the

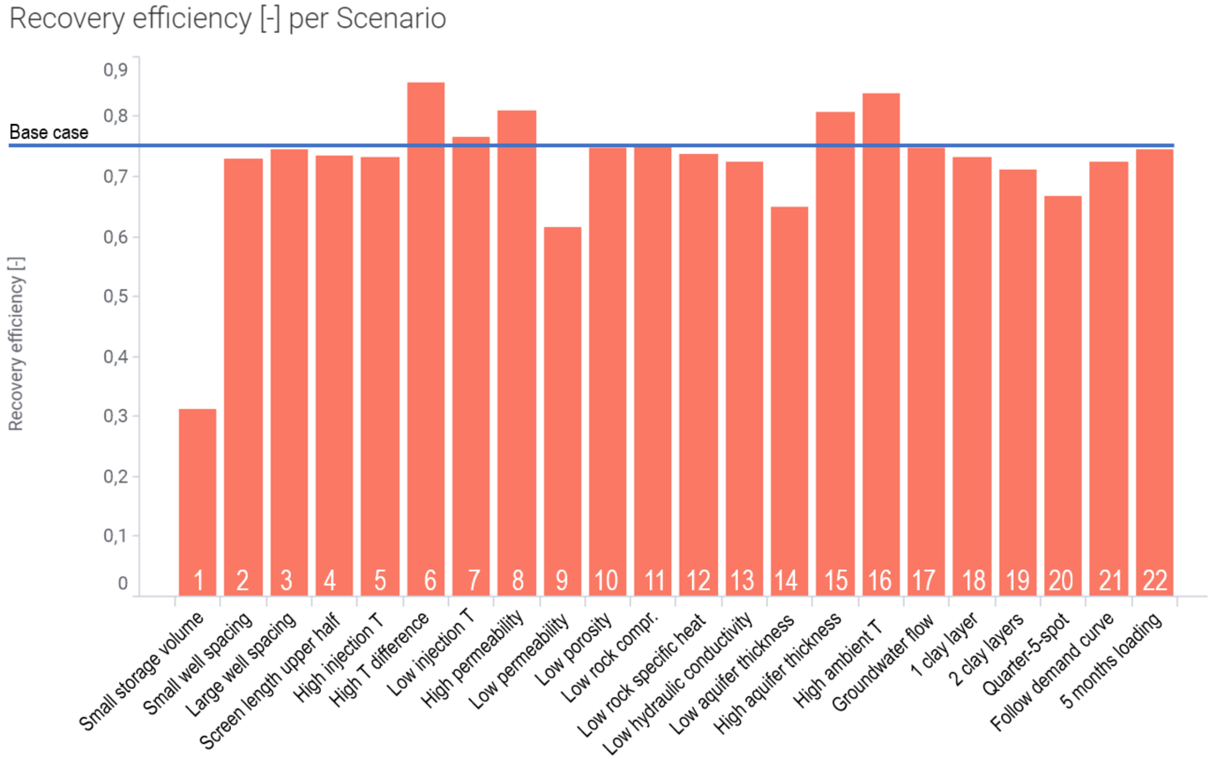

Figure 5.1: Recovery efficiencies for the fourth cycle for all scenarios as provided in Table 3.6

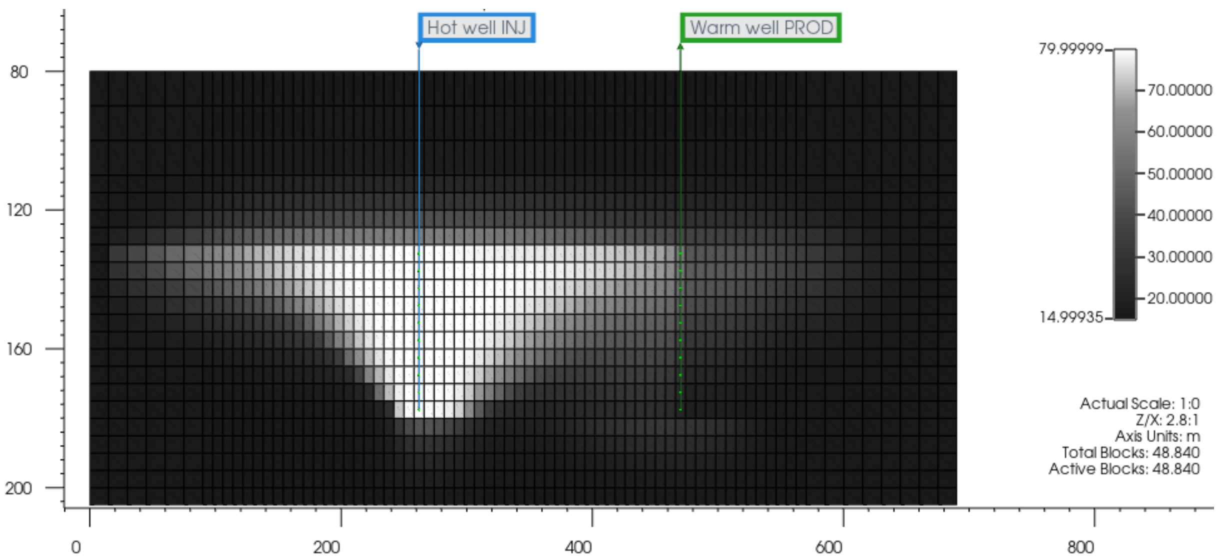

Figure 5.2: I-K temperature profile after exactly 3.5 cycles; right after the fourth hot-water injection period. Permeability: $k_h = 50D, k_v = 5D$. All other parameters are as provided in Table 3.4.

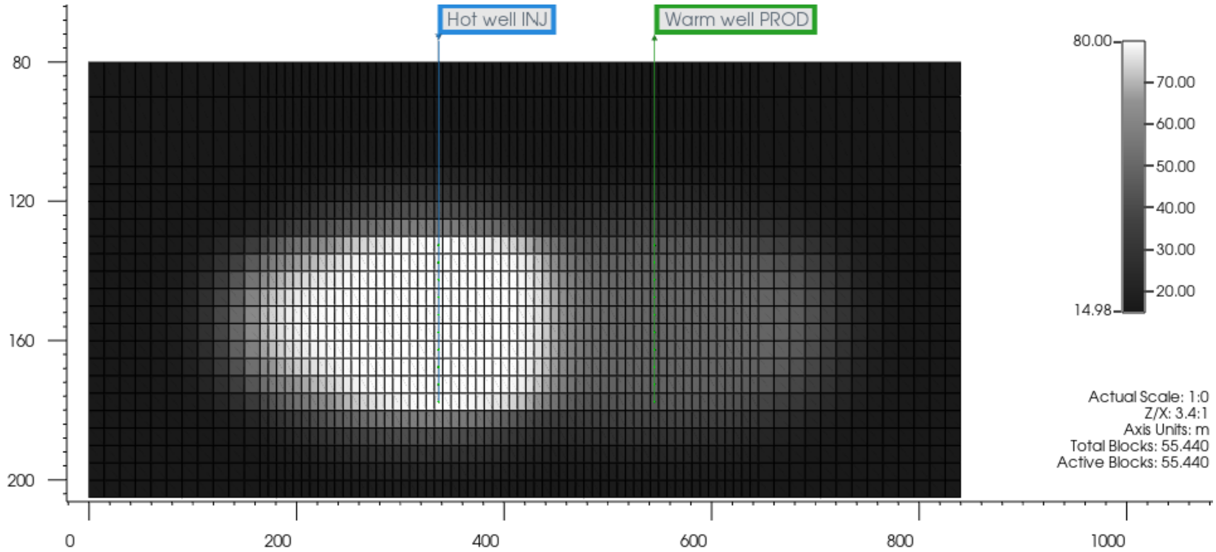

Figure 5.3: I-K temperature profile after exactly 3.5 cycles; right after the fourth hot-water injection period. Permeability: $k_h = 1D, k_v = 0.1D$. All other parameters are as provided in Table 3.4.

water to flow easily and the buoyancy flow takes place. However, when the permeabilities are low, as shown in Figure 5.3, the effect of buoyancy flow is extremely small. The hot-water bulk is still located around the well and over the full aquifer thickness. Near the bottom and top there is less heat, because in these locations some heat is lost via conduction to the clay layers.

The low permeability scenario in scenario 9 also indicates a lower recovery efficiency compared to the base case. The permeability in both horizontal as in vertical directions are ten times lower. This lower recovery efficiency can be explained by two phenomena, both influenced by the (lack of) buoyancy flow. Since more heat is stored near the bottom of the aquifer compared to the high permeability scenario, more heat losses take place into the bottom clay formation by heat conduction. The low permeability scenario is shown in Figure 5.3.

One other aspect is related to viscous forces along the well. Hot water has a lower viscosity at equal pressure compared to colder water, therefore higher flow rates can be found at the hotter intervals of the well. This can also be obtained from Table 5.1, where can be seen that for the high permeability scenario a large part of the produced water actually comes from the top intervals of the full aquifer thickness, more than twice as much as the bottom part. In this Table, both wells are subdivided into ten equally thick sections, according to grid cell dimensions. For all intervals, total flow rates are obtained at the end of the simulations. It is found that depending on the permeability, the flow rates differ per interval.

Table 5.2 provides proof for the processes just described. For two moments in time, the energy distribution in the system is provided. The factor of the total energy in the system that is stored in each specific part of the system is also given. One can see that for both moments in time, less heat is stored in the top confining layer for the low permeability scenario. However, more heat is stored in the bottom clay formation compared to the high permeability scenario.

Two scenarios that show different recovery efficiencies compared to the base case as well, are scenarios 14 and 15. These scenarios include different aquifer geometries, shown in Figures 5.4 and 5.5, the first one with a total thickness of 100 meters and the second being thinner, 20

Table 5.1: Flow rates per interval in the hot well for scenarios 8 and 9 at the end of the simulations

	Flow rates [$\frac{m^3}{day}$]	
Interval	**High k_h and k_v scenario (#8)**	**Low k_h and k_v scenario (#9)**
1 (top)	347.79	230.86
2	351.74	248.53
3	326.74	254.18
4	290.51	254.99
5	251.10	254.17
6	215.46	252.57
7	186.88	250.11
8	165.86	245.94
9	151.87	237.46
10 (bottom)	146.10	220.23
Total	**2400**	**2400**

Table 5.2: The amount of energy stored in the aquifer and confining layers before and after hot-water injection, after 3.5 and after 4 cycles.

		$k_h = 1D$,	$k_v = 0.1D$	$k_h = 50D$,	$k_v = 5D$
		Energy [e^{13} J]	**Factor [-]**	**Energy [e^{13} J]**	**Factor [-]**
3.5 cycles	Overburden	10.7	0.117	11.1	0.126
	Aquifer	71.7	0.786	69.0	0.784
	Underburden	8.91	0.097	7.90	0.090
	Total	**91.6**		**88.0**	
4 cycles	Overburden	11.8	0.101	17.4	0.150
	Aquifer	95.0	0.810	91.8	0.793
	Underburden	10.4	0.089	6.65	0.057
	Total	**117**		**116**	

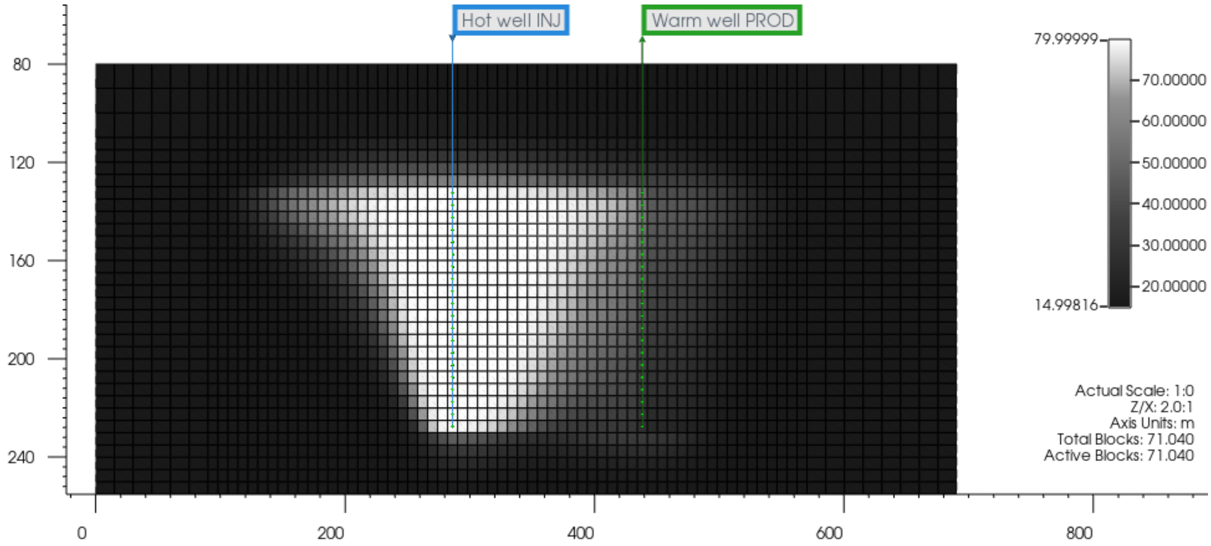

Figure 5.4: I-K temperature profile after exactly 3.5 cycles; right after the fourth hot-water injection period. Aquifer thickness: $h = 100m$.

meters. For these scenarios, well spacing is adjusted as well to accommodate for the different thermal radii. The well spacing in Figure 5.4 is 152m and in Figure 5.5 it is 336m. Keeping the well spacing equal for the different scenarios would make these less comparable since it can affect the system such that the hot water is already reproduced via the warm well. Therefore this approach is chosen.

One can see two very different shapes for the two situations. The thick reservoir results in a candy cane shaped hot-water plume with a small thermal radius. The top confining layer shows a significant increase in temperature due to heat conduction, where as the bottom does not contain much heat compared to the top. This is a result of the buoyancy flow that is clearly visible in this scenario. Also, it can be seen that the hot-water front stretches out further towards the warm well compared to the opposite direction, something that was also noticed in the base case in Chapter 4.

The low aquifer thickness in Figure 5.5 results in a pancake-shaped hot-water plume, where in this situation both wells are further away from each other. There is less contact with the colder parts of the aquifer due to the low thickness, however, both on top and at the bottom, more heat is lost to the impermeable confining formations due to conduction. This results in a lower recovery efficiency compared to the base case. Still it can be seen that the heat is concentrated near the top of the aquifer, but the buoyancy effect is small compared to the large thickness scenario.

The last one with a high recovery efficiency is scenario 16, as shown in Figure 5.1, where an ambient initial temperature of 40 °C is simulated. This decreases the difference between the stored and ambient temperature and therefore decreases heat losses, resulting in an increased recovery efficiency.

Figures 5.6 and 5.7 both show a situation where the subsurface does not consist of thick, vertically continuous high-permeable sand layers. These are scenarios 18 and 19 in Table 3.6. These scenarios do not vary significantly from the base case when comparing recovery efficiencies, however, in real situations these small clay layers are likely to be present in a lot

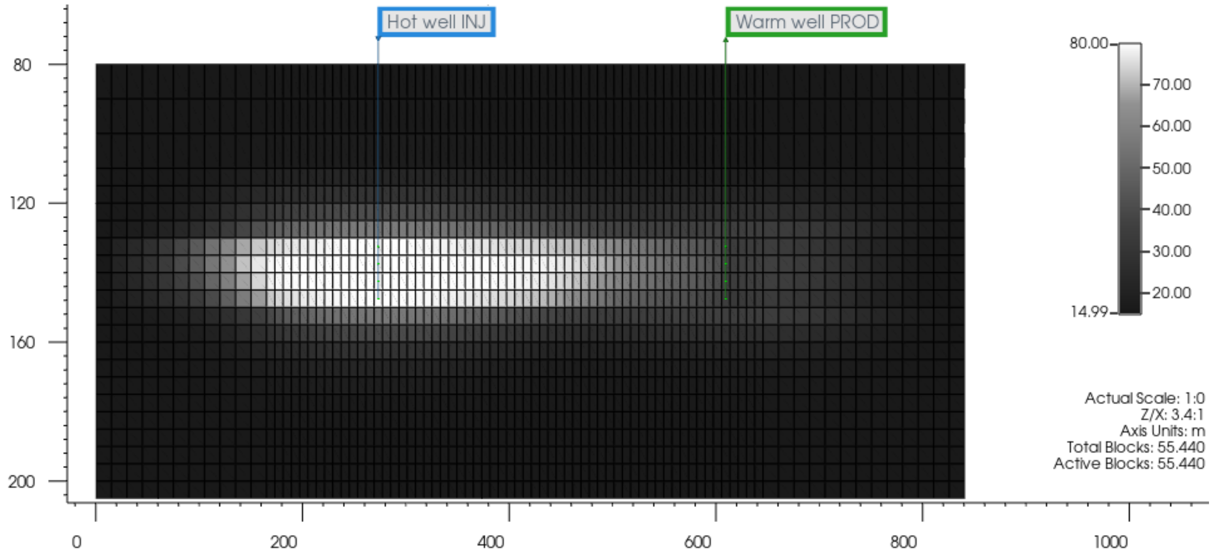

Figure 5.5: I-K temperature profile after exactly 3.5 cycles; right after the fourth hot-water injection period. Aquifer thickness: $h = 20m$.

of aquifers and therefore they are given some attention as well. In Figure 5.6, one 1 meter thick clay layer is positioned right in the middle of the sand and in 5.7 there are two thin layers present. Wells are completed in all permeable sections but not in the clays. One thing to note is that heat exchange between the different sand sections is still possible; in the form of heat conduction. However, the low vertical permeability of the clay prevents any heat convection to take place, whereas in absence of the clay layers the fluids can flow vertically more easily.

Figures 5.6 and 5.7 show that for every section, the buoyancy effect drives the water to create similar shapes as shown in previous temperature profiles, now stacked on top of each other. The thin clay layers have adsorbed a significant amount of heat, but over the full area are not as warm as the surroundings. When looking at the profile after the hot-water extraction, this is actually reversed; the clay layers contain more heat than the sand formations. This is due to the lack of convection and therefore the heating and cooling processes are slower than in the sands.

In Figure 5.8, the total energy output versus LCOH is plotted for all scenarios. Also, an interpreted trendline is drawn that intersects most of the points, indicating that in general there is a correlation between the two parameters; the higher the energy output the lower the LCOH. This can be explained by the fact that the variable OPEX of the HT-ATES are significantly lower than of the gas boiler, so the more heat can be provided by the heat storage system, the lower the total OPEX. There are however, three clear outliers in this plot.

The first one is scenario 9, the low permeability scenario. This can be explained by the variable OPEX as well. The HT-ATES pumping costs for this scenario are very high, increasing the total costs per MWh delivered. The second outlier is the scenario where the temperature difference is larger, 60 °C instead of 30 °C. As can be obtained from Equation 2.9 in Section 2.2, a larger temperature difference results in a higher HT-ATES power and therefore energy output. The third outlier is the small storage scenario, which has a lower enery output and a higher LCOH compared to most other scenarios. This can be explained by the low recovery efficiency as already provided in Figure 5.1.

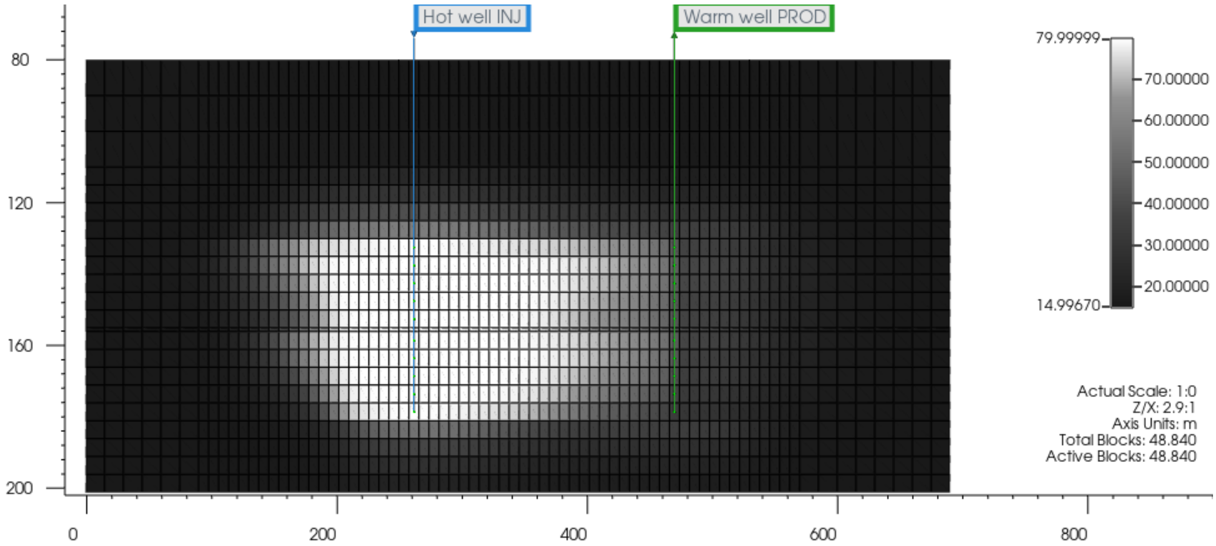

Figure 5.6: I-K temperature profile after exactly 3.5 cycles: right after the fourth hot-water injection period. One clay layer.

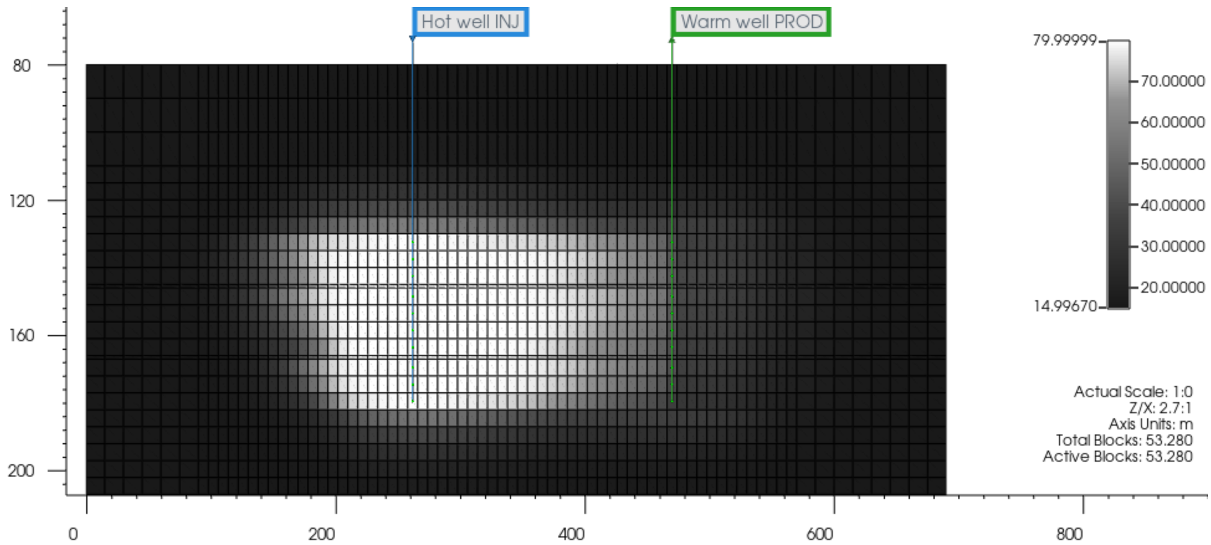

Figure 5.7: I-K temperature profile after exactly 3.5 cycles: right after the fourth hot-water injection period. Two clay layers.

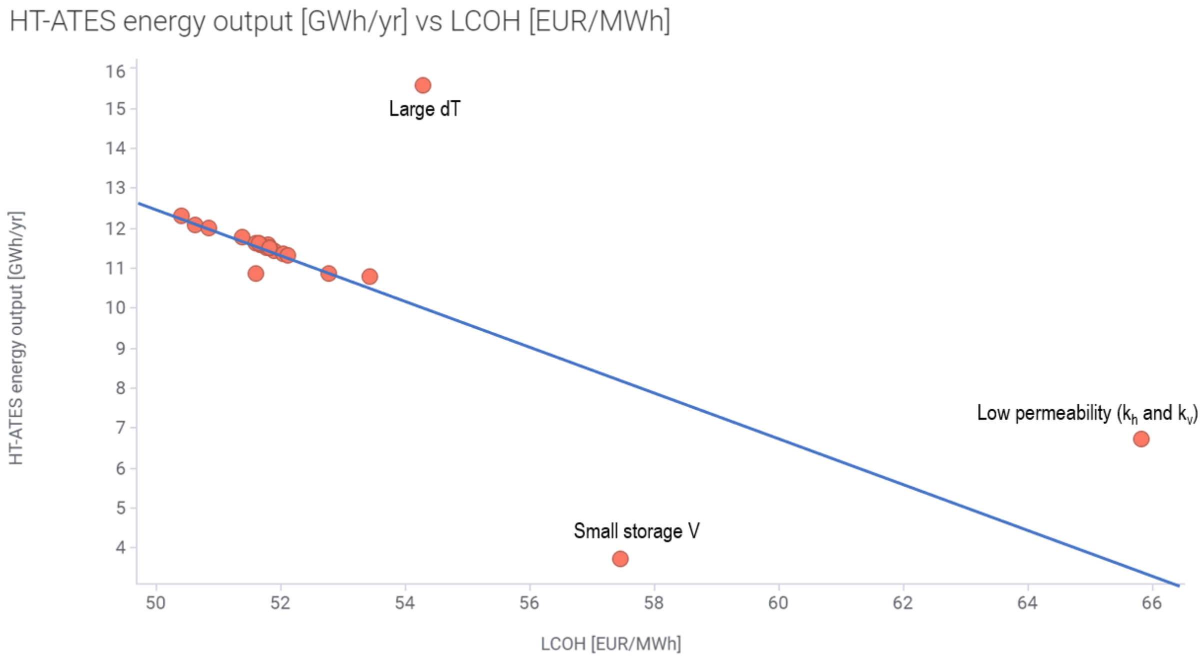

Figure 5.8: HT-ATES energy output versus LCOH for the scenarios as provided in Table 3.6

5.2. Study on storage volume, permeability and temperature difference

Figure 5.9 shows the recovery efficiency in year four plotted versus the LCOH. The 27 runs as provided in Table 3.7 are plotted, where each point also provides information about temperature difference between the wells, horizontal permeability and storage volume.

When having a closer look at the impact of ΔT (colors in the plot), one can see that higher temperature differences result in higher recovery efficiencies and a lower LCOH in all scenarios. This means that a higher temperature difference between the wells is always preferred compared to a lower ΔT.

The storage volume (different sizes in the plot) also shows a clear pattern when comparing different volumes where the other parameters are kept constant. It shows that a larger storage volume in all scenarios results in a lower LCOH and higher recovery efficiencies. However, at large storage volumes the 50 Darcy scenario is the optimal one, while for the smallest storage volumes the lowest horizontal permeability of 10 Darcy is preferred.

This has to do with the shape of the stored heat in the subsurface, which is dependent on multiple parameters such as aquifer thickness, permeability, storage volume and injection temperature. When storing a different volume in an aquifer with the same thickness, the shape is different and therefore the A/V ratio differs as well. This can result in deviating recovery efficiencies. From Figure 5.9 there can be retrieved that these different subsurface geometries also have different optimal horizontal permeabilities.

One can also obtain from the plot that when keeping the storage volume constant, there is more spreading between the results when the temperature difference between the two wells is smaller. This is clear especially for the high-volume scenarios and when looking into the LCOH. The lower temperature difference results in a lower HT-ATES power output and there-

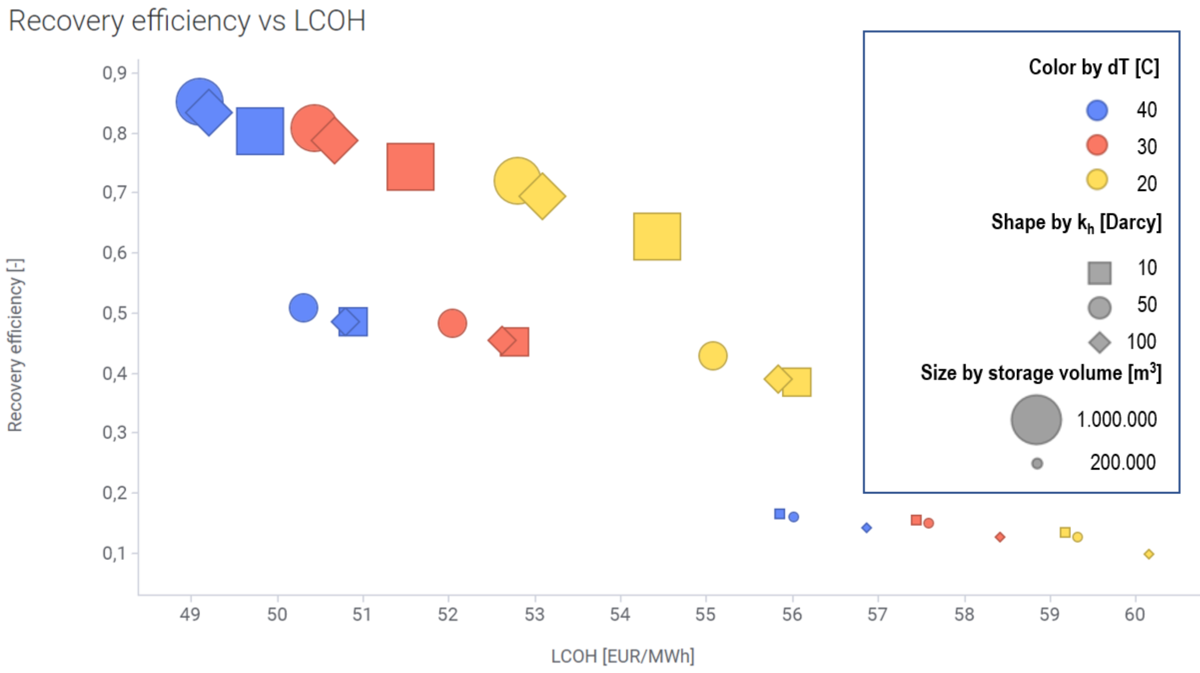

Figure 5.9: Recovery efficiency in year 4 versus LCOH

fore a larger part of the heat demand is covered by the gas boilers. For every step in ΔT between the wells, this fraction of heat supplied by the boiler increases, increasing the spreading in LCOH.

5.3. Permeability study

In this section, the permeability is studied in further detail. Where for the last section it was one of three variables in the plot, this time it is the only changed parameter to study the effect on the LCOH and recovery efficiency without influence from other parameters. In Figure 5.10, one can see the horizontal permeability plotted versus LCOH, as obtained from simulations shown in Table 3.9. In these simulations, the k_h/k_v ratio was kept constant at $10/1$. The point size indicates the HT-ATES variable OPEX to see how the permeability affects the total investment costs. This is not one of the main outputs this research focuses on, however, it is important to know since this is indicates the minimum total budget to start the project.

One can see that the lowest LCOH is not found either at highest or lowest permeabilities but rather somewhere in the middle, at $k_h = 50$ (and $k_v = 5$) Darcy. Under these circumstances, when increasing the aquifer permeability the LCOH increases. This can be explained by the lower recovery efficiencies; by buoyancy flow there are more heat losses to the top confining formation. Lower recovery efficiencies are also found at lower permeabilities. As already explained, this is a result of differences in viscosity along the well screen and throughout the aquifer and heat losses at the bottom of the aquifer. However, there is one other significant reason for the higher LCOH, this is the increased OPEX (pumping costs). At lower (horizontal) permeabilities, more energy is needed to inject and produce with the constant flow rate. This is also shown in Figure 5.10 when looking at the point sizes.

Figure 5.11 shows results from simulations provided in Table 3.10. A total of 3 different vertical and 4 different horizontal permeabilities have been used and plotted against recovery

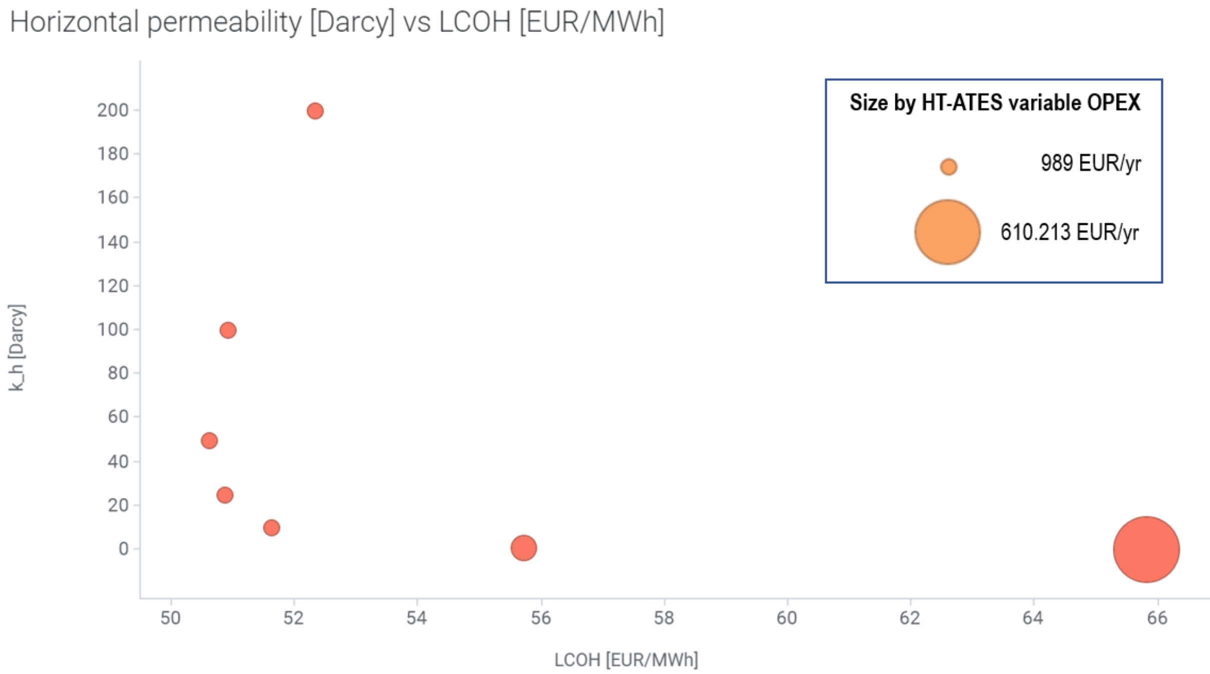

Figure 5.10: Horizontal permeability versus LCOH

efficiencies.

From Figure 5.11, one can see that in general at lower vertical permeabilities, the horizontal permeability has a higher impact on the recovery efficiency compared to higher vertical permeabilities. The line showing the $k_h = 1$ Darcy for all three values of k_v, shows lower recovery efficiencies. Then the line for $k_h = 10$ Darcy results in higher recovery efficiencies. But when comparing the largest horizontal permeabilities to each other, one can see that between $k_v = 1$ and $k_v = 5$, the two lines intersect. This indicates that for lower k_v values, the highest k_h is the preferred scenario, while for higher k_v values (5 and 10 Darcy), a k_h of 50 Darcy is preferred instead of 100 Darcy.

These different trends are a result of the interplay between buoyancy and viscous forces. Buoyancy flow is only dependent on the vertical permeability, whereas the fluid viscosity (related to fluid temperature) can influence fluid flow both in horizontal as vertical directions. When vertical permeabilities are low, buoyancy flow will not have a big impact on the fluid flow and therefore the shape of the stored heat. When vertical permeabilities are higher, the flow is determined both by buoyancy and viscous forces.

To come back to the $k_h = 50$ and 100 Darcy lines, there is an intersection visible between $k_v = 1$ and 5 Darcy. At the left side of the plot in Figure 5.11, vertical permeabilities are low and viscous forces are dominating. When the vertical permeability increases from 1 to 5 Darcy, the $k_h = 50$ Darcy scenario becomes more favourable when looking at the recovery efficiency. This can be explained by the fact that now the hot fluid can travel upwards more easily. The lower horizontal permeability ensures that when the hot fluid reaches the top of the aquifer, it is harder to flow to the sides along the boundary between the aquifer and confining top layer. This results in less heat losses to the clay formation on top. This is highlighted in Figure 5.12, where the difference in hot-water shapes is shown after 6 months of injection.

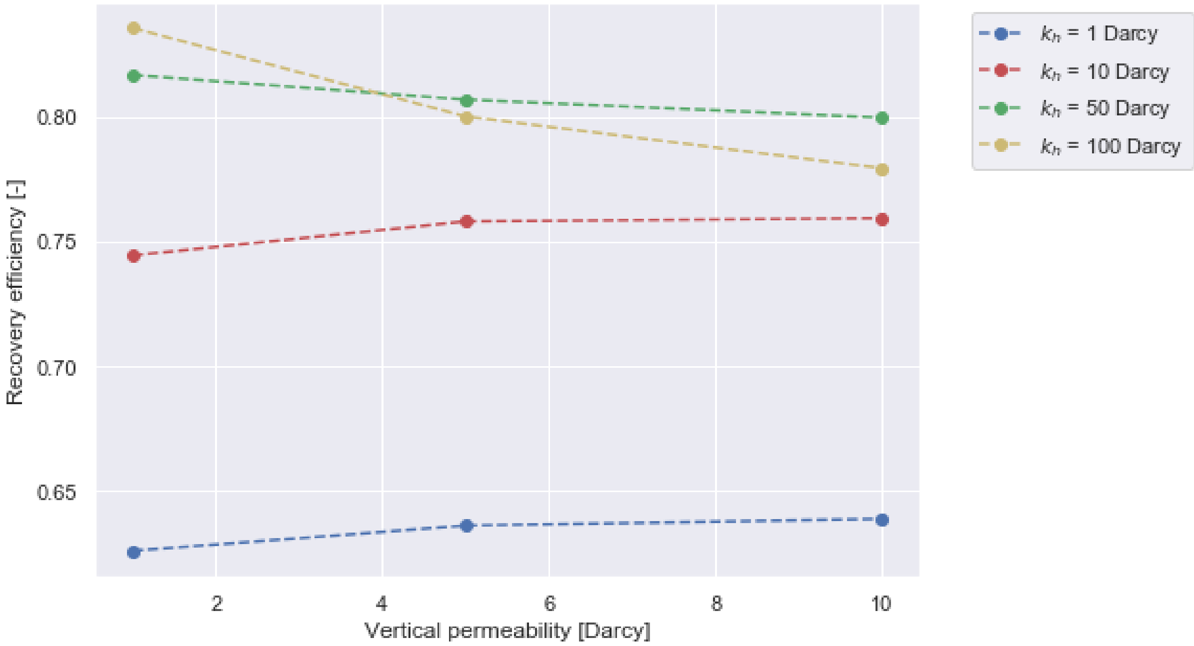

Figure 5.11: Recovery efficiencies for different values of horizontal and vertical permeabilities

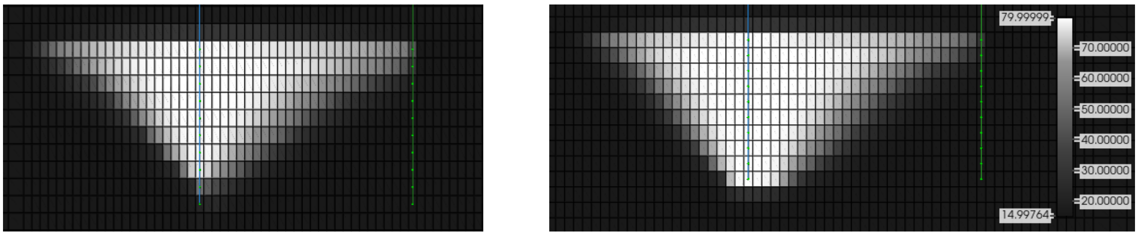

(a) $k_h = 100$ and $k_v = 5$ Darcy

(b) $k_h = 50$ and $k_v = 5$ Darcy

Figure 5.12: The difference in shape when k_v changes from 100 to 50 Darcy. Temperature profile after 6 months of hot-fluid injection.

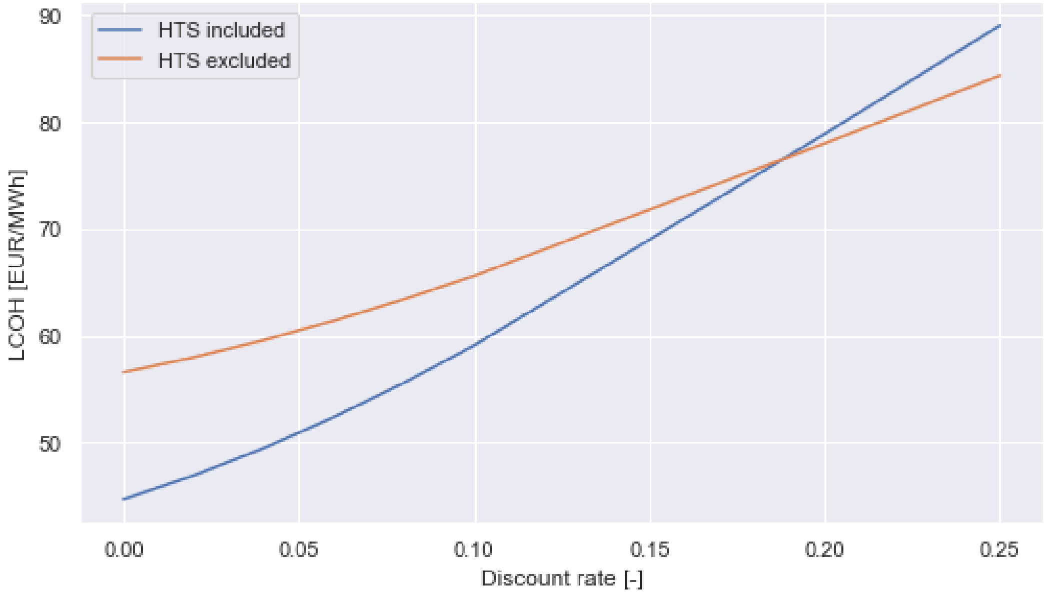

Figure 5.13: LCOH plotted versus the projects' discount rate (r). All other parameters are kept constant as provided in Tables 3.4 and 3.5.

5.4. Impact of economic parameters on the LCOH

In Figure 5.13, one can find the LCOH of the two scenarios (in- and excluding HT-ATES) at different project discount rates. One can see that for low discount rates the scenario where HT-ATES is included in the system of heat suppliers has a lower LCOH than the other scenario. At a discount rate of 18.3%, this switches to the scenario where only geothermal heat and the gas boiler provide heat to the network. However, this discount rate is not very representative since the discount rate as described in Bloemendal et al. (2020) is 0.055. But the trend is logical as well, this is mainly the result of the higher CAPEX and lower OPEX for the HT-ATES compared to the gas boiler. The impact of the discount rate increases the further into the lifetime of the project the costs are made. These costs include all operational expenses: fixed OPEX, variable OPEX and CO_2 taxes.

The LCOH is also plotted versus different gas prices, as can be seen in Figure 5.14. This Figure shows a linear relationship for both scenarios between the LCOH with a project lifetime of 30 years. However, the angle is different, because the gas price has a higher impact on the scenario where more gas is used. One can see that for gas prices below 21 €/MWh the scenario excluding HT-ATES is the better option. However, when the gas price exceeds this value, the scenario where HT-ATES is included in the network is the preferred option. This can be explained by the fact that gas price takes up a big part of the gas boiler OPEX. When gas prices are low, the difference between gas boiler and HT-ATES OPEX is small and then the low HT-ATES OPEX does not weight up against its large CAPEX. High gas prices, in this case average prices exceeding 21 €/MWh, result in a large boiler-HT-ATES OPEX difference and therefore it is worth to make the HT-ATES investment. Note that the gas price here is the average pas price over the full project lifetime.

In Figures 5.15, 5.16 and 5.17, the LCOH is plotted against the HT-ATES CAPEX, the CO_2 tax and the average electricity price, respectively. In Figure 5.15 one can find that even though the CAPEX does impact the absolute value of LCOH for the scenario where HT-ATES is included, for all realistic values the LCOH remains below the level of the scenario without high-

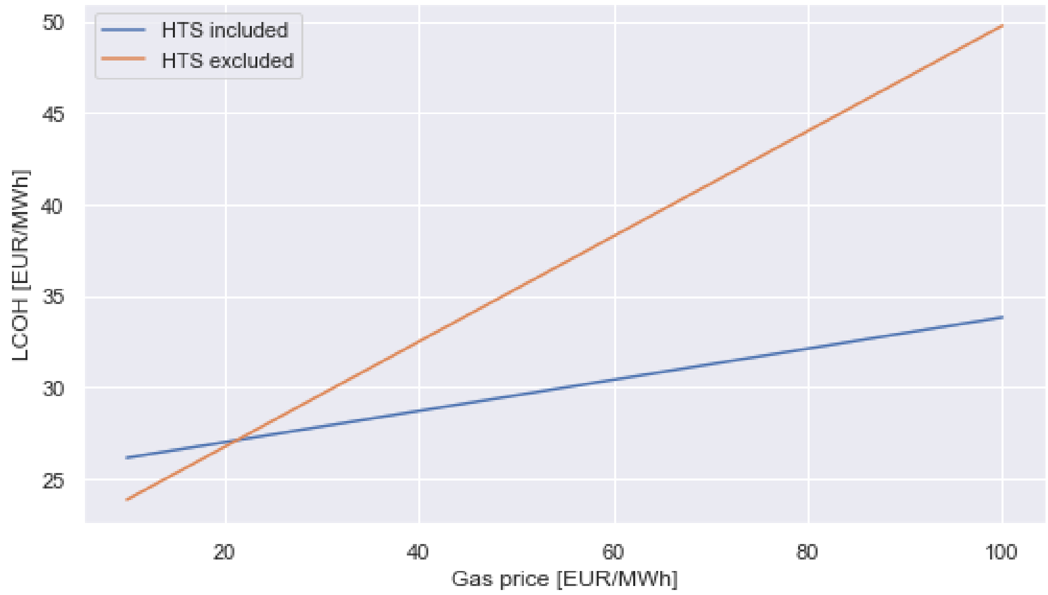

Figure 5.14: LCOH plotted versus the gas price. All other parameters are kept constant as provided in Tables 3.4 and 3.5.

temperature storage.

The CO_2 tax does have some impact on both scenarios. The scenario where HT-ATES is excluded is slightly steeper, since more CO_2 is emitted in that scenario. However, its impact is not decisive. The impact of the electricity price is also relatively small as obtained from Figure 5.17. This electricity is used to power the pumps for the high-temperature storage system.

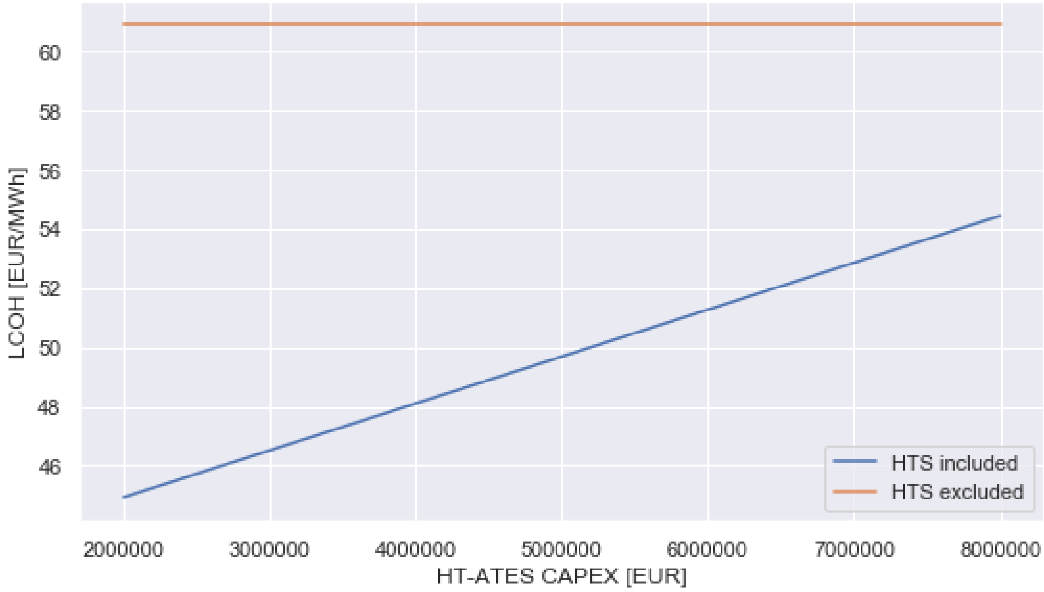

Figure 5.15: LCOH plotted versus the HT-ATES CAPEX. All other parameters are kept constant as provided in Tables 3.4 and 3.5.

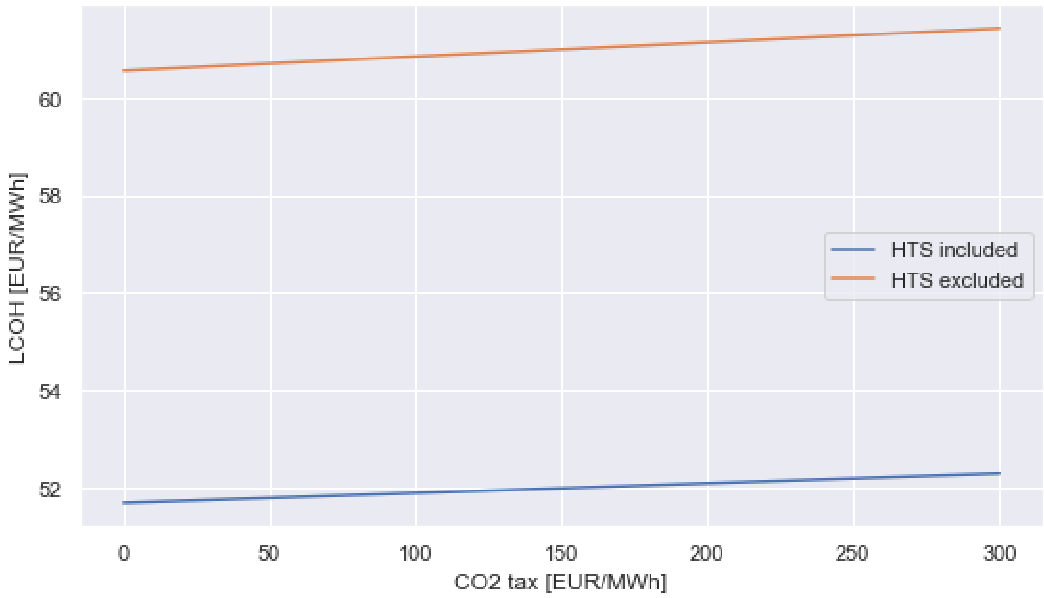

Figure 5.16: LCOH plotted versus the CO_2 tax. All other parameters are kept constant as provided in Tables 3.4 and 3.5.

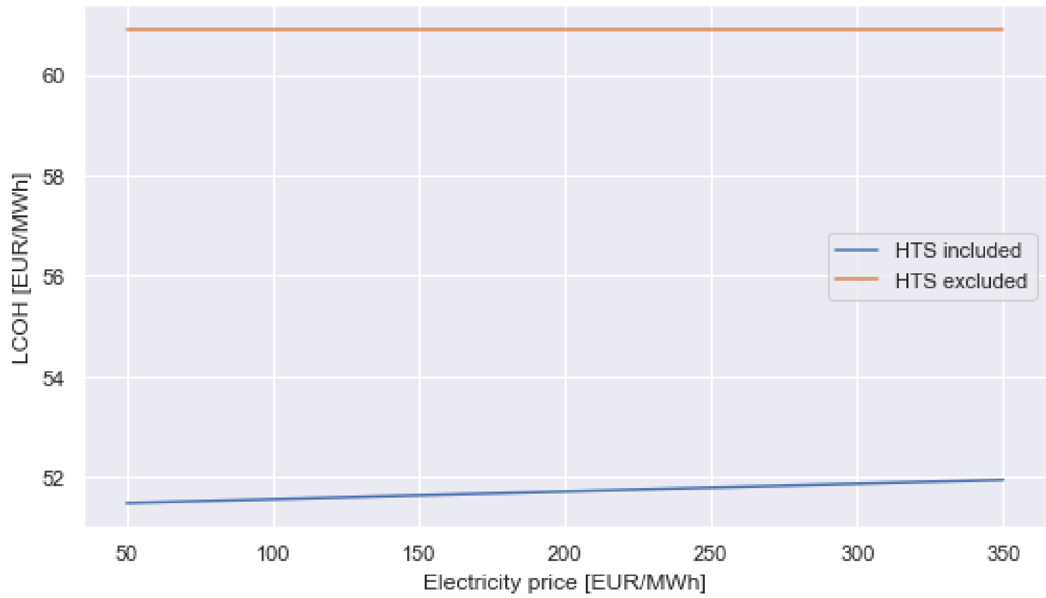

Figure 5.17: LCOH plotted versus the electricity price. All other parameters are kept constant as provided in Tables 3.4 and 3.5.

6 Discussion

6.1. Importance of the results

From the output of the HT-ATES performance simulator, one is able to study the impact every single parameter has on the subsurface fluid flow and final recovery efficiency. Some aquifer characteristics have a decisive impact whereas others only influence the outcome in a minor way. Most of the results are in line with the results of previous studies, such as fluid transport due to buoyancy flow and the fact that not all heat is retrieved during the hot-water production period. The buoyancy flow effect is an interplay between a lot of different factors, such as aquifer dimensions, aquifer permeability, ambient and injection temperature, storage volume and injection and production periods. One aspect that is not included in these simulations is the salt content of the water and the biochemistry as a result of temperature differences in the aquifer. Also, it is assumed no heat losses are present during water transport between the surface and aquifer.

From the results, it is obtained that the amount of buoyancy flow present in the aquifer determines the main heat loss processes. When the stored heat is transported to the top of the aquifer at a fast rate, a lot of heat is lost via conduction to the top confining layer resulting in a low recovery efficiency. However, in that same scenario less heat is lost via conduction to the bottom of the aquifer. When having a closer look into the aquifer permeability, this results in interesting observations.

To recall the results of the permeability analysis, there is an optimum for the permeabilities to obtain the best efficiency ($k_h = 100$ and $k_v = 1$ Darcy). Higher permeability values result in more buoyancy flow and therefore more heat losses to the top confining formation. Lower permeabilities increase heat losses to the bottom of the aquifer. The interplay between viscous and buoyancy forces impact the fluid flow in the reservoir. The role of fluid viscosity as a function of temperature is highlighted in Table 5.1, where one is able to see the difference in flow rates from different aquifer intervals at different aquifer permeabilities. There it is explained that more buoyancy flow results in larger temperature differences between the different sections along the well and therefore results in larger fluid viscosity differences and flow rates. The higher the temperature in a specific section compared to the other sections, the more fluid flows in or out of the well.

One of the assumptions in the CMG GEM model is a homogeneous permeability distribution in the aquifer. In two scenarios some heterogeneity in the reservoir is simulated using either one or two 1m-thick clay layers within the sand formation. However, it is very likely that also on a smaller scale some form of heterogeneity is present, which is not included in these simulations. This uncertainty especially holds for the subsurface parameters like porosity, permeability, rock specific heat capacity and thermal conductivity. Two of the decisive parameters are storage volume and temperature difference between the two wells. These variables in the modelling tool are associated with less uncertainties, since this can precisely be operated from the surface.

The degree of uncertainty associated with particular parameters includes not only the technical factors, but also the economic variables. The CAPEX of the specific heat suppliers can be predicted accurately, especially for the gas boilers but also for the geothermal doublet. However, the average gas price for the upcoming years is extremely hard, if not impossible, to predict. So, although the gas price does have an impact on the HT-ATES economic feasibility, it is hard to draw the conclusions at this point.

6.2. Added value in relation to previous studies

In the Introduction, an overview is given on the current state-of-the-art of HT-ATES. Some things already discussed there are also found in the simulation results from this research. Buoyancy flow, for example, is something that is studied in detail in previous studies and proved to have an effect on the flow within the aquifer in the simulations from this research as well. The fact that the recovery efficiency is lower in the first couple of cycles is also not a surprise, this was already mentioned in other literature as well and the results of this project confirm this. Another important result is the total CO_2 emissions savings, which also align with a previous study on HT-ATES implementation at the TU Delft Campus, performed by Bloemendal et al. (2020). From both studies, a CO_2 emission reduction of 31% is predicted.

However, apart from confirming the results of previous studies performed on HT-ATES, the goal is to add knowledge to the current SOTA of high-temperature storage. One of the goals is to not only investigate technical feasibility but also look into the business case of HT-ATES implementation and to identify the key factors that affect the economic feasibility. From the obtained results, one can say that the key parameters affecting HT-ATES economic feasibility are storage volume, aquifer permeability, temperature differences between hot and warm well, discount rate and average gas price. These key parameters are retrieved not only by assessing the HT-ATES feasibility on its own, but looking into the full heat demand and supply system.

The HT-ATES technical performance simulations are performed in CMG GEM software, something that is not done before. The proof that this report provides, that simulating HT-ATES in this software is possible, can bring the traditional oil and gas sector that makes use of this software and the new technology closer together. This could potentially lead to more projects in the future, kicking off this promising technique in practice.

The economic feasibility tool created in Python is build up in a way that the economic assessment can be performed for different types of systems. The economic assessment is created in such a way that when the technical performance (output from CMG GEM) is present, one can easily obtain the key economic outputs such as LCOH and CO_2 emissions.

6.3. Consequences

In the research question, the importance of economic feasibility for HT-ATES implementation in current heat networks is already highlighted. A lot of previous work focused mainly on technical aspects rather than also looking at the finances. When looking at the bigger picture, all research performed on this technique to enable more green energy in our heating systems is meant to contribute to more real-life projects in the near future. These projects will only start when a strong foundation is build that indicates an attractive business case.

This research adds to the foundation in a way that the results show that the LCOH of the situation at the TU Delft Campus decreases when HT-ATES is implemented compared to the scenario when only the geothermal doublet and gas boilers provide heat. This helps to not only support the start of the implementation in Delft, but hopefully also at other locations. The decisive characteristics that are found in this research can help companies or institutions that have interest in starting a HT-ATES project, to design the storage system in an optimal way.

7 Conclusions and Recommendations

7.1. Conclusions

The first research question focuses on how to model all relevant parameters to obtain a business case for HT-ATES implementation in heat networks. This research introduces a method that first models the technical process of subsurface heat storage in a 3D equation-of-state numerical simulator, where both subsurface and operational input parameters are required. This simulator shows detailed heat propagation profiles over time as well as pressure profiles and provides all relevant well production data: volumetric flow rates, well-head temperatures and bottom-hole pressures.

Simulation outputs from this HT-ATES technical performance simulator are used in an assessment tool, that also requires operational and economic input data. The assessment tool then provides the key data to assess HT-ATES feasibility in the heat network; a costs overview, the project LCOH, recovery efficiency, load factors and total CO_2 emissions.

These tools are then used to assess the economic feasibility of HT-ATES implementation at the TU Delft Campus. A comparison is made between the heat network where only a geothermal doublet and gas boilers provide heat and a network where high-temperature storage is included as well. Results show that under the conditions provided for HT-ATES implementation at the TU Delft Campus, the network where HT-ATES is included is the economic scenario, only if the project lifetime is longer than 13.6 years. For a project lifetime of 30 years, the LCOH when HT-ATES is included is 52 €/MWh compared to 61 €/MWh when only heat is provided by the geothermal doublet and gas boilers. Total CO_2 savings when using high-temperature storage are 31% compared to the other scenario.

The second research question states 'What are the decisive characteristics for HT-ATES economic feasibility?'. In order to answer this question, the previously mentioned tools are used to model all relevant parameters in a sensitivity analysis to study the impact of these parameters on important outputs: recovery efficiency, LCOH and CO_2 emissions. There it is found that the aquifer permeability has an impact on fluid flow: higher permeabilities increase buoyancy flow as a result of water density differences. The extent of buoyancy flow influences the shape of the stored hot water in the reservoir and therefore the main heat loss processes. High vertical permeabilities result in hot-water accumulation near the top of the aquifer and therefore more heat losses via conduction to the top confining clay formation. At lower permeabilities, the heat loss to confining layers is more evenly distributed between top and bottom confining layers, because the hot water is more evenly distributed along the well screen length.

The shape of the stored hot water in the aquifer also affects fluid viscosity distributions. The buoyancy flow effect results in larger temperature and therefore fluid viscosity differences along the well. Volumetric flow rates from well screen intervals with lower fluid viscosities are higher compared to intervals at lower temperatures and therefore higher viscosity. The interplay between buoyancy and viscous forces results in an optimal permeability of $k_h = 50$ and $k_v = 5$ Darcy under the circumstances provided, which results in a LCOH of 51 €/MWh.

Two operational parameters that showed to be decisive characteristics for HT-ATES economic feasibility are storage volume and the temperature difference between the wells. Increasing the storage volume and wells ΔT both increases the power output and improves recovery efficiencies. This lowers the projects' LCOH.

The economic parameters discount rate and gas price also impact the LCOH and affect the competitiveness of HT-ATES in the heat network. Heat-storage implementation is only the economic option when the discount rate is below 18% and when the average gas price during the projects lifetime exceeds 21 €/MWh and all variables remain as stated for the case at the TU Delft Campus.

7.2. Recommendations

All performed simulations in this research were focused on the conditions at the TU Delft Campus with an HT-ATES system in the Maassluis formation. However, it is important to see what results can be obtained when applying these technical and economic tools to another location with different subsurface conditions, another geothermal base load and heat demand. This implies not changing only very few parameters at a time, which was in the sensitivity analysis in this research, but adjusting both the subsurface model and the operational parameters significantly. A good test for the tools discussed in this report would be to apply them to another project to assess the feasibility.

The permeability was studied in detail in this report. However, the prediction is that reservoir geometries also could affect the optimal permeability values. A thicker aquifer with a constant storage volume throughout these scenarios allows for more fluid transport due to buoyancy forces than a very thin aquifer where the shape of the stored hot water is much flatter. This must be studied into further detail to reveal the optimal permeabilities at different reservoir geometries.

Although some simulations were performed that included some reservoir heterogeneity, this should still be studied in more detail. The layered-cake approach could be refined to include more vertical heterogeneities. Since the model is build using a Cartesian grid, also some heterogeneity in the horizontal directions could be included.

For all scenarios, the assumption was made that there are no heat losses during transport of the water from and to the surface and aquifer. However, depending on multiple parameters such as the volumetric flow rate and aquifer depth, there will be some heat losses around the wells. The significance of these heat losses could be modelled to see whether or not this process should be taken into account.

Implementing a high-temperature storage system results in large temperature differences in the aquifer. This could affect the biochemical composition of the water which can result in problems around the wells such as well clogging. In some areas in The Netherlands, drinking water is also extracted from the same aquifers as the potential HT-ATES aquifers and therefore there it should be looked into the biochemics of the fluids in more detail to ensure the water quality is maintained.

References

Baker, R., & Jensen, J. (2015). Conventional core analysis - rock properties. *Practical Reservoir Engineering and Characterization*, *1*(1), 1–27.

Birdsell, D., Adams, B., & Saar, M. (2021). Minimum transmissivity and optimal well spacing and flow rate for high-temperature aquifer thermal energy storage. *Applied Energy*, *1*(289), 1–14. doi: https://doi.org/10.1016/j.apenergy.2021.116658

Blanco, H., & Faaij, A. (2018). A review at the role of storage in energy systems with a focus on power to gas and long-term storage. *Renewable and Sustainable Energy Reviews*, *81*.

Bloemendal, M. (2021). *Ates well design.* Retrieved 17-08-2022, from https://brightspace.tudelft.nl/d2l/le/content/288823/viewContent/2062711/View

Bloemendal, M., Vardon, P., Medema, A., Snelleman, S., Marif, K., Beernink, S., … Van Oort, T. (2020). Ht-ates at the tu delft campus. *Feasibility study*, *1*(1), 1–77.

Daniilidis, A., Mindel, J., De Oliveira Filho, F., & Guglielmetti, L. (2022). Techno-economic assessment and operational co2 emissions of high- temperature aquifer thermal energy storage (ht-ates) using demand-driven and subsurface-constrained dimensioning. *Energy*, *249*(123682), 1–17. doi: https://doi.org/10.1016/j.energy.2022.123682

Dinkelman, D. (2019). Optimization of technical and economic efficiency of ht-ates combined with geothermal energy. *Master's thesis*, *1*(1), 1–97.

Driesner, T. (2021). Heatstore - final report on tools and workflows for simulating subsurface dynamics of different types of high temperature underground thermal energy storage. *Geothermica*, *1*(1), 1–355.

Drijver, B., Van Aarssen, M., & De Zwart, B. (2012). High-temperature aquifer thermal energy storage (ht-ates): sustainable and multi-usable. *Innostock*, *1*(1), 1–10.

DUEC. (2022). *Warmtepompen besparen voor co_2 uitstoot ten opzichte van gasverwarming.* Retrieved 13-05-2022, from https://www.duec.nl/warmtepompen-besparen-veel-co2-uitstoot-ten-opzichte-van-gasverwarming/#:~:text=Bij%20verbranding%20van%20aardgas%20komt,uitgestoten%20(1800%2F9).

EBN. (2022). *Infographic 2022.* Retrieved 25-09-2022, from https://www.energieinnederland.nl/feiten-en-cijfers/infographic/

EEX. (2022). *Spot market data.* Retrieved 16-06-2022, from https://www.powernext.com/spot-market-data

EMI. (2022). *Marktinformatie elektra.* Retrieved 16-04-2022, from https://www.energiemarktinformatie.nl/beurzen/elektra/

Fleuchaus, P., Godschalk, B., Stober, I., & Blum, P. (2018). Worldwide application of aquifer thermal energy storage - a review. *Renewable and Sustainable Energy Reviews*, *94*(1), 861–876.

Harris, C. R., Millman, K. J., van der Walt, S. J., Gommers, R., Virtanen, P., Cournapeau, D., … Oliphant, T. E. (2020, September). Array programming with NumPy. *Nature*, *585*(7825), 357–362. Retrieved from https://doi.org/10.1038/s41586-020-2649-2 doi: 10.1038/s41586-020-2649-2

Hartog, N., Bloemendal, M., Slingerland, E., & Van Wijk, A. (2016). Duurzame warmte gaat ondergronds. *KWR*, *1*(1), 1–7.

Hunter, J. D. (2007). Matplotlib: A 2d graphics environment. *Computing in Science & Engineering*, *9*(3), 90–95. doi: 10.1109/MCSE.2007.55

LTD., C. M. G. (2022). *Gem user guide 2020.11.*

Marif, K. (2019). Counteraction of buoyancy flow in high temperature aquifer thermal energy storage systems by applying multiple partially penetrating wells. *MSc Thesis*, *1*(1), 1–116.

Matek, B., & Gawell, K. (2015). The benefits of baseload renewables: A misunderstood energy technology. *The electricity journal*, *28*(2), 101–112. doi: https://doi.org/10.1016/j.tej.2015.02.001

MEA. (2018). Natural resources and geothermal energy in the netherlands in 2017. *Annual review*, *1*(1), 1–139.

Numbere, D., Brigham, W., & Standing, M. (1977). Correlations for physical properties of petroleum reservoir brines. *Stanford University Petroleum Research Institute*, *1*(1), 1–21.

Oerlemans, P. (2018). Modelling heat transport in a high temperature ates system. *MSc Thesis*, *1*(1), 1–53.

of Gaza, T. I. U. (2011). *Special topics in water and environment.* Retrieved 24-08-2022, from `http://site.iugaza.edu.ps/ymogheir/files/2010/02/Lecture-11.pdf`

pandas development team, T. (2020, February). *pandas-dev/pandas: Pandas.* Zenodo. Retrieved from `https://doi.org/10.5281/zenodo.3509134` doi: 10.5281/zenodo.3509134

PBL. (2022). *Eindadvies basisbedragen sde++ 2022.* Retrieved 20-07-2022, from `https://www.pbl.nl/publicaties/eindadvies-basisbedragen-sde-2022`

PWC. (2022). *A national co2 tax to reduce annual industrial emissions with 14.3 megatonnes by 2030.* Retrieved 28-04-2022, from `https://www.pwc.nl/en/topics/sustainability/green-deal-monitor/green-deal-monitor-4.html#:~:text=To%20ensure%20achieving%20this%20goal,Economic%20Affairs%20and%20Climate%20Policy.`

Rowe, A., & Chou, J. (1970). Pressure - volume - temperature - concentration relation of aqueous nacl solutions. *Chemical Engineering Data*, *1*(1), 61–66.

Schout, G., Drijver, B., Gutierrez-Neri, M., & Schotting, R. (2014). Analysis of recovery efficiency in high-temperature aquifer thermal energy storage: a rayleigh-based method. *Hydrology Journal*, *22*(1), 281–291. doi: DOI10.1007/s10040-013-1050-8

Ssegawaa, J., & Muzindab, M. (2021). Feasibility assessment framework (faf): A systematic and objective approach for assessing the viability of a project. *Procedia*, *181*(1), 377–385.

TNO. (2020). Duurzaamheid van geothermie in warmtenetten. *TNO whitepaper*, *1*(1), 1–36.

TNO. (2022). *Subsurface models; regis ii v2.2.* Retrieved 14-04-2022, from `https://www.dinoloket.nl/en/subsurface-models`

Van Gessel, S., Huijskes, T., Juez-Larré, J., & Dalman, R. (2021). Ondergrondse energieopslag in nederland 2030 – 2050: Technische evaluatie van vraag en aanbod. *TNO Rapport 2021*, *1*(1), 1–115.

Van Lopik, J., Hartog, N., & Zaadnoordijk, W. (2016). The use of salinity contrast for density difference compensation to improve the thermal recovery efficiency in high-temperature aquifer thermal energy storage systems. *Hydrogeol J*, *1*(1), 1–17. doi: DOI10.1007/s10040-016-1366-2

Vinsome, P., & Westerveld, J. (1980). A simple method for predicting cap and base rock heat losses in thermal reservoir simulators. *JCPT*, *19*(1), 87–90.

WarmingUp. (2021). *Inpassing van hto in warmtenetten.* Retrieved 08-01-2022, from https://www.warmingup.info/documenten/project-5b2-inpassing-hto-window-consortium-meeting-2dec2021.pdf

Waskom, M. L. (2021). seaborn: statistical data visualization. *Journal of Open Source Software*, *6*(60), 3021. Retrieved from https://doi.org/10.21105/joss.03021 doi: 10.21105/joss.03021

Zwamborn, M., Kleinlugtenbelt, R., De Man, G., Schaaf, J., & Mars, J. (2020). Notitie vergelijking en selectie locaties. *Window*, *1*(1), 1–37.

Appendices

Appendix I: Study on storage volume

These plots are created to further highlight the relationship between storage volumes, recovery efficiencies and the LCOH. Using the outputs from the simulations using inputs from Table 3.8, the plot in Figures 1 and 2 are created. The storage volume is plotted against recovery efficiency in Figure 1 and versus LCOH in Figure 2, where the colors indicate the total HT-ATES annual energy output. A trend is also indicated.

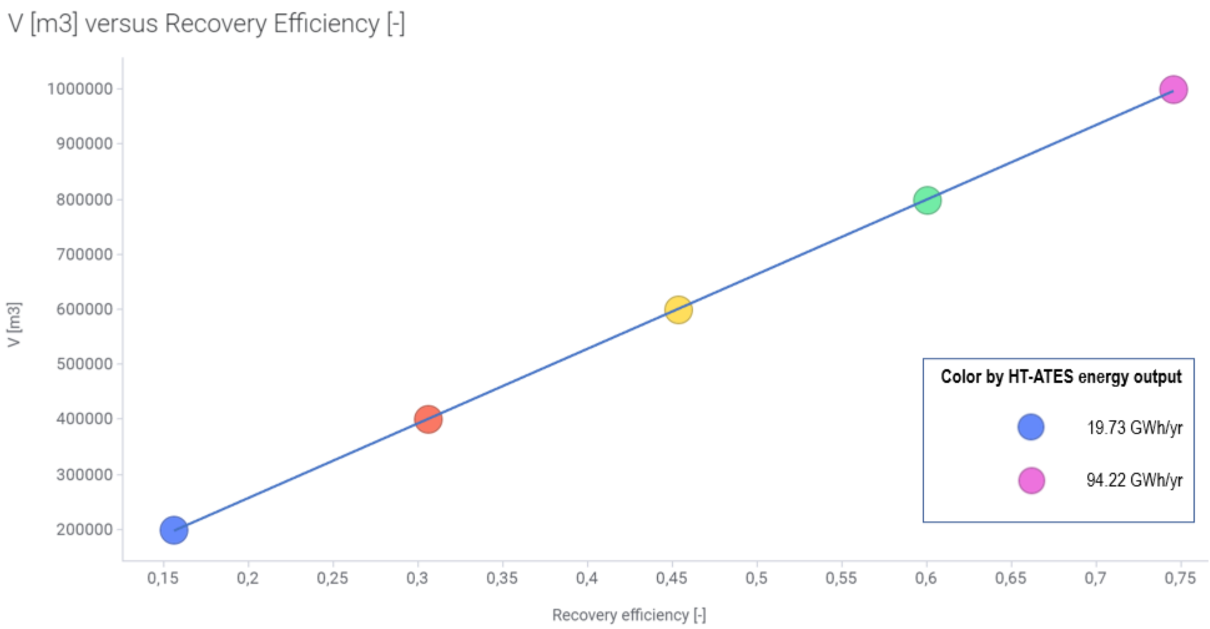

Figure 1: Storage volume versus recovery efficiency

In Figure 1, one can see a clear linear relationship between the storage volume and the recovery efficiency. The trend shows that larger storage volumes result in higher recovery efficiencies. The color of the points imply the total annual HT-ATES energy outputs, which is related to these other two parameters as well. The larger the volume, the higher the energy output simply because more heat is stored.

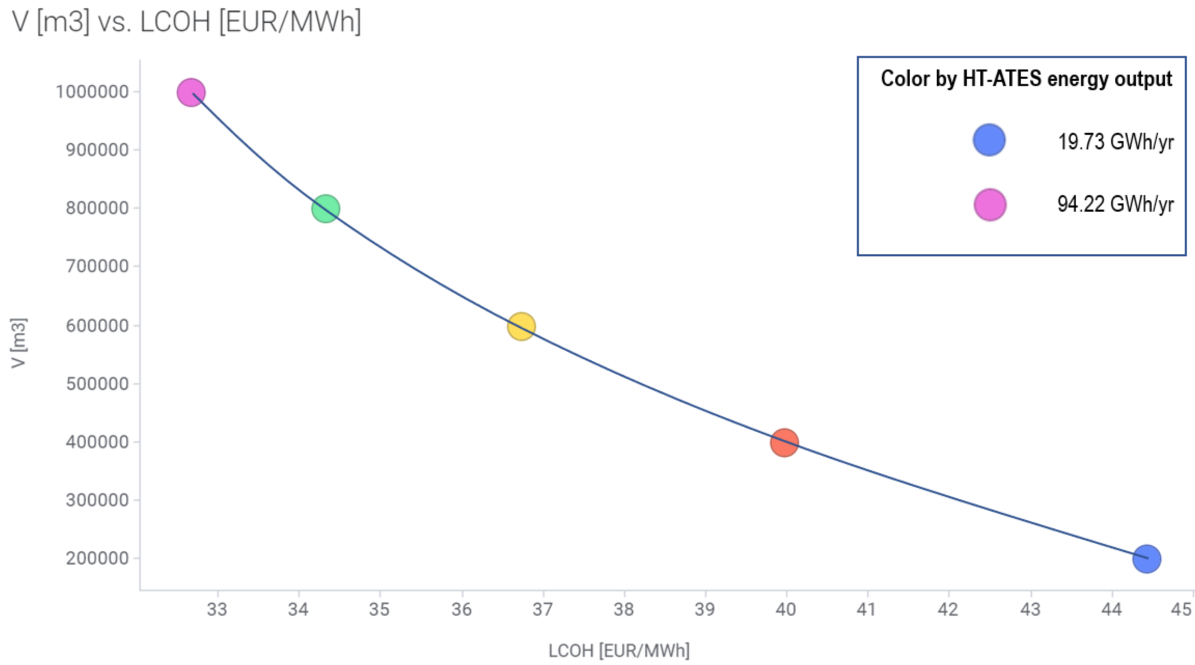

Figure 2: Storage volume versus LCOH

The same volumes have also been plotted against the LCOH, as is shown in Figure 2. The colors indicate the total energy output from the HT-ATES. In this graph, there still is a clear trend, however, this time it is not linear. The trend confirms the statements about storage volumes for Figure 5.9, that higher storage volumes results in a lower LCOH. The trendline also shows that when the storage volume keeps increasing, the decrease in LCOH slows down. When looking at the whole heating network, this is due to the relationship with the heat demand. The more energy supplied by the HT-ATES, the more gaps there are in the profile where there is less or no demand for the heat storage system. So then relatively a smaller part of the heat can be used effectively.

Appendix II: Base case temperature profiles

I-K cross sections of the temperature profiles over time. The cross-sections after 3 and 3.5 cycles can be found in Chapter 4.

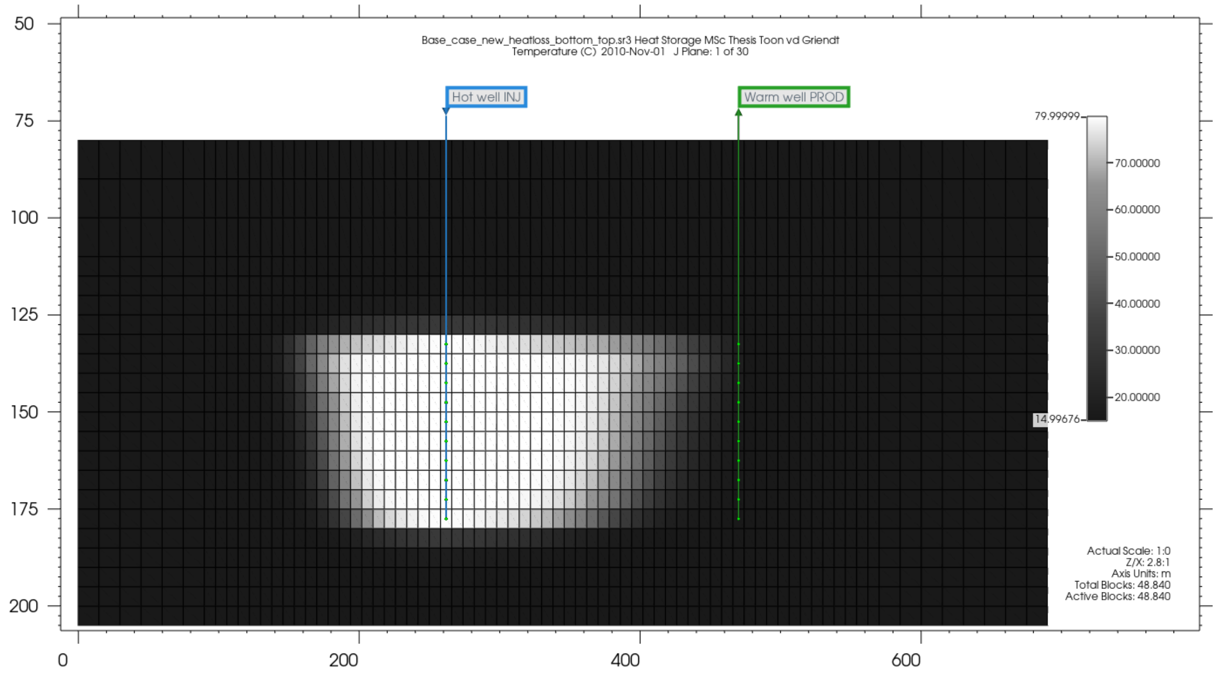

Figure 3: Vertical cross-section of the temperature profile after 0.5 cycle

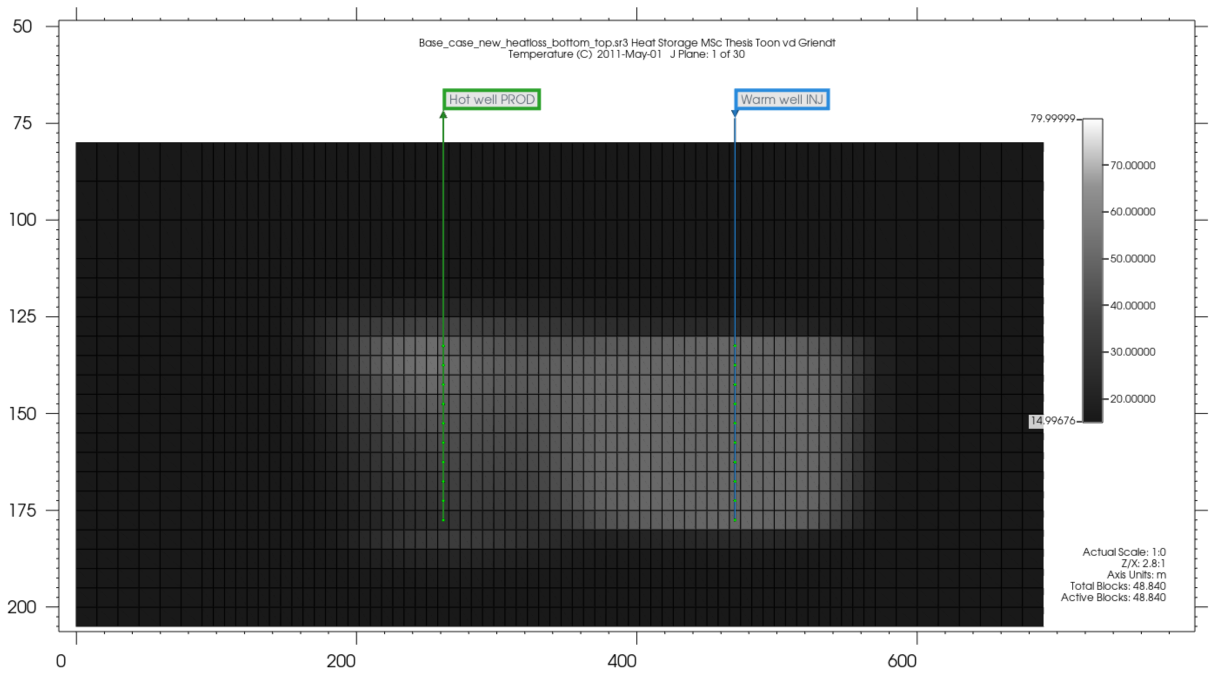

Figure 4: Vertical cross-section of the temperature profile after 1 cycle

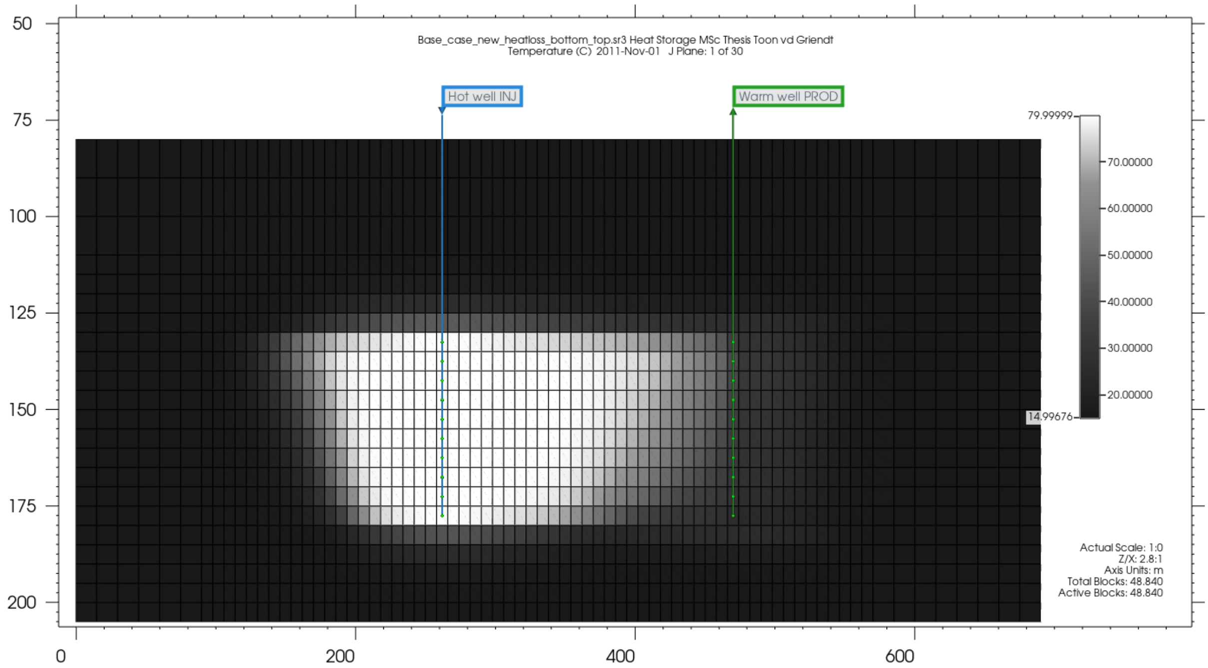

Figure 5: Vertical cross-section of the temperature profile after 1.5 cycles

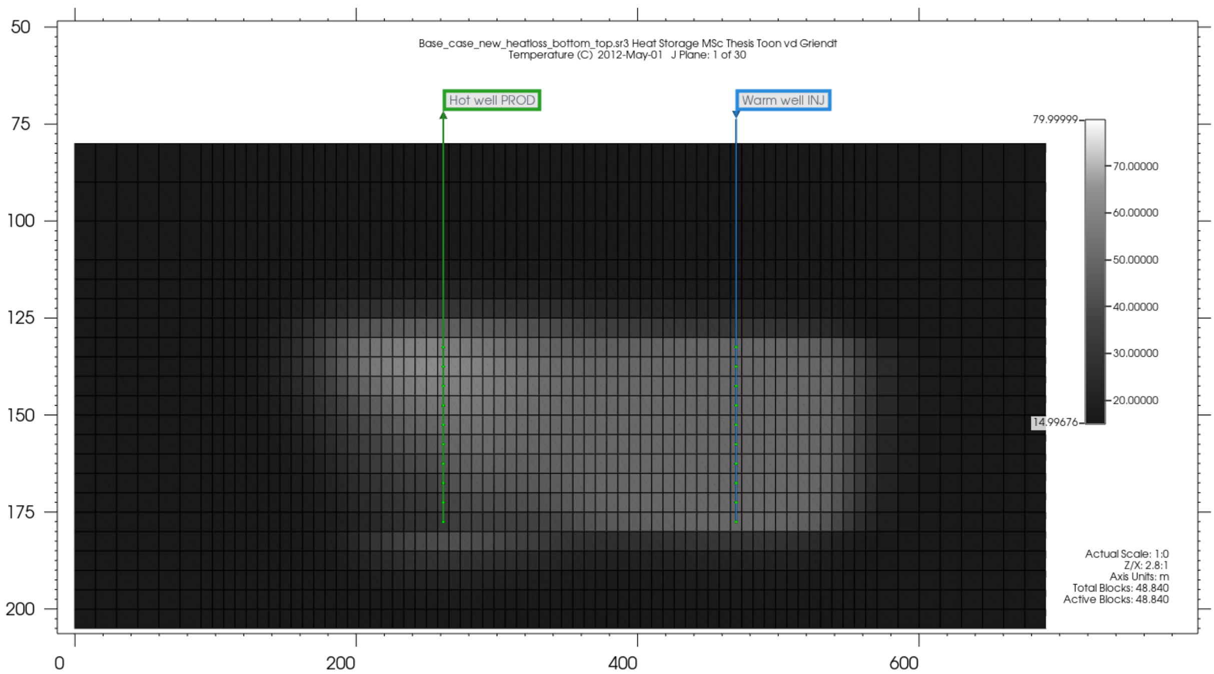

Figure 6: Vertical cross-section of the temperature profile after 2 cycles

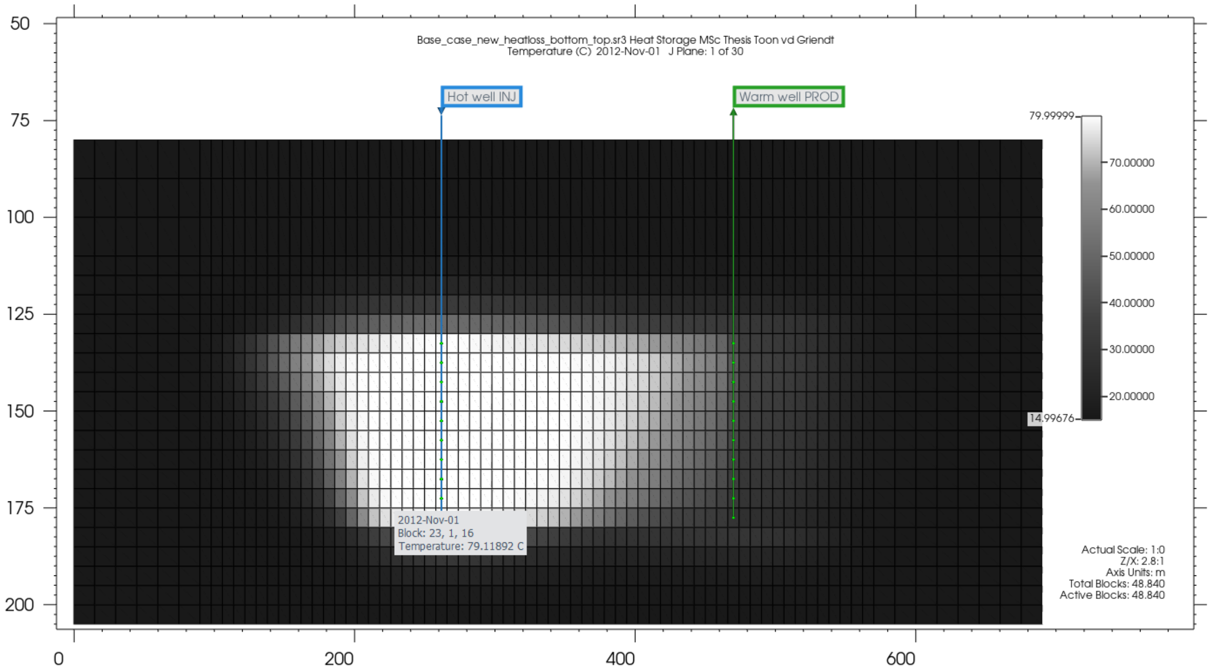

Figure 7: Vertical cross-section of the temperature profile after 2.5 cycles

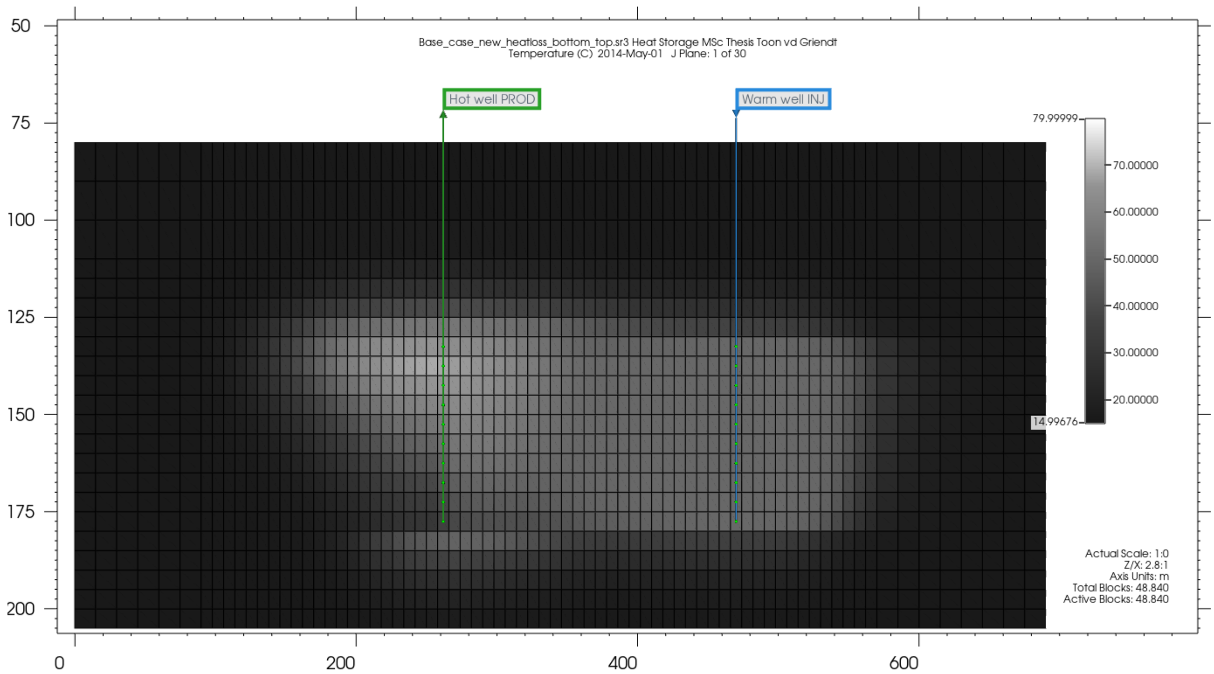

Figure 8: Vertical cross-section of the temperature profile after 4 cycle

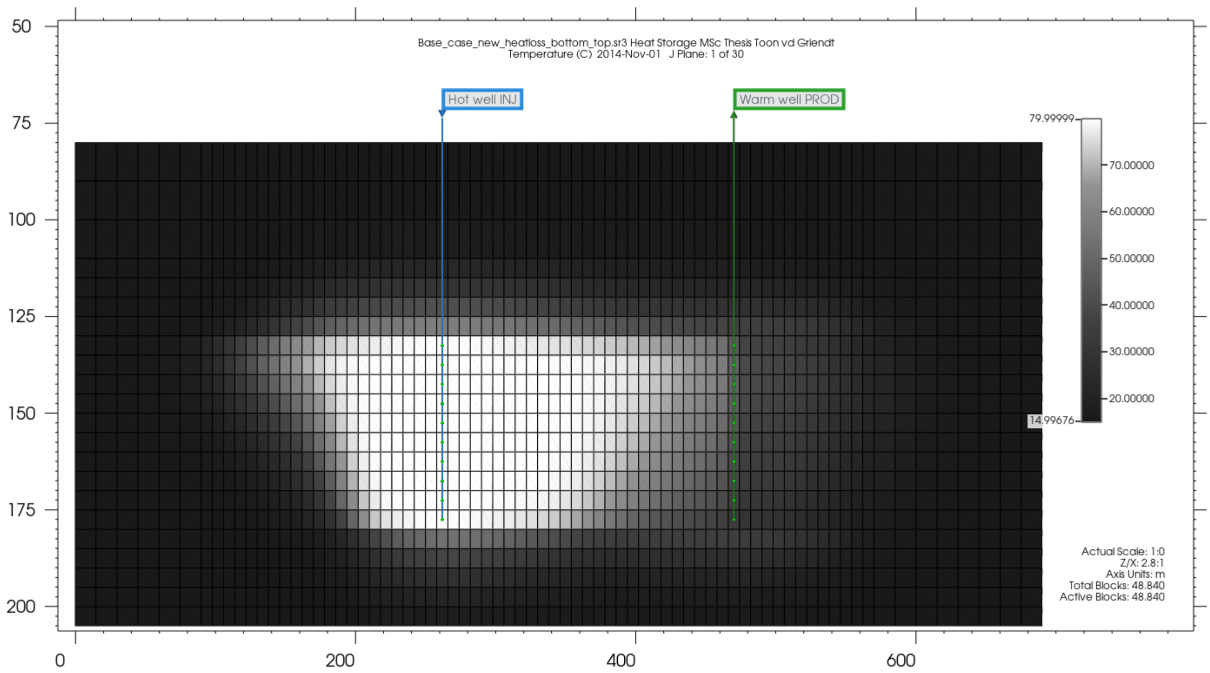

Figure 9: Vertical cross-section of the temperature profile after 4.5 cycles

Appendix III: Temperature profiles of the scenarios from parameter study

I-K cross-sections of the temperature profiles after exactly 3.5 cycles, just after hot-water injection of the fourth cycle. The cross-sections of scenarios 8, 9, 14, 15, 18 and 19 can be found in Chapter 5.

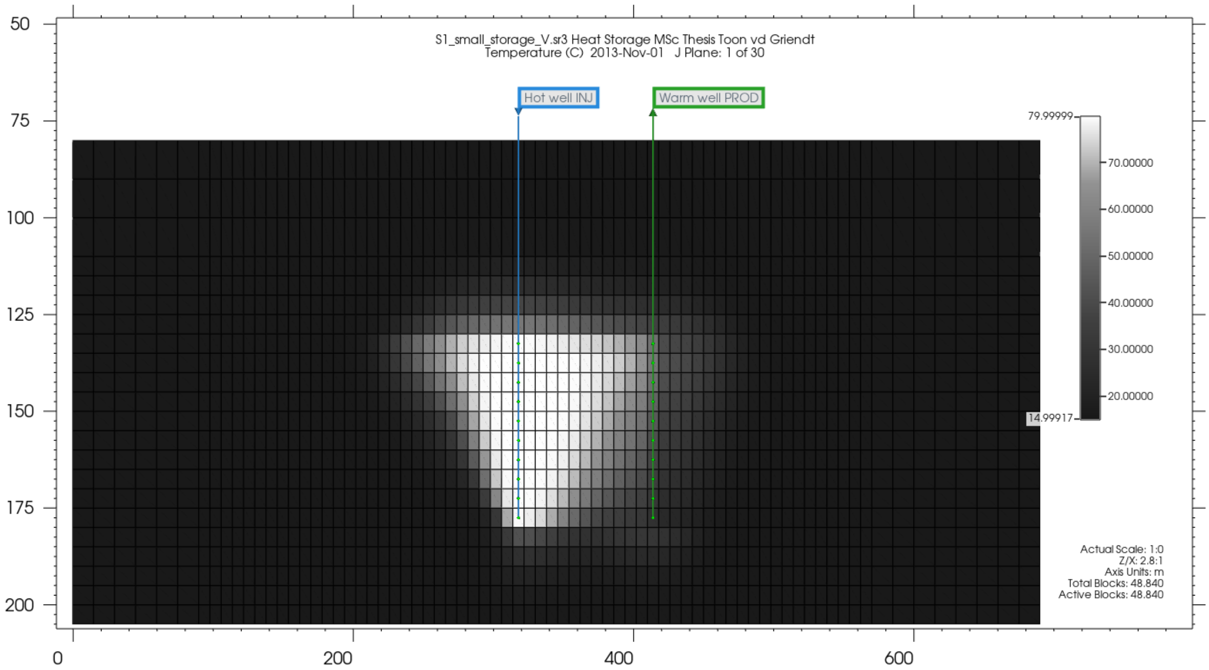

Figure 10: Vertical cross-section of the temperature profile after 3.5 cycles for scenario 1; small storage volume

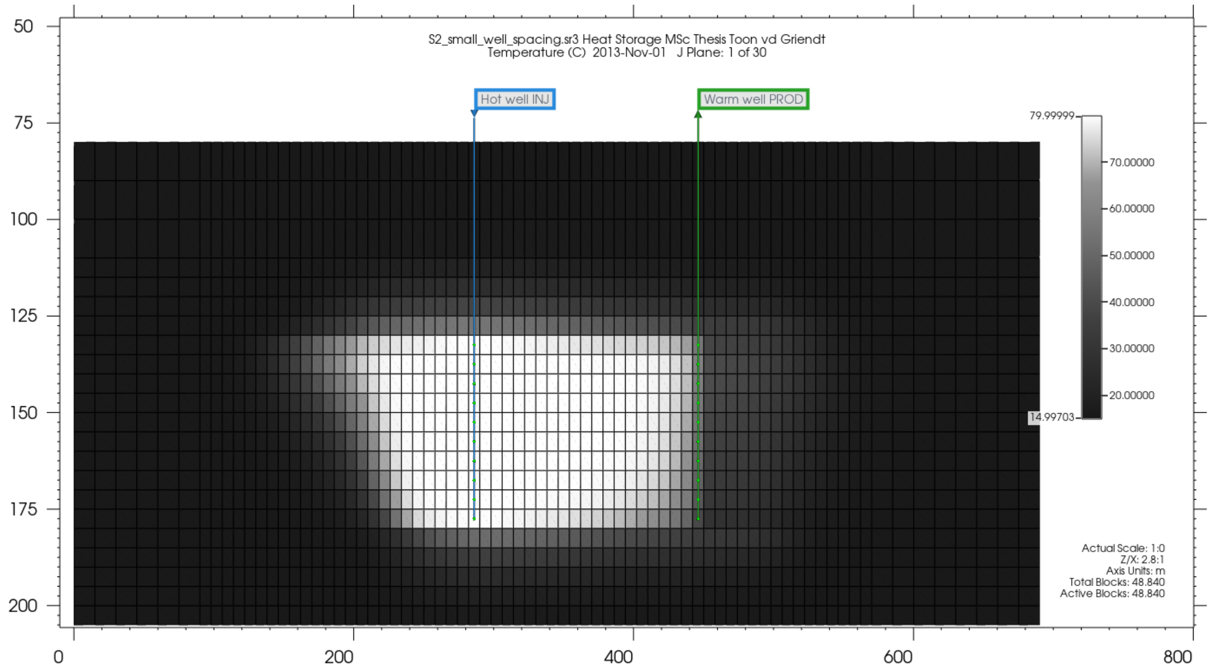

Figure 11: Vertical cross-section of the temperature profile after 3.5 cycles for scenario 2; small well spacing

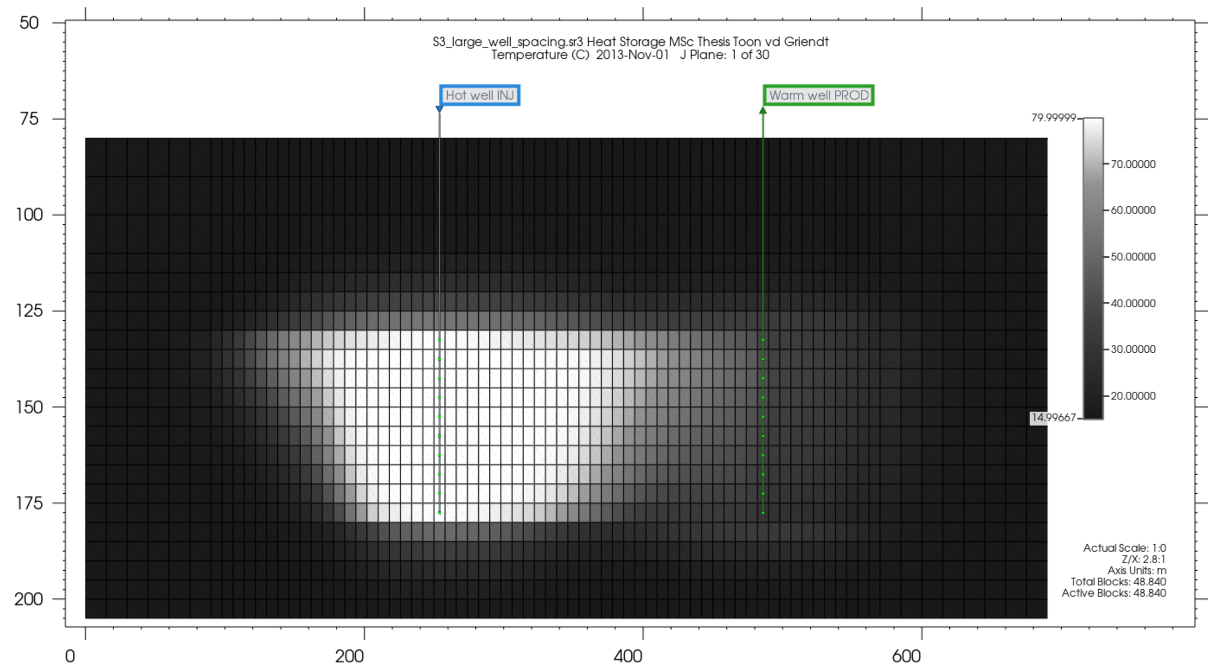

Figure 12: Vertical cross-section of the temperature profile after 3.5 cycles for scenario 3; large well spacing

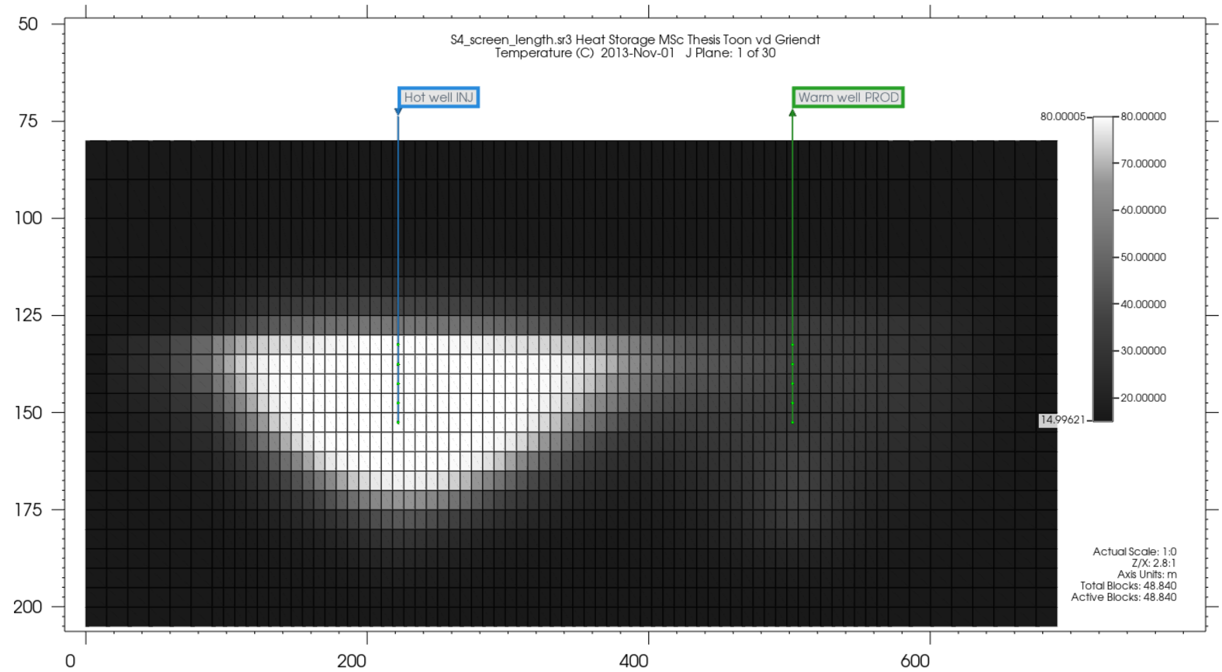

Figure 13: Vertical cross-section of the temperature profile after 3.5 cycles for scenario 4; screen length only in upper half

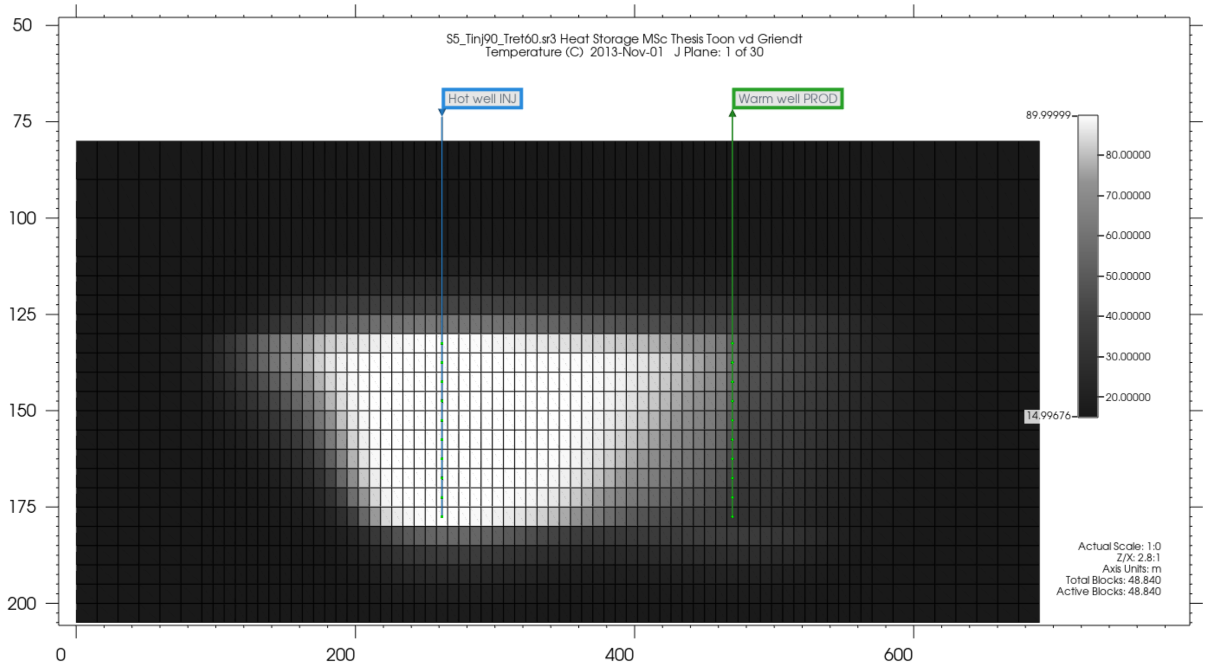

Figure 14: Vertical cross-section of the temperature profile after 3.5 cycles for scenario 5; higher temperatures in the wells

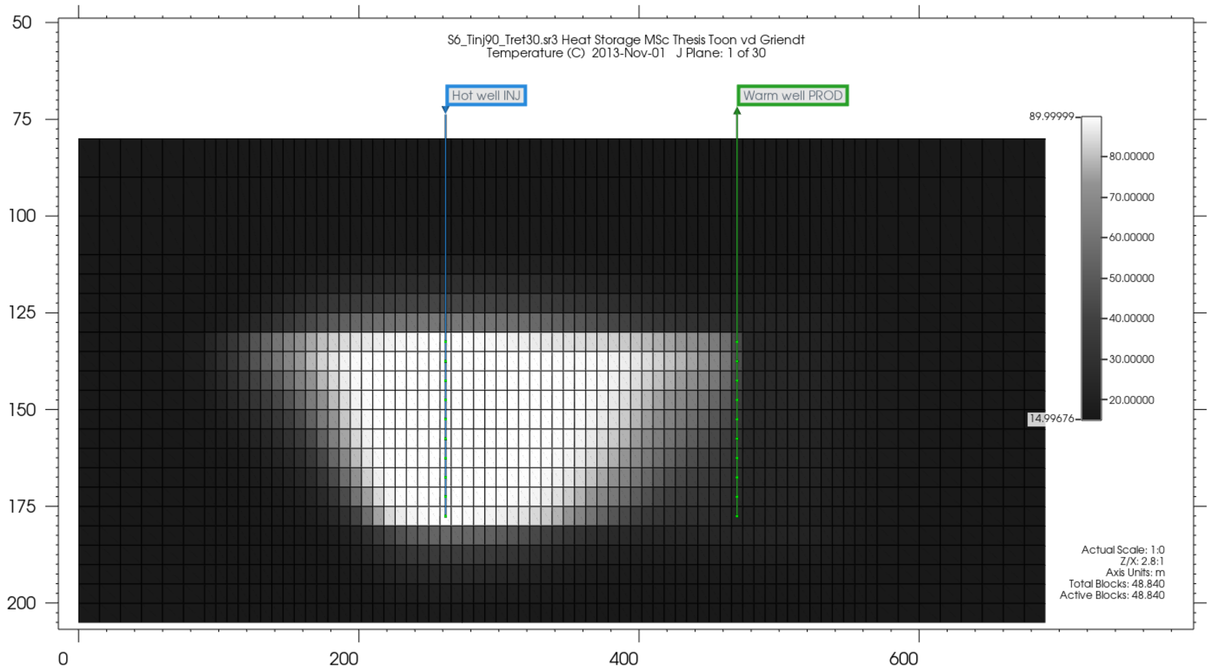

Figure 15: Vertical cross-section of the temperature profile after 3.5 cycles for scenario 6; larger temperature difference between the wells

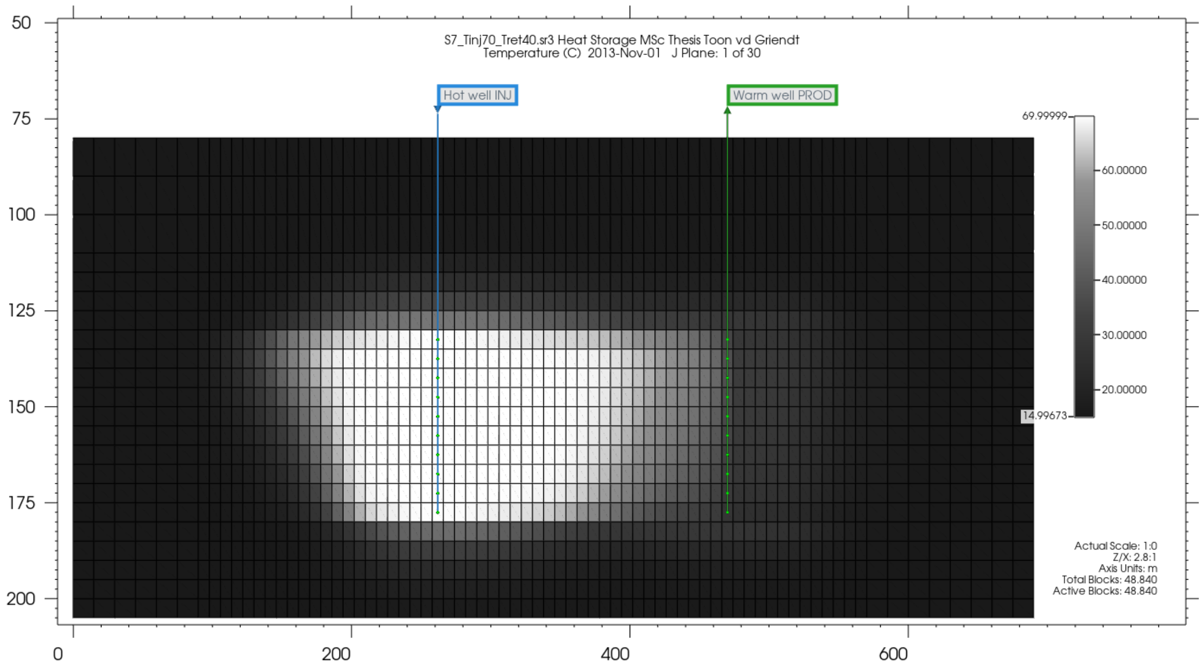

Figure 16: Vertical cross-section of the temperature profile after 3.5 cycles for scenario 7; lower temperatures in the wells

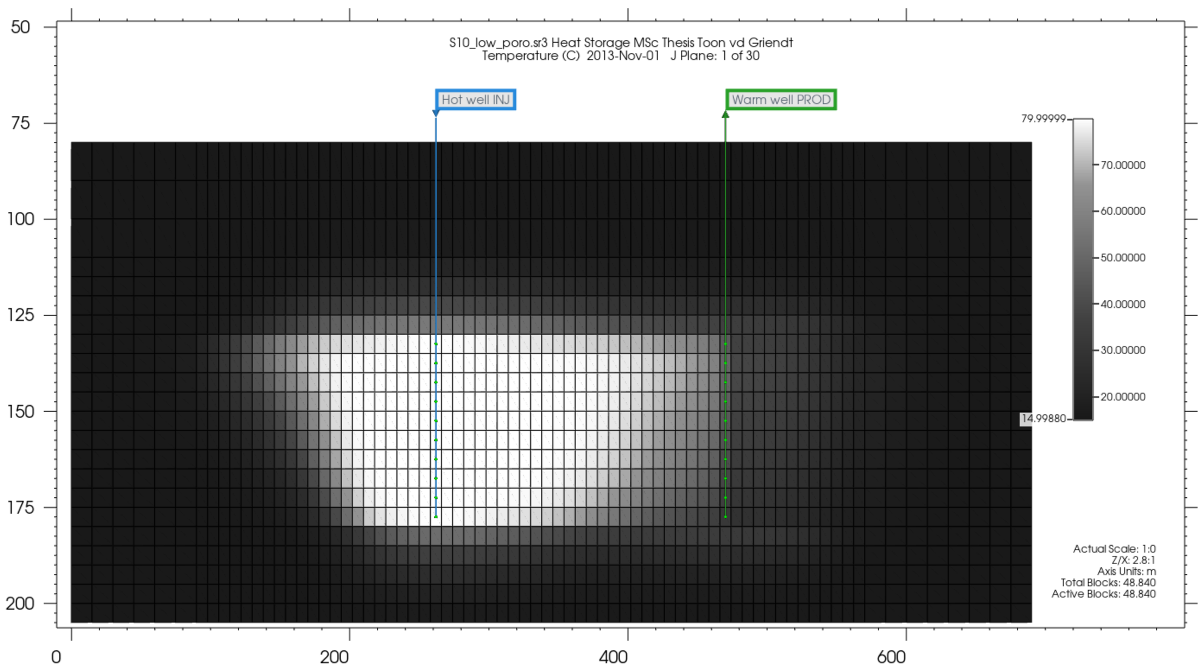

Figure 17: Vertical cross-section of the temperature profile after 3.5 cycles for scenario 10; lower porosity

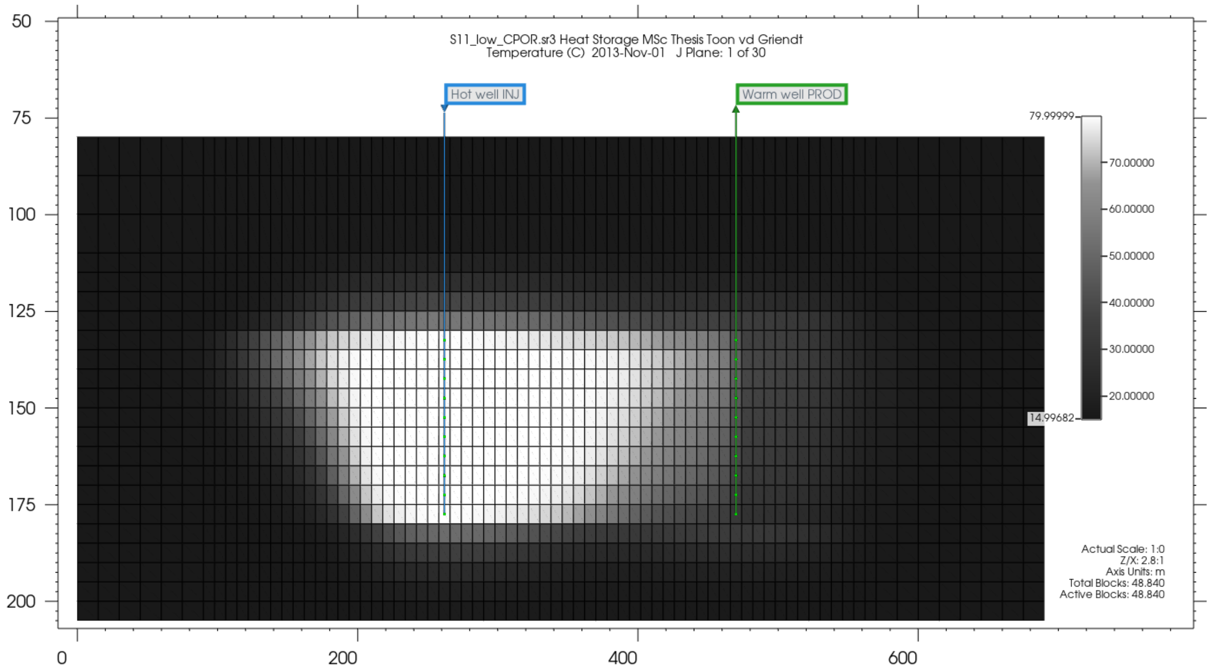

Figure 18: Vertical cross-section of the temperature profile after 3.5 cycles for scenario 11; higher rock compressibility

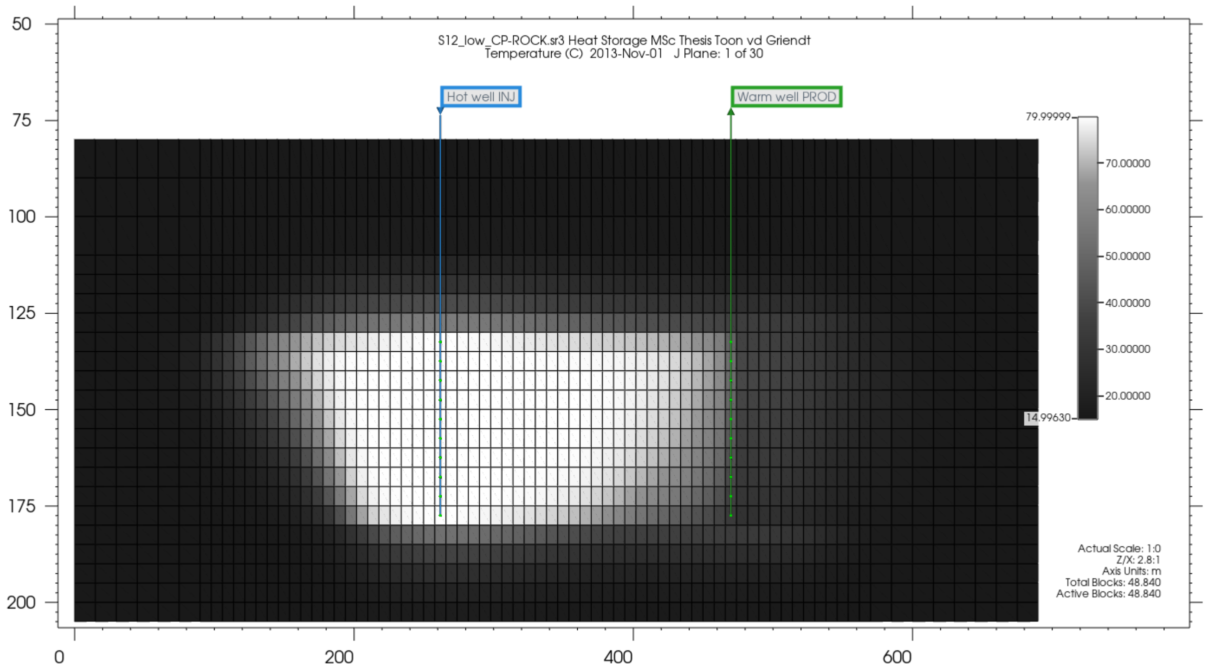

Figure 19: Vertical cross-section of the temperature profile after 3.5 cycles for scenario 12; lower rock specific heat

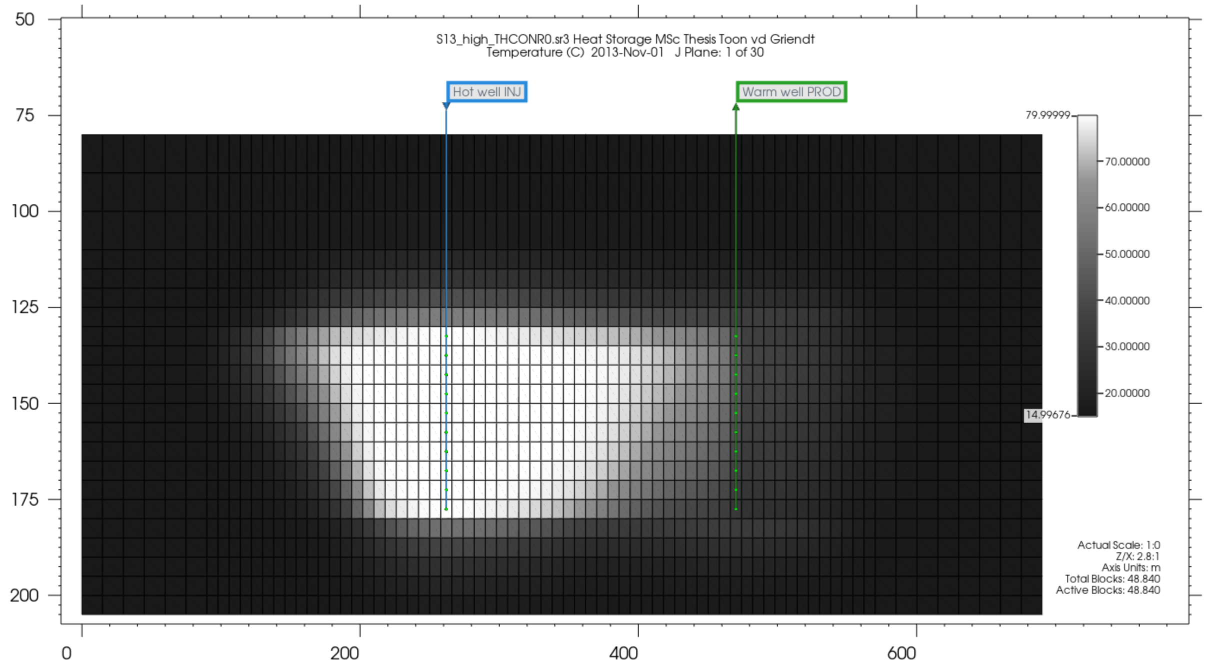

Figure 20: Vertical cross-section of the temperature profile after 3.5 cycles for scenario 13; higher rock thermal conductivity

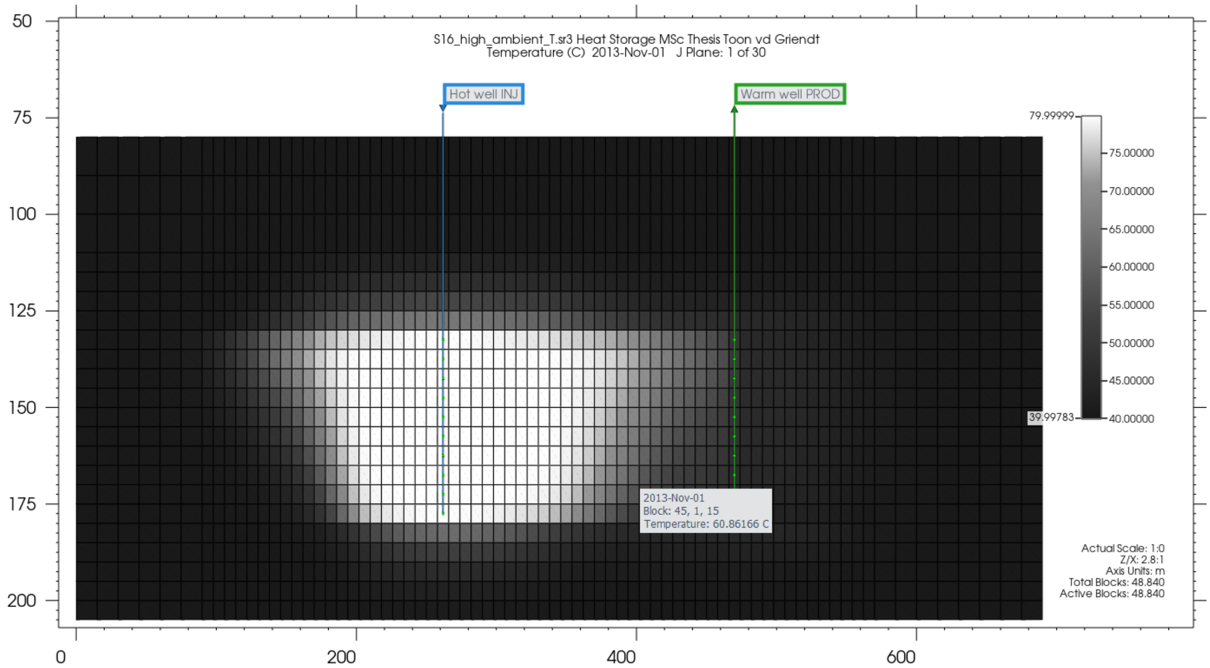

Figure 21: Vertical cross-section of the temperature profile after 3.5 cycles for scenario 16; higher ambient temperature

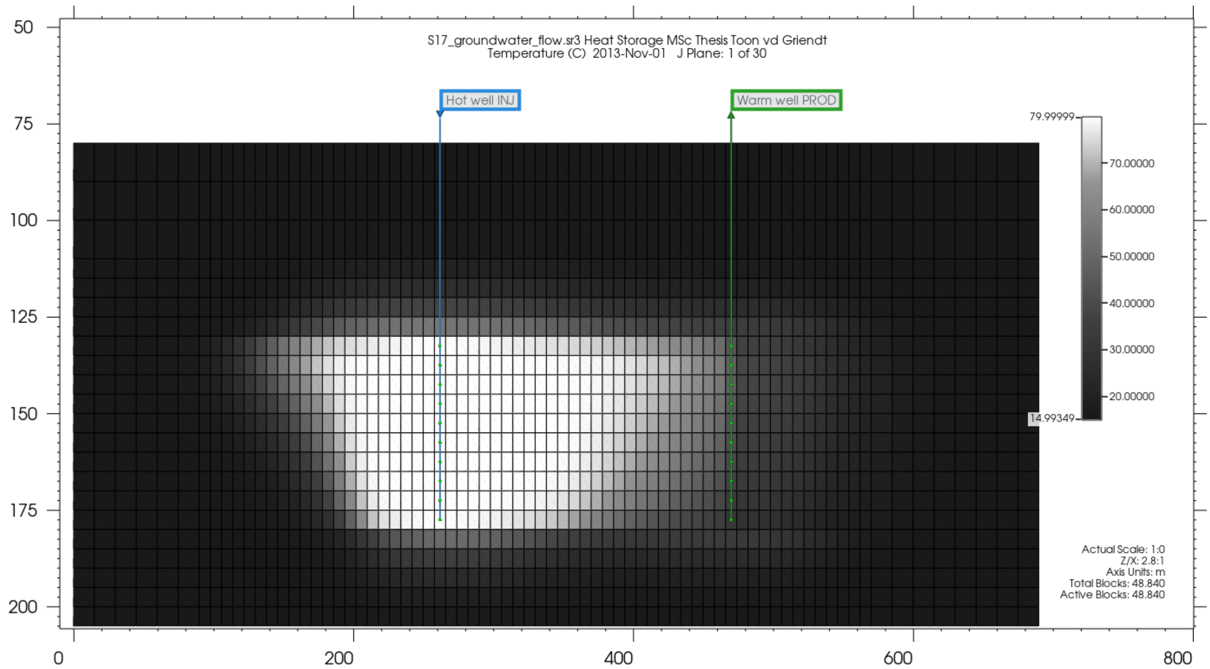

Figure 22: Vertical cross-section of the temperature profile after 3.5 cycles for scenario 17; groundwater flow

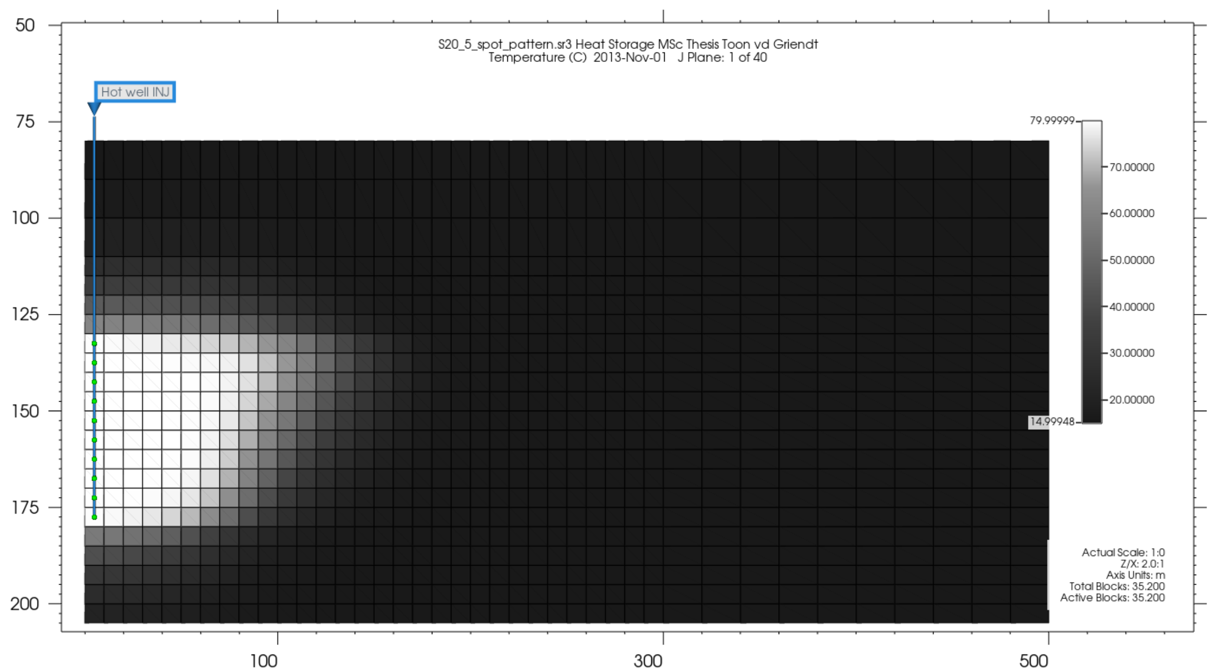

Figure 23: Vertical cross-section of the temperature profile after 3.5 cycles for scenario 20; 5-spot pattern geometry

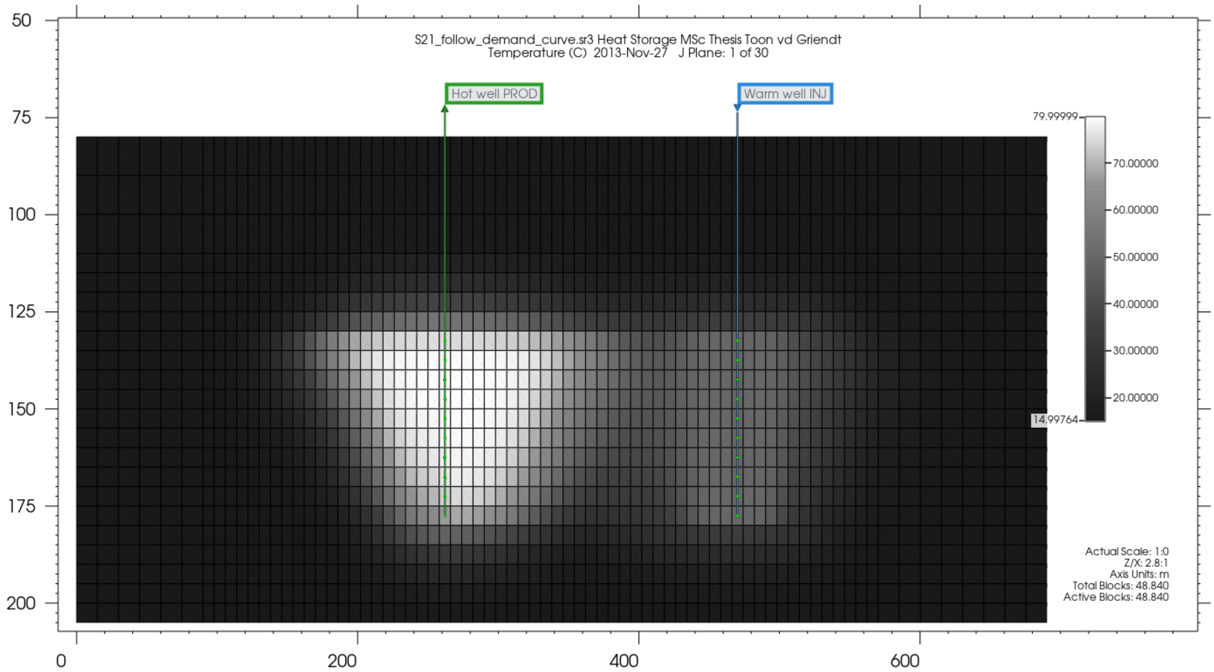

Figure 24: Vertical cross-section of the temperature profile after 3.5 cycles for scenario 21; injection and production profiles following the demand curve

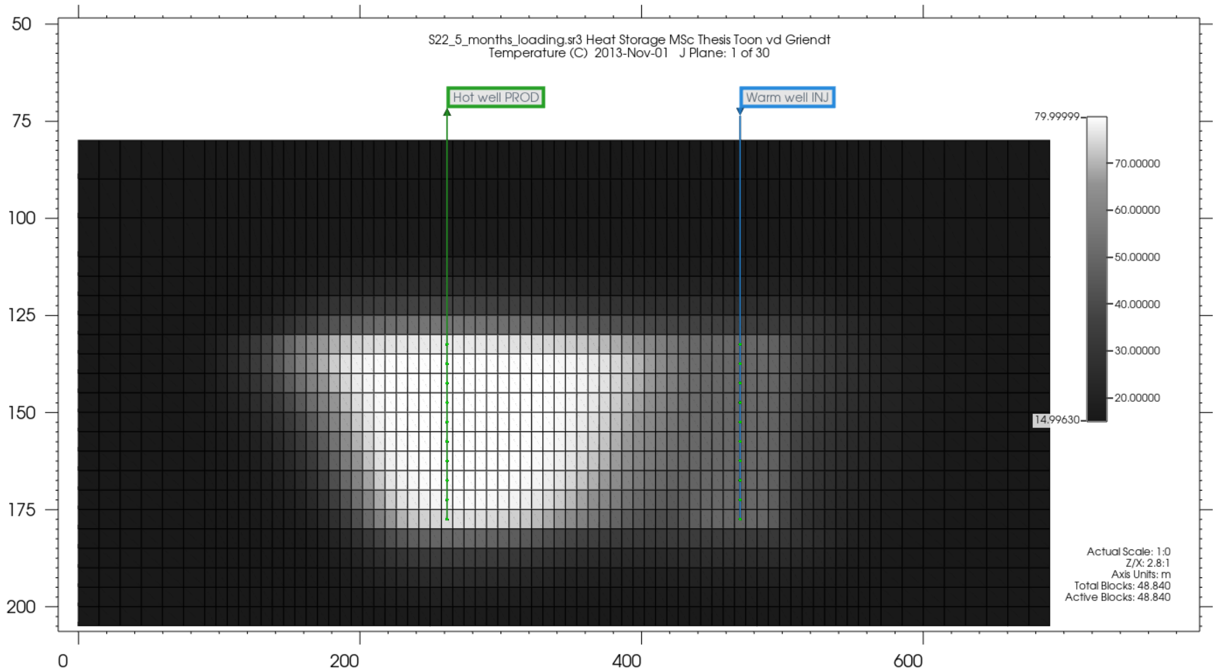

Figure 25: Vertical cross-section of the temperature profile after 3.5 cycles for scenario 22; loading in 5 months and produce during 7 months